Breaking Waves on the Ocean Surface

Michael S. Schwendeman

A dissertation
submitted in partial fulfillment of the
requirements for the degree of

Doctor of Philosophy

University of Washington

2016

Reading Committee:

James M. Thomson, Chair

Alexander R. Horner-Devine

Johannes R. Gemmrich

Program Authorized to Offer Degree:
Civil and Environmental Engineering

University of Washington

Abstract

Breaking Waves on the Ocean Surface

Michael S. Schwendeman

Chair of the Supervisory Committee:
Associate Professor James M. Thomson
Civil and Environmental Engineering

In the open ocean, breaking waves are a critical mechanism for the transfer of energy, momentum, and mass between the atmosphere and the ocean. Despite much study, fundamental questions about wave breaking, such as what determines whether a wave will break, remain unresolved. Measurements of oceanic breakers, or "whitecaps," are often used to validate the hypotheses derived in simplified theoretical, numerical, or experimental studies. Real-world measurements are also used to improve the parameterizations of wave-breaking in large global models, such as those forecasting climate change. Here, measurements of whitecaps are presented using ship-based cameras, from two experiments in the North Pacific Ocean.

First, a method for georectifying the camera imagery is described using the distant horizon, without additional instrumentation. Over the course of the experiment, this algorithm correctly identifies the horizon in 92% of images in which it is visible. In such cases, the calculation of camera pitch and roll is accurate to within 1°. The main sources of error in the final georectification are from mislabeled horizons due to clouds, rain, or poor lighting, and from vertical "heave" motions of the camera, which cannot be calculated with the horizon method. This method is used for correcting the imagery from the first experiment, and synchronizing the imagery from the second experiment to an onboard inertial motion package.

Next, measurements of the whitecap coverage, W, are shown from both experiments.

Although W is often used in models to represent whitecapping, large uncertainty remains in the existing parameterizations. The data show good agreement with recent measurements using the wind speed, U_{10}. Although wave steepness and dissipation are hypothesized to be more robust predictors of W, this is shown to not always be the case. Wave steepness shows comparable success to the wind parameterizations only when using a mean-square slope variable calculated over the equilibrium range waves and normalizing by the wave directional spread. Meanwhile, correlation of W with turbulent dissipation measurements is significantly worse, which may be due to uncertainty in the measurements or bias related to micro-breaking waves.

Finally, phase-resolved, three-dimensional, measurements of the whitecaps were made from a new ship-based stereo video system. Comparison with concurrent buoy measurements indicate that the stereo data accurately reproduces the wave statistics, including the frequency spectra. The whitecaps are characterized by transient and spatially localized regions of extreme surface gradients, rather than large crest-to-trough steepnesses. It was found that whitecaps were around 10 times more likely to have extreme slopes, and 50% of the observed extreme surface slopes were in the vicinity of the breaking waves. The maximum whitecap slopes show good agreement with the Stokes 120° limiting crest geometry, and the whitecap crest loses much of its maximum steepness shortly after the onset of breaking. The whitecap phase speeds are consistently less than the linear or weakly nonlinear predicted phase speed, which indicate the effect of narrow-band wave groups, despite the broad-band wave spectra.

TABLE OF CONTENTS

LIST OF FIGURES

LIST OF TABLES

ACKNOWLEDGMENTS

First and foremost, I need to thank Jim Thomson — "El Jefe" to use his self-given nickname from our first cruise together. It was complete luck that I got to work with Jim, but it's hard to imagine having made it this far with anyone else. This document is a testament to his guidance and support. He is the embodiment of the phrase "lead by example," and his is an example I have been glad to follow for the past five years.

My committee, Alex Horner-Devine, Johannes Gemmrich, and Randy LeVeque, are all leaders in their respective fields, all incredibly busy, and have all been fantastically generous in giving me their time. I am lucky to have had their support throughout this process. A special thanks goes to Alex, the consummate committee member, for also serving on my Masters and qualifying committees. Alex was also instrumental in recruiting me to UW, and for that I cannot thank him enough.

Next, I am indebted to Alex de Klerk and Joe Talbert. Without their hard work and technical expertise, there would be nothing here for me to write about. I had the pleasure of spending six weeks at sea with these two, from which I have nothing but good memories.

A big shoutout to the EFM group, with whom I've spent countless Thursday lunches. The group has grown tremendously in my time here, and it has been amazing to be a part of it. In particular, thanks to Roxanne Carini, who has been my friend and officemate since 2011, when we showed up at UW on the same exact day. Thanks to Seth Zippel for sharing numerous conference hotel rooms (and the occasional bed). The rest of my officemates at Ben Hall 211, past and present, have all been fantastic: J. Paul Rinehimer, Chris Bassett, Maricarmen Guerra Paris, and Maddie Smith.

I am grateful for Peter Diamessis at Cornell University, who took me on as an undergrad-

uate researcher, before I knew anything, and taught me as much as he could about numerical models and internal waves. Without his advice, I certainly would not have ended up at UW, and may not have gone to graduate school at all.

For funding my work at UW, I would like to thank the National Science Foundation, the Seattle ARCS Foundation, and the Gibbs family. The UNOLS organization provided the ships for our experiments, and the captains and crews of the R/V *New Horizon* and R/V *Thomas G. Thompson* were instrumental in making these experiments a success. Also thanks to Stephanie Downey, Mike Ohmart, Adam Brown, and Jarett Goldsmith for their help during these cruises.

The foundations of this research were laid by dozens of exemplary scientists, such as Owen Phillips, James Duncan, Mike Banner, Ken Melville, Edward Monahan, and Bill Plant, some of whom I've been lucky enough to meet along the way. On the subject of amazing scientists, thanks to Johannes Gemmrich, Adrian Callaghan, Peter Sutherland, and many others, for helpful advice and suggestions.

Outside of science, I am grateful for the support I've received from my friends in Seattle. In particular, my cousins Marta, Cailen, Pam, and Shams, went above and beyond the call of duty in making me feel welcome in a totally new corner of the country.

I cannot thank my family enough for their love and support for 27 years. Whatever I have accomplished, my parents, my brother, and my grandparents deserve most of the credit. I love you all very much.

Finally, my fiancée Anna. I have relied on her strength so many times over the years, and she has always been there to listen when I've needed to vent. I am so proud of what we have done together. And I promise when this is over I will go outside.

DEDICATION

To my parents, for everything.

Chapter 1
INTRODUCTION

1.1 Motivation

Surface waves are a familiar sight to anyone who has spent time on or near the ocean. Driven by the wind, these waves propagate along the air-water interface under the restoring force of gravity. The physics governing these waves are largely understood when the waves are small. As the waves grow, however, many will become unstable and break, at which point a new set of dynamics is needed. The mechanics of wave-breaking are still not well understood, particularly for the waves that break in the open ocean away from the coast.

"Whitecaps," as these deep water breaking waves are often called, play a critical role in many of the large-scale interactions between the atmosphere and the ocean (Melville, 1996). The transfer of energy, momentum, heat, and mass between the ocean and atmosphere is strongly dependent on the whitecaps, making breaking waves a critical component of the global climate system (Cavaleri et al., 2012). Whitecaps also dissipate surface wave energy, in the form of turbulence and bubble production. In deep water, wave-breaking is the primary mechanism for wave dissipation, therefore, understanding the energetics of the whitecaps is critical for improving upon the present operational wave forecasts (Cavaleri et al., 2007).

Theoretical study of wave-breaking is difficult, as the flow becomes turbulent, highly nonlinear, and two-phase. Instead, the understanding of breaking has progressed though a combination of three methodologies: numerical simulations, laboratory experiments, and — the focus of this thesis — field measurements. Measurements in the field are often necessary to test the theories developed in laboratory experiments, or to verify results or inputs for numerical models (Perlin et al., 2013). For example, implementation of whitecaps in current

climate models uses an empirical relation based on a simple theory with constants found from field observations (see de Leeuw et al., 2011).

The field data used here were taken during two research cruises in the North Pacific Ocean, in October 2012 and January 2015. In both cases, the primary goal of the cruise was to reach Station Papa, located at 50° N, 145° W, to replace a moored long-term wave measurement buoy. However, additional time was scheduled to make measurements of the waves from the ship and from short-term drifting buoy deployments.

This thesis is primarily related to measurements of whitecaps from ship-based cameras. Visible imagery is a powerful tool for quantifying whitecapping, but it can be difficult to automate the analysis and interpret the imagery. Two metrics have been commonly used in measuring whitecaps from cameras: the fractional whitecap coverage, W, and the normalized distribution of whitecap crest length by speed, $\Lambda(c)$. In addition, recent work has shown that accurate measurements of the surface waves can be made by stereo processing of images from two or more cameras (e.g. Gallego et al., 2011; de Vries et al., 2011; Benetazzo et al., 2012, and others). Here, a stereo video system is used to study the geometry of the whitecaps at breaking onset. As stereo video becomes more widely used and accepted, it is likely to yield important insights into the fundamental questions of breaking waves.

1.2 Ocean Waves Basics

1.2.1 Linear Wave Theory

With just a few assumptions, it is possible to solve for the equations of motion of surface waves. The result is called "linear wave theory," or sometimes "Airy wave theory." The derivation starts by assuming inviscid, incompressible, and irrotational fluid motion, which considerably simplifies the mass and momentum conservation equations. These are generally good assumptions that are extended even to the non-linear theories described later. A troublesome problem remains in the boundary conditions, which are to be applied at the sea surface, at an unknown height. Assuming wave heights that are small relative to their

wavelength, the boundary conditions may be applied at the mean water line, $z = 0$. This "linearizes" the equations, and leads to expressions for the surface position, η, water velocity, (u, v), and water pressure, p. Despite the simplifying assumptions, linear theory often provides a close approximation to the true wave motion, and reveals a number of important properties of surface waves.

One of the most important results of the linear solution is the dispersion relation, which relates a wave's frequency, f, to its wavenumber, k. f and k are the inverse of wave period, T, and wavelength, L, respectively, and are often used for mathematical convenience. In deep water the dispersion relation can be written as

$$\omega^2 = gk_{rad}, \tag{1.1}$$

where ω and k_{rad} are the radian frequency and wavelength ($\omega = 2\pi f$, $k_{rad} = 2\pi k$). The wave phase velocity, c_p, is the speed at which wave crests (and troughs) move, and is given by

$$c_p = \omega/k_{rad} = \sqrt{g/k_{rad}} = \sqrt{gL/(2\pi)}. \tag{1.2}$$

The group velocity, c_g, is the propagation speed of wave groups, which relates to the flux of wave energy. For linear waves, c_g can be calculated as

$$c_g = \frac{\partial \omega}{\partial k_{rad}} = \frac{1}{2}\sqrt{\frac{g}{k_{rad}}} = c_p/2. \tag{1.3}$$

The dispersion relation reveals that longer waves propagate faster, in both phase and group velocity, which causes waves of different length to "disperse." Moreover, the wave phase moves at twice the speed of the wave groups, which results in important group dynamics. In intermediate and shallow water, the above equations also depend on the water depth, d.

1.2.2 The Wave Spectrum

In nature, waves are rarely observed propagating at a single frequency in a single direction (these would be called "monochromatic" and "unidirectional" waves). However, Fourier theory states that any stationary signal can be decomposed into a summation of sinusoids.

Thus, even the most complicated "wavefield," can be represented as a combination of waves of different frequencies, each of which approximately follows the linear theory. This representation is called a wave spectrum, and gives the contribution of energy (which is proportional to squared wave height) at every wave frequency. In practice, the spectrum must be averaged over sufficient time and/or space in order to achieve a statistically robust distribution of energy. In doing so, the phase of the sinusoids is lost and the result is a "phase-averaged" representation of the wavefield. However, the spectral approach is appealing because the results of linear theory (dispersion, etc) can be applied at each frequency. Thus, the phase-averaged spectrum also forms the basis for most wave forecast models.

The sea surface, $\eta(x, y, t)$, is a function of two spatial dimensions (x and y) and time (t). Thus, the full wave spectrum, $\chi(k_x, k_y, t)$, is also a three-dimensional function, of two wavenumbers (k_x and k_y) and frequency (f). As it is difficult to measure the full three-dimensional sea surface, the full spectrum is rarely calculated. Instead, projections of the full spectrum are often shown, such as the frequency spectrum, $S(f)$, or frequency-directional spectrum, $S(f, \theta)$. Even this latter quantity is usually an approximation of the true directional spectrum, as reconstructed from low order directional "moments" using maximum likelihood or maximum entropy.

In any of its forms, the spectrum is normalized such that the area under the curve is the total variance of the surface, σ^2. It is often useful to represent the spectrum in terms of scalar "bulk parameters." For example, a commonly calculated parameter is the significant wave height,

$$H_s = 4\sigma, \tag{1.4}$$

which is used as a characteristic wave height in describing the wave conditions. The characteristic wave frequency, wavenumber, or wave direction are often given by the values at the spectral peak. Alternatively, energy-weighted mean values are often found from the spectrum. For example, mean frequency may be defined as

$$f_m = \frac{\int f S(f) df}{\int S(f) df}. \tag{1.5}$$

1.2.3 Wave Nonlinearity

The derivation of linear wave theory depends on assuming waves of small amplitude relative to their wavelength. The ratio of wave height or amplitude to wavelength is called the steepness. As the steepness gets large, deviations from linear theory become more noticeable. In deep water, perturbation theory may be used to account for nonlinearity. Perturbation theory works by assuming power series solutions for the variables η, u, v, ω, etc., where higher order terms are polynomials in steepness. As more terms are retained in the perturbation solution, the solution approaches the true nonlinear solution.

Although linear wave theory is useful in many circumstances, it does not account for a number of important properties of nonlinear waves. One example is Stokes drift, which is a net mass transport in the direction of wave motion. In linear theory, water parcels move in closed orbits, with no net translation. Similarly, the shape of nonlinear waves is not symmetric like the sinusoids of linear theory. Instead, nonlinear waves have more peaked crests and flat troughs.

Two nonlinear effects are most relevant to this thesis. First is the Benjamin-Feir instability, sometimes called modulational instability, which prevents waves from propagating as unimodal wave trains. The modulational instability causes such waves to break up into modulating wave groups, and leads to a steepening of the waves at the center of the group. It has been suggested as one physical mechanism for the wave steepening that often precedes wave breaking.

Second, it can be shown that nonlinear waves have a maximum attainable steepness, which is often called the Stokes limit. The limiting wave has a steepness of $H/L \approx 1/7$, and its crest forms a corner of angle 120°. For this solution, the peak of the crest is a singularity where the surface water velocity exactly equals the phase speed. As discussed below, it has often been suggested that waves break when they reach the Stokes limit.

Finally, some nonlinear effects are more subtle, such as the so-called "wave-wave" interactions, in which combinations of waves of different frequencies resonate and exchange energy.

In deep water, the dominant wave-wave interaction occurs between two pairs of wave frequencies, or quadruplets, the effect of which is to transfer energy out of certain frequencies and into others. This is a rather "weak" nonlinearity in that the effects are only felt over relatively large distances and times. Still, it is one of the dominant processes governing the evolution of the wave spectrum in the open ocean, as described below.

1.2.4 The Radiative Transfer Equation

The radiative transfer equation describes the change in a wavefield in time and space. For example, if one were to drop a stone in a quiet lake, the radiative transfer equation would determine the outward radiation of the wave energy. The equation takes the form of a conservation equation, where the quantity conserved is the "wave action," n, which is the wave energy divided by wave frequency. Without outside forcing, the only evolution in the wavefield is from dispersion and directional spreading of the energy. In this case, the radiative transfer equation can be written as

$$\frac{\partial n}{\partial t} + \overrightarrow{c_g} \cdot \nabla n = 0. \tag{1.6}$$

In the open ocean, three main forces alter the wave action balance. These are incorporated into the radiative transfer equation as "sources" and "sinks" of wave action or energy. The first is the wind, which pumps energy into the waves. The second is wave-breaking, which dissipates wave energy, primarily in the form of turbulence in the upper ocean. Finally, is the nonlinear wave-wave interactions mentioned in the previous section. These do not change the overall energy in the waves, but rather transfer energy between waves of different frequencies. The nonlinear interactions are responsible for most wave spectra having a somewhat common shape, especially at high frequencies.

The final radiative transfer equation is given as

$$\frac{\partial n}{\partial t} + \overrightarrow{c_g} \cdot \nabla n = S_{in} + S_{ds} + S_{nl}, \tag{1.7}$$

where the terms S_{in}, S_{ds}, and S_{nl} represent the wind input, wave-breaking dissipation, and

nonlinear interactions, respectively. By modeling these source terms, the change in the wave-field can be predicted. The radiative transfer equation is at the heart of the so-called "third generation" global wave forecast models, such as WAM, WAVEWATCH III and SWAN.

1.3 Review of Wave Breaking

1.3.1 Breaking Onset

When a wave breaks, the result is a turbulent, two-phase flow that cannot be described analytically with either the linear or weakly nonlinear theories mentioned above. The complexity of the wave-breaking problem has hampered progress on even the most fundamental questions. For example, it is still not clear exactly what causes a wave to break.

Scientists have long sought a universal criteria for determining the onset of breaking. The Stokes limit gives an upper bound on the wave steepness ($H/L \approx 1/7$), thus, it has often been suggested that waves must achieve this steepness before breaking. Unfortunately, the Stokes limit does not appear to provide a robust, universal criteria for breaking. This can be seen in several studies showing waves breaking well below the Stokes limit (for example Holthuijsen and Herbers, 1986; Rapp and Melville, 1990; Banner and Pierson, 2007; Drazen et al., 2008; Tian et al., 2010). Conversely, other studies (for example Babanin et al., 2007, 2010) have shown experimental and numerical evidence of waves approaching the limiting steepness just prior to breaking. At the very least, it does seem that waves at the Stokes limit will break, although three-dimensional affects may alter the limiting value slightly (the Stokes limit being derived for two-dimensional waves only).

The Stokes limit is related to another suggested criteria, which states that waves break when the horizontal water velocity at the crest exceeds the phase speed of the wave. This makes physical sense, especially when picturing a large plunging breaker. However, validation of this kinematic criteria has also been ambiguous. In particular, Stansell and MacFarlane (2002) measured both the water velocity U and phase speed c_p of breakers in a laboratory tank, and found that for any of several definitions of c_p, the kinematic criteria did not hold

up (i.e. $U < c$ at breaking).

Both the steepness and kinematic limits may therefore provide only a sufficient, but not necessary, condition for breaking. The work of Banner and Tian (1998), Song and Banner (2002), and Banner and Pierson (2007) advocate for a different type of breaking criteria, which has been called a "dynamic criteria." These papers suggest that breaking occurs when the rate of growth of wave energy (potential plus kinetic) exceeds a universal threshold. This criteria works particularly well for the case of modulating wave groups. In this scenario, the Benjamin-Feir instability causes wave energy to slowly converge towards the center of the group, leading the center wave to either break and quickly dissipate energy, or to not break and repeat the modulational cycle, which is called "recurrence." Song and Banner (2002) show that the dynamic criteria is capable of distinguishing between initially very similar breaking and recurrence cases.

A number of factors make the evaluation of these breaking criteria difficult, especially outside of a controlled laboratory environment. For one thing, it is difficult to measure both the surface configuration (for steepness or potential energy) and the water velocity (for orbital velocity and kinetic energy) leading up to and during breaking. Application of the dynamic breaking criteria is particularly challenging (Perlin et al., 2013). Moreover, it becomes difficult to even define quantities like wave steepness, phase speed, and energy growth in a spectral wave environment. For example, Chalikov and Babanin (2012) evaluated each of these criteria in numerical simulations of spectral waves, and were unable to find any universal criteria among them.

1.3.2 Whitecap Coverage, W

A related question to predicting the breaking onset of an individual wave is determining how many waves will break within a given wavefield. This can be expressed as a breaking frequency, breaking probability, or, most commonly, whitecap coverage. The whitecap coverage, W, is the average fraction of sea surface covered by whitecaps. W is frequently used in parameterizations of gas transfer (Woolf, 2005) and sea spray aerosol production

flux (de Leeuw et al., 2011). W has been frequently found to scale with the wind speed, usually defined as the 10-meter wind speed, U_{10}. The most widely used relation comes from Monahan and O'Muircheartaigh (1980), who fit to the available data a power law of the form

$$W = 3.84 \times 10^{-6} U_{10}^{3.41}, \tag{1.8}$$

where U_{10} is in m/s, and W is the fractional coverage. More recent measurements of W include Stramska and Petelski (2003), Sugihara et al. (2007), and Callaghan et al. (2008a).

Although fits of W to U_{10} are common, the wind does not directly cause waves to break (Babanin, 2011). Instead, the onset of breaking is more directly related to wave variables, such as increased wave steepness. Banner et al. (2000) and Banner et al. (2002) show that as the average wave steepness increases, so does the probability of whitecapping. Therefore, average steepness parameters have recently been suggested in place of wind variables in parameterizations of W. In fetch-limited waves, Kleiss and Melville (2010) show good agreement between W and the mean steepness, although the fit to wind speed is still slightly better. Alternatively, Goddijn-Murphy et al. (2011) and Salisbury et al. (2013) have suggested using wave steepness as a secondary variable to correct for in shortcomings in the wind speed parameterizations.

Others have suggested that W may be related to the energy dissipation from wave-breaking, S_{ds}. The first to propose this idea was Cardone (1970), after noting that fits to wind speed suffered from uncertainties related to the atmospheric stability. However, large uncertainties in the value of S_{ds} make the development and application of such relations challenging. Kraan et al. (1996) derived a theoretical prediction for W based on the WAM dissipation source function and a JONSWAP spectrum, which showed reasonable agreement with their measured whitecap coverage. Hanson and Phillips (1999) used estimates of dissipation from the Phillips (1985) equilibrium range theory, and showed improved correlation over U_{10} fits. Most recently, Hwang and Sletten (2008) derived a dissipation parameterization based on a total equilibrium with wind energy input.

One of the ambiguities of calculating W (and other measurements based on the presence

of visible foam) is in the distinction between foam from actively breaking waves and old, residual foam from previous breakers. It is often noted that the active whitecap coverage is dependent on the wave dynamics only, whereas the residual foam decay is also a function of the bubble and water chemistry (see Callaghan et al., 2008b). However, there is currently no automated method for differentiating between active and residual whitecap foam in visible imagery (Scanlon and Ward, 2013).

1.3.3 Wave Breaking Dissipation

Of the radiative transfer equation source terms, it is generally agreed that the breaking dissipation term is the least well-constrained (Babanin, 2011). One challenge is that breaking does not fit well within the spectral framework. Wave breaking is a strongly nonlinear process that is localized in space and time, whereas the spectrum is an average quantity that evolves on long spatial and temporal scales. The implementation of breaking dissipation in current models is often based on Hasselmann (1974), in which a random distribution of whitecaps does negative work by exerting downward pressure on the front face of the waves. Historically, improvements to this model were often made based on empirical comparisons with observations, rather than improved physical understanding (i.e. using S_{ds} as a "tuning knob," see Cavaleri et al., 2007). Only recently have effects such as the dissipation of swell waves by the wind and the threshold behavior of wave-breaking been implemented in the spectral models (see Ardhuin et al., 2010).

Further progress has been made primarily through laboratory experiments. The experiments of Duncan (1981) were particularly important, as they describe a physical scaling to relate the speed of a breaking wave to its rate of energy dissipation. This was done by towing a hydrofoil through a long channel at a constant speed and depth, setting up a steady breaking wave in the wake. Duncan determined that the rate of energy loss scaled as

$$\epsilon_l \propto \frac{\rho_w c^5}{g} \tag{1.9}$$

where ϵ_l is the energy dissipation per crest length, ρ_w is the water density, g is gravitational

acceleration, and c is the speed of the hydrofoil and breaker.

Other experiments have since been performed using more realistic breakers. The study of Rapp and Melville (1990) pioneered the use of "dispersive focusing" to induce breaking at a chosen distance along a wave tank. Subsequent experiments, such as Lamarre and Melville (1991) and Melville (1994), showed a dependence on wave steepness in the resulting dissipation. Drazen et al. (2008) incorporated this steepness dependence into Equation 1.9, resulting in the scaling,

$$\epsilon_l \propto \frac{\rho_w c^5 (hk)^{5/2}}{g}. \tag{1.10}$$

Meanwhile, Banner and Pierson (2007) proposed that the breaking strength is better parameterized using the rate of wave energy convergence, rather than wave steepness.

Most of the energy lost during breaking goes into the production of turbulence, which is itself primarily dissipated in the upper layer of the ocean. This is observable in measurements of the vertical profile of the turbulent dissipation rate. In the near-surface region, the dissipation is significantly larger than predicted by the "law of the wall" for turbulence over a flat boundary (see Agrawal et al., 1992; Terray et al., 1996; Gemmrich and Farmer, 2004; Gemmrich, 2010). There remains some question as to the exact structure of the energy fluxes and turbulent dissipation profiles, but Thomson et al. (2016) showed that there is generally good agreement between total near-surface turbulent dissipation and wave-breaking dissipation. That study used measurements from drifting SWIFT buoys (Surface Wave Instrument Float with Tracking), which measure turbulent dissipation profiles in the wave reference frame, as first described in Thomson (2012). The same SWIFT buoys are used throughout this thesis as well.

1.3.4 Phillips' Equilibrium Hypothesis and $\Lambda(c)$

Under many conditions, it has been observed that the wave-breaking dissipation is approximately equal to the wind input (see, for example, Hwang and Sletten, 2008; Thomson et al., 2013). In other words, the wind and the whitecaps are in near equilibrium. This is re-

lated to the study of Phillips (1985), which hypothesized that for waves shorter than the peak wavelength, an equilibrium range exists such that wind input, nonlinear transfers, and dissipation are all of the same order and approximately in balance. This allowed Phillips (1985) to derive an expression for the spectral form of the dissipation function within the equilibrium range,

$$\epsilon(c) = 4\gamma\beta^3 I(3p)\rho_w u_*^3 c^{-1} \tag{1.11}$$

where

$$I(3p) = \int_{-\pi/2}^{\pi/2} (\cos\theta)^{3p} d\theta \tag{1.12}$$

is a directional weight function, γ, β, and p are constants, and u_* is the wind friction velocity.

Furthermore, Phillips (1985) realized the utility of the Duncan (1981) dissipation scaling, as a way to determine the spectral dissipation from observations of the whitecap speeds, and perhaps validate Equation 1.11. Thus, Phillips (1985) introduced a distribution function for breaking, $\Lambda(c)$, which was defined as the distribution of breaking crest lengths per area as a function of speed, c. Using this definition, along with Equation 1.9, Phillips (1985) proposed a relation for the spectral breaking-induced dissipation, namely,

$$S_{ds}(c) = \frac{b\rho_w}{g} c^5 \Lambda(c) \tag{1.13}$$

where b is a "breaking strength" scaling factor, and c is the phase speed (which was assumed to equal the breaker speed).

Phillips et al. (2001) made the first measurements of $\Lambda(c)$ in the field, using marine radar. Numerous studies since then (Melville and Matusov, 2002; Gemmrich et al., 2008; Thomson et al., 2009; Kleiss and Melville, 2010, and others) have measured $\Lambda(c)$ using digital video cameras. There has been overall agreement in the shape of $\Lambda(c)$, which generally peaks at roughly one-half of the spectral peak phase speed. However, there has been no consensus on the value of b, indicating that it is likely not a constant. Romero et al. (2012) was the first to incorporate the steepness correction of Drazen et al. (2008) into b. Specifically, they used

the spectral saturation, defined as

$$\sigma = \frac{(2\pi)^4 f^5 E(f)}{2g^2} \tag{1.14}$$

as a proxy for the spectral steepness. The saturation was used as it closely relates to the wave mean square slope (see Banner et al., 2002).

A potential issue in the above studies is "microbreaking," a phenomenon first described in Banner and Phillips (1974). Microbreakers are breaking waves which occur at small scales and do not entrain air, therefore they do not form whitecaps. Thus, microbreaking is missed by measurements that rely on visible foam, such as from standard digital cameras. Jessup and Phadnis (2005) showed that infrared (IR) cameras could be used to measure $\Lambda(c)$ in laboratory microbreakers. Sutherland and Melville (2013) used IR cameras to measure microbreaking in the open ocean, and found that this methodology shifted the peak in $\Lambda(c)$ to much shorter wavelengths when compared with traditional video cameras.

1.4 Prior Work - Masters Thesis

The calculation of $\Lambda(c)$ played a large role in the author's Masters thesis (Schwendeman, 2012), which was later adapted to an article in the Journal of Physical Oceanography, the full citation for which is:

> Schwendeman, M., J. Thomson, and J. R. Gemmrich. Wave breaking dissipation in a young wind sea. *J. Phys. Ocean.*, 44(1):104-127, 2014. doi: 10.1175/JPO-D-12-0237.1.

During peer review, a number of important modifications were made from the original Masters thesis. Therefore, the major results and conclusions from the journal article are summarized below.

Data was taken from a field experiment in the Strait of Juan de Fuca, north of Washington's Olympic Peninsula. Over two days in February 2011, a storm produced consistently strong offshore winds, which made for an ideal study of wave-breaking dissipation. Wind

and whitecap measurements were made from the R/V *Robertson*, which was allowed to drift slowly downwind as each day progressed. The whitecaps were recorded from a digital video camera mounted at about 7 meter height, above the ship's wheelhouse. Nearby were two drifting SWIFT buoys, which measured the wave frequency spectra and turbulent dissipation profiles. An additional measure of the turbulence was made from an array of "Dopbeam" current profilers, tethered to the ship on a long cord at sufficient distance to minimize disturbance.

Figures 1.1, 1.2, and 1.3 show the resulting data products. In Figure 1.1 the frequency spectra are shown and colored by the fetch (in km) and the wind stress, u_*. The high-frequency decay is compared with f^{-4} and f^{-5} power laws, which are predicted on theoretical grounds in Phillips (1985) and Phillips (1957), respectively. Figure 1.2 plots the average dissipation profiles from the two SWIFTs, as well as the integrated dissipation rate, which is used throughout as an estimate of S_{ds}. Both are shown as a function of the offshore distance, called the "fetch." The integrated turbulent dissipation rate from the Dopbeam array is also shown. In the later analysis, a 0.5 W m^{-2} "background dissipation" is subtracted from the integrated turbulent dissipation rate.

Finally, Figure 1.3 shows the measured $\Lambda(c)$ distributions, plotted on linear and logarithmic axes, and against both dimensional and non-dimensional speed. $\Lambda(c)$ was calculated using the Fourier method of Thomson and Jessup (2009), with minor modifications. The curves are colored by the wave mean square slope (mss), calculated from the spectra as

$$\text{mss} = \int \frac{2\sigma}{f} df = \int \frac{(2\pi)^4 f^4 E(f)}{g^2} df. \tag{1.15}$$

Several of the $\Lambda(c)$ measurements at short fetches were found to be less reliable, as their breaking rates were significantly less than those estimated from cameras on the SWIFTs. Figure 1.3 also shows a c^{-6} power law decay, as predicted from the Phillips (1985) equilibrium range calculations.

The growth of the waves was compared with classical fetch "laws," as shown in Figure 1.4. These are empirical relations used to determine the wave height and frequency for

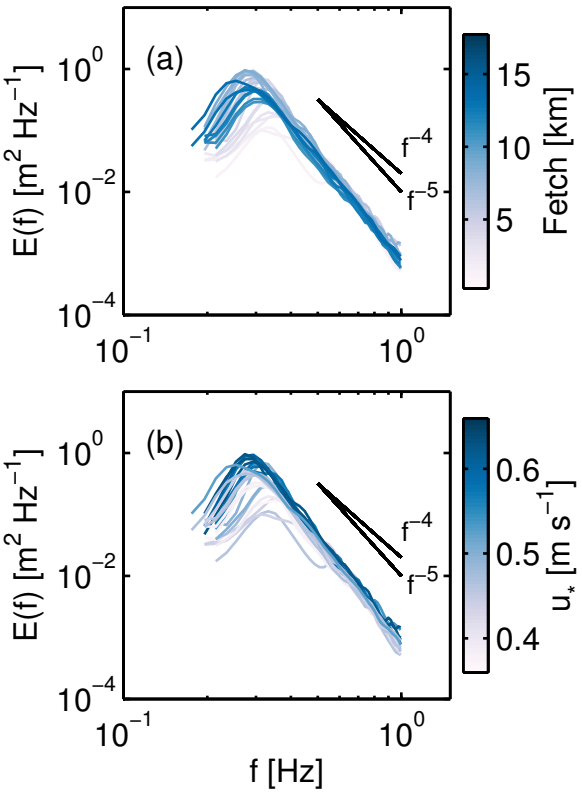

Figure 1.1: Wave frequency spectra colored by fetch (a) and u_* (b). Also shown are power laws of the form f^{-4} and f^{-5}.

fetch-limited waves, given the (assumed constant) wind speed and fetch. The exact laws used are a synthesis of several earlier studies, from Young (1999). The fetch law comparison was complicated by the fact that the wind speed was not constant as measured from the ship, especially at the shortest fetches. Thus, Figure 1.4 shows the results using three different scaling wind speeds. A daily average wind speed gave the closest agreement to the expected growth. Interestingly, offshore buoy measurements showed relatively steady winds throughout the experiment, with waves closely matching the fetch laws. This may be related to an evolution of the boundary layer with fetch, as shown by the changes in the wave mean square slope and the drag coefficient, especially at short fetches.

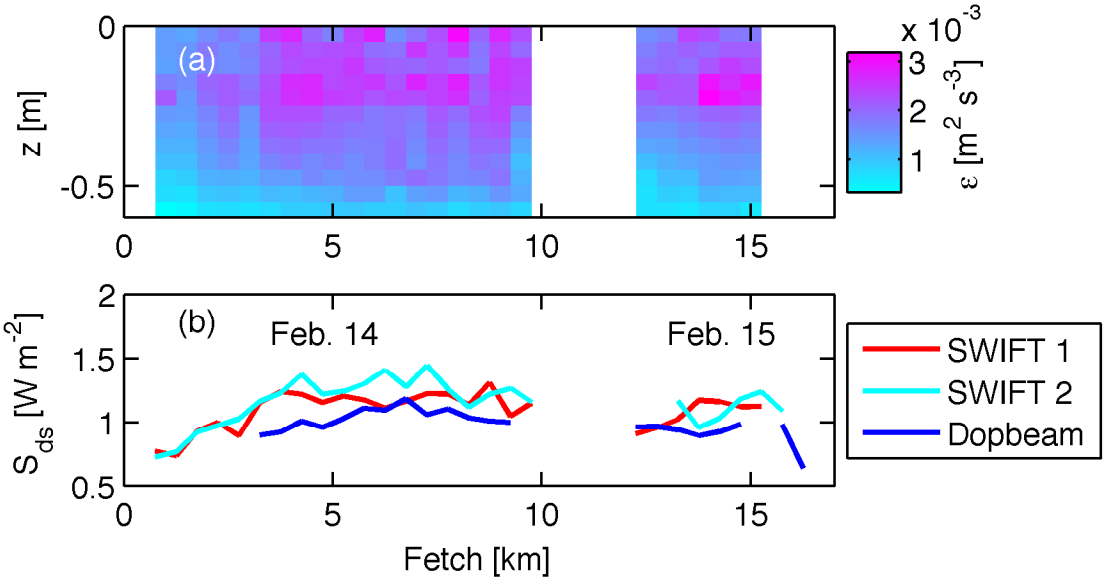

Figure 1.2: (a) Turbulent dissipation profiles from SWIFT 1 plotted with fetch. Depth, z, is measured from the instantaneous sea surface. (b) Total (integrated) turbulent dissipation measured by SWIFT 1 (red), SWIFT 2 (cyan), and Dopbeam system (blue) vs. fetch, averaged over 500 meters. The background dissipation level of 0.5 W m^{-2} has not been subtracted from these values, but is shown as the lower axis limit of panel (b).

Next, the wind, wave, and turbulence data were used to examine the local energy budget from the radiative transfer equation (Equation 1.7). Specifically, a "bulk" energy balance was evaluated, by integrating the spectral terms over all frequencies. The resulting balance is

$$\frac{\partial E}{\partial t} + c_g \frac{\partial E}{\partial x} = S_{in} - S_{ds}, \tag{1.16}$$

where E, c_g, S_{in}, and S_{ds} are now integrated variables. The above also assumes minimal surface currents and one-dimensional wave growth. Figure 1.5 gives estimates of the contribution from each of these terms, as a function of fetch. The uncertainty in each term was also estimated. For example, S_{in} was calculated from the parameterization of Terray et al. (1996), using the wind stress multiplied with an "effective" phase speed, c_{eff}, and the error bars reflect the uncertainty in c_{eff}. If the waves were purely fetch-limited (i.e. steady), the time

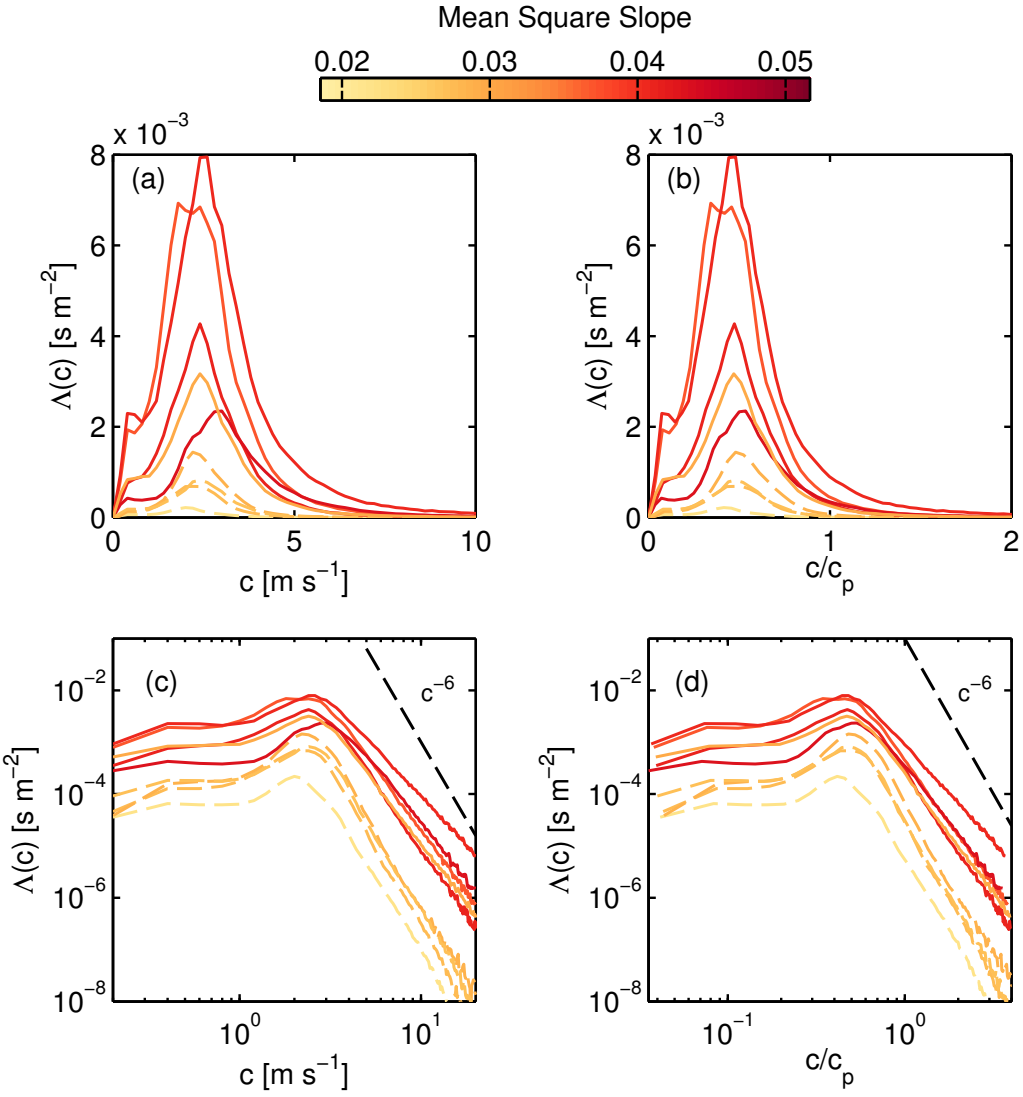

Figure 1.3: $\Lambda(c)$ vs dimensional (a,c) and non-dimensional (b,d) phase speed, in linear (a,b) and logarithmic (c,d) coordinates. All curves colored by mean square slope. Dashed curves are $\Lambda(c)$ results shown to be biased low by comparison with SWIFT breaking rate estimates. Black dashed line is the c^{-6} power law derived in Phillips (1985).

derivative on the left side of Equation 1.16 would be zero. However, the ramp up in the wind suggests that this assumption is not valid. The actual wave growth was somewhere in the range between pure growth in fetch, pure growth in time, and the sum of both growth rates.

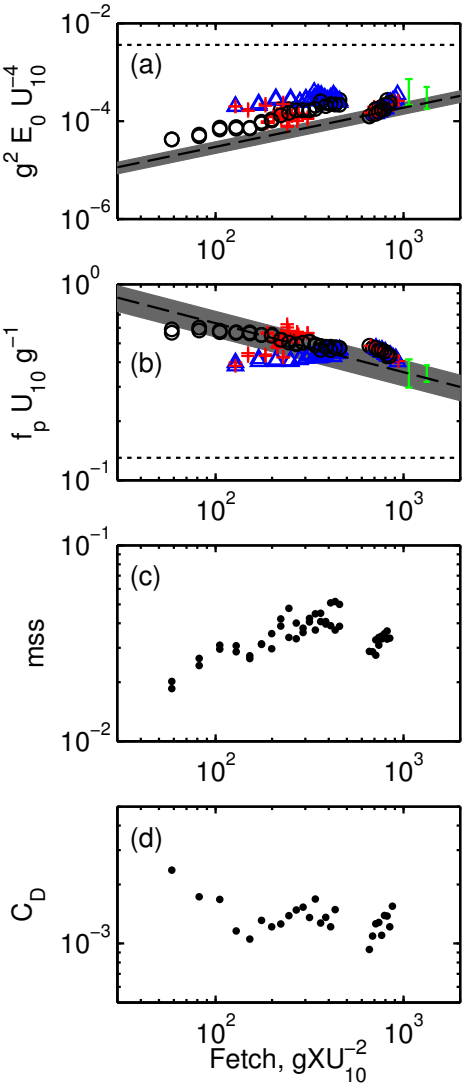

Figure 1.4: Evolution of four wave parameters plotted against non-dimensional fetch. (a) Non-dimensional wave energy. Black circles use the mean daily wind speed, blue triangles use a linear fetch-integrated wind speed, and red crosses use the instantaneous wind speed. Green symbols show the values from the NDBC #46088 wave buoy, with error bars for the minimum and maximum of the range of values. The Young (1999) empirical relation is shown by the black dashed line with gray range of parameters and fully-developed limits (horizontal solid black line). (b) Non-dimensional frequency, symbols as in (a). (c) Mean square slope. (d) Drag coefficient

From Equation 1.16, the net difference of these terms gives the dissipation from breaking. This inferred dissipation rate was compared with the integrated turbulent dissipation rate from the SWIFTs and Dopbeam array. The comparison is good overall, with the turbulence values lying in the range of the dissipation estimates needed to close the energy budget. There are a few regions of higher discrepancy, such as the largest fetches on February 14. Unfortunately, since the uncertainty in each of the wind, growth, and turbulent dissipation terms is significant, it is difficult to isolate the cause of these discrepancies.

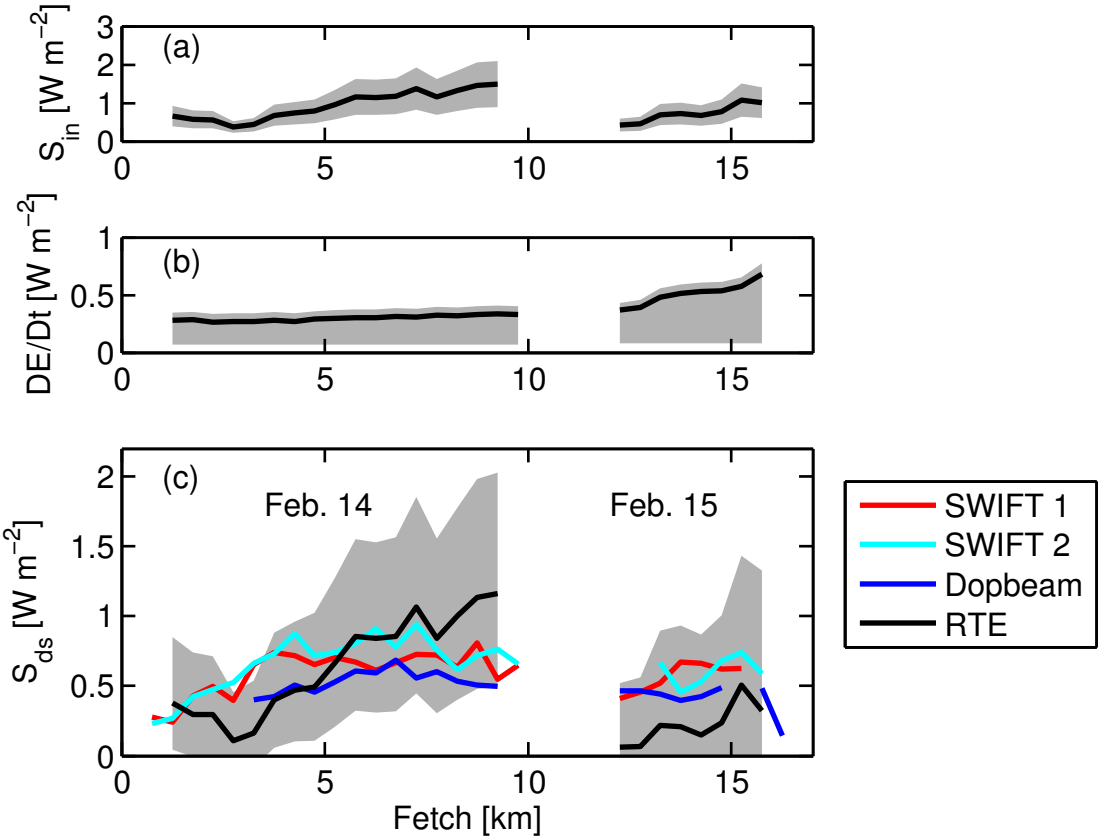

Figure 1.5: Evaluation and comparison of wave fluxes. Gray shaded regions show possible range of wind input (a), wave energy flux (b), and breaking dissipation (c) vs. fetch. Black lines come from a stationary assumption, $\partial E/\partial t = 0$, and using the mean value of $c_{eff} = 0.5c_p$. Colored curves of dissipation are calculated directly from turbulent dissipation for SWIFT 1 (red), SWIFT 2 (cyan), and Dopbeam (blue), with a background dissipation level of 0.5 W m^{-2} subtracted off. All quantities are 500-meter averages.

Each of the four estimates of S_{ds} from Figure 1.5 were then used, along with the measured $\Lambda(c)$, to evaluate the breaking strength parameter, b. The results are shown in Figure 1.6, as function of mean square slope, inverse wave age, and wave steepness from the significant wave height and peak wavenumber. Also shown are older data from Thomson et al. (2009), from young waves in Lake Washington and Puget Sound. It is clear that over the whole dataset, the breaking strength is not constant. Moreover, the trend with wave steepness is actually opposite that of the proposed correction from Drazen et al. (2008). Much of the remaining discussion centered on this incongruity.

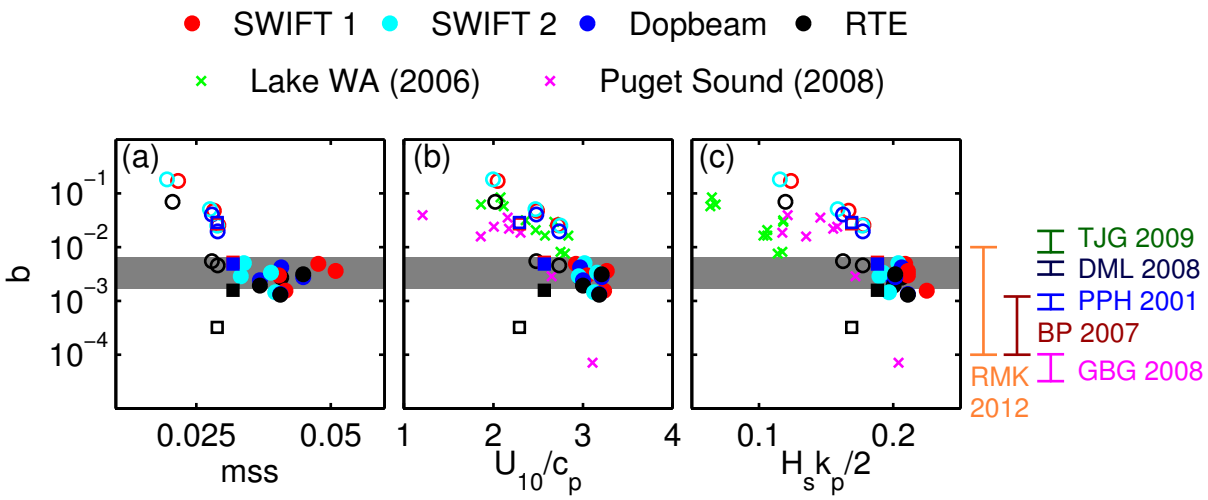

Figure 1.6: Breaking strength parameter, b, plotted against mean square slope (a), inverse wave age (b), and peak steepness (c). The data are colored by the source of S_{ds} in the calculation. Circles denote the first day of the experiment, and squares the second. Open symbols are used for data with known bias. Additional data from Lake Washington in 2006 (green crosses) and Puget Sound in 2008 (magenta crosses) described in Thomson et al. (2009). Vertical bars to the right of the plots show ranges of b estimates from Thomson et al. (2009) (green), Gemmrich et al. (2008) (pink), Phillips et al. (2001) (light blue), and Banner and Pierson (2007) (dark red). For Drazen et al. (2008) (dark blue), b is extrapolated to these steepness from their power law fit. For Romero et al. (2012) (orange), the approximate range of b for $c \leq c_p$ is shown.

On one hand, the variation in b might be predicted based on the similar variation across the literature. The range in b from several other papers is shown along the right of Figure 1.6. The experiment covered an unusually large range in wave development over a short time, which might explain why such large variations had not been seen before within a single study. The influence of microbreaking waves was a big question. Video taken from the SWIFT buoys indicated that smaller, less visible breakers were much more common at short fetches than could be detected in the ship-based imagery. It was theorized that in highly forced, young waves, the microbreaking might be a first-order source of dissipation, becoming less important as the waves developed. Thus, the microbreaking could be a biasing effect responsible for the large variation of b. Conversely, other sources of turbulence, such as from non-breaking waves, were examined but determined to be small by comparison. A detailed error analysis showed that b was also quite sensitive to several choices made during the processing of $\Lambda(c)$.

Finally, the shape of $\Lambda(c)$ was discussed and compared with the original Phillips (1985) theoretical prediction. Similar to Gemmrich et al. (2008), Thomson et al. (2009), and Kleiss and Melville (2010), the $\Lambda(c)$ curves peak at intermediate speeds somewhat less than the peak phase speed. At higher speeds, the decay of $\Lambda(c)$ resembles Phillips (1985) predicted c^{-6} shape, but this is not the wave regime where this equation should hold. At the low speeds where the Phillips (1985) theory is applicable, $\Lambda(c)$ does not resemble the prediction. The Romero et al. (2012) steepness correction based on the spectral saturation does not remedy this inconsistency. Although microbreaking is likely to be important, it was noted that several assumptions from Duncan (1981), Phillips (1985), and Drazen et al. (2008) had never been confirmed in the field.

1.5 Thesis Outline

In the remaining chapters, measurements of open ocean whitecaps are presented from two research cruises in the North Pacific Ocean. The organization is as follows:

Chapter 2 describes a method for stabilizing and georectifying ship-based imagery using

the distant horizon. In the first experiment, this algorithm is used to correct for the ship motion in the camera data, while in the second, it is used to synchronize the cameras with inertial motion data. This chapter is reproduced, with only minor changes to the introductory material, from the article:

> M. Schwendeman and J. Thomson. A horizon-tracking method for shipboard video stabilization and rectification. *J. Atmos. Ocean. Tech.*, 32:164176, 2015a. doi: 10.1175/JTECH- D-14-00047.1.

Next, Chapter 3 shows measurements of the whitecap coverage from both cruises, and compares them with shipboard wind measurements and buoy measurements of the waves and turbulent dissipation. It examines the issue of how best to parameterize the whitecap coverage. This chapter was published as:

> M. Schwendeman and J. Thomson. Observations of whitecap coverage and the relation to wind stress, wave slope, and turbulent dissipation. *J. Geophys. Res. Oceans*, 120, 2015b. doi: 10.1002/2015JC011196.

Chapter 4 introduces the ship-based stereo video system, present during the second experiment only. The stereo imagery is used to recreate, in three dimensions, the surface geometry during whitecapping. The focus is primarily on breaking onset, including a reevaluation of the Stokes limiting steepness and the conclusions of Holthuijsen and Herbers (1986). This work will be submitted for publication in the near future.

Finally, Chapter 5 summarizes the key findings of the earlier chapters, and concludes with a few speculative ideas and suggestions for future research directions.

Chapter 2

A HORIZON-TRACKING METHOD FOR SHIPBOARD VIDEO STABILIZATION AND RECTIFICATION[1]

2.1 Introduction

The use of digital video as a measurement tool has grown tremendously in recent years, as the cost of making and storing high-quality digital videos has decreased. Standard "electro-optical" (EO) video, which records visible light in the wavelengths spanning 400-700 nm, is part of a larger category of passive remote sensors, which also includes infrared (IR) cameras and hyperspectral imaging systems (Holman and Haller, 2013; Dickey et al., 2006). These passive systems complement the active remote sensors such as radar and lidar. Oceanographic applications of remote sensing include direct measurements of whitecap coverage (Callaghan and White, 2009) and sea ice concentration (Weissling et al., 2009). In addition, underlying properties such as wave dissipation, bathymetry, or currents can sometimes be inferred from remote measurements (Sutherland and Melville, 2013; Stockdon and Holman, 2000; Chickadel et al., 2003). Alternatively, hyperspectral measurements of optical properties of the upper water column (i.e. ocean color) may be used to determine concentrations of certain biological quantities (IOCCG, 2000).

Across these modes and applications, quantitative use of camera imagery benefits greatly from knowledge of the camera location and orientation, or "pose." Camera pose information is needed specifically for two common tasks: stabilization and rectification. Stabilization is the removal of camera motion from a set of images, resulting in images appearing as though recorded from a fixed camera. Rectification is the projection of one or more images into a

[1]This chapter was originally published in the Journal of Atmospheric and Oceanic Technology as:
M. Schwendeman and J. Thomson. A horizon-tracking method for shipboard video stabilization and rectification. *J. Atmos. Ocean. Tech.*, 32:164176, 2015a. doi: 10.1175/JTECH- D-14-00047.1.

common coordinate system. When images are projected to a map of the earth's surface, as from an airplane or satellite, it is commonly termed "orthorectification."

For a camera mounted to a fixed platform, the pose may be measured once and applied to all images. Such configurations are not often available at sea, but may sometimes be approximated in exceptionally stable ships (such as R/V FLIP, see Gemmrich et al., 2008; Zappa et al., 2012; Sutherland and Melville, 2013) or relatively calm conditions (e.g Thomson et al., 2009; Thomson and Jessup, 2009). Reliance on specific ships or conditions is not ideal, however, as it limits the availability of these measurements. Alternatively, the pose may be recorded continuously from an external system, usually an inertial motion unit (IMU). IMUs measure linear acceleration and angular velocity with a combination of accelerometers and gyroscopes. The position of the IMU is then estimated from dead reckoning. In Kleiss and Melville (2010, 2011) and Romero et al. (2012), an IMU was used to gather the positional data needed to rectify images taken from an airborne system. In Schwendeman et al. (2014), a shipboard camera was actively stabilized with an inertial pan-tilt system. There are two disadvantages of this strategy. First, inertial measurements are sensitive to noise and drift, such that accurate systems can be prohibitively expensive. Second, such systems require precise synchronization with the video frames, otherwise matching errors will occur.

A more attractive option is to use the video frames themselves to estimate the camera orientation. Problems of this type usually require ground control points (GCPs) with known x, y, and z coordinates (Szeliski, 2010). GCPs may be available in coastal applications when land makes up a significant portion of the camera field of view, as in Holland et al. (1997). In the open ocean, however, there are no GCPs.

In the following chapter, a method for determining the pitch and roll of a shipboard camera is described from the location of the horizon line in the image. Similar strategies have been used for stabilization of cameras for marine surveillance (Cao and Zhang, 2007; Morris et al., 2007; Fefilatyev et al., 2012) and unmanned aerial vehicle (UAV) flight control (Bao et al., 2005; Thurrowgood et al., 2009; Zhang et al., 2011). The focus here is on image rectification to sea surface coordinates for oceanic measurement tasks. One such application

is the calculation of the wave-breaking distribution $\Lambda(c)$ (Phillips, 1985). Calculating this distribution requires the measurement of the length, L, and speed, c, of many breaking wave events.

In Section 2.2, the horizon-finding method is described using an example image from a research cruise in the North Pacific. In Section 2.3, this algorithm is applied to the full video dataset and its performance is evaluated. The uncertainty and sensitivity in the method are examined in Section 2.4, using $\Lambda(c)$ as a case study. Finally, Section 2.5 concludes and points the user to a publicly-available Matlab toolbox for implementation of these algorithms.

2.2 Methods

The general problem of interest is outlined in Figure 2.1. A camera looks obliquely outwards over a flat sea surface from a known height H, at a constant heading (or azimuth), γ. The horizon line is unobstructed and visible in the image. The camera orientation is fixed except for two angles: pitch, ϕ, and roll, τ, which are unknown and are defined in the camera reference frame rather than the ship reference frame. Throughout the remainder of this paper, the incidence angle, $\sigma = \pi/2 - \phi$, is used rather than pitch, ϕ, for notational convenience in the calculations.

The ultimate goal of the following procedure is to determine σ and τ, such that it becomes possible to project a point located at pixel (u, v) to sea-surface coordinates $(x, y, -H)$, and visa versa. This goal will be achieved by relating the equation of the horizon line to σ and τ, as detailed below.

2.2.1 Data Collection

The images shown here were collected during a research cruise onboard the *R/V New Horizon* in the North Pacific in 2012. The ship sailed from San Diego to Ocean Station Papa (50°N, 145°W) and back over the course of three weeks. On twelve of these days, the ship held station for several hours to make a variety of wind and wave measurements. These measurements include approximately 48 hours of video, taken from a 3.6 mm "bullet" camera with 1/3"

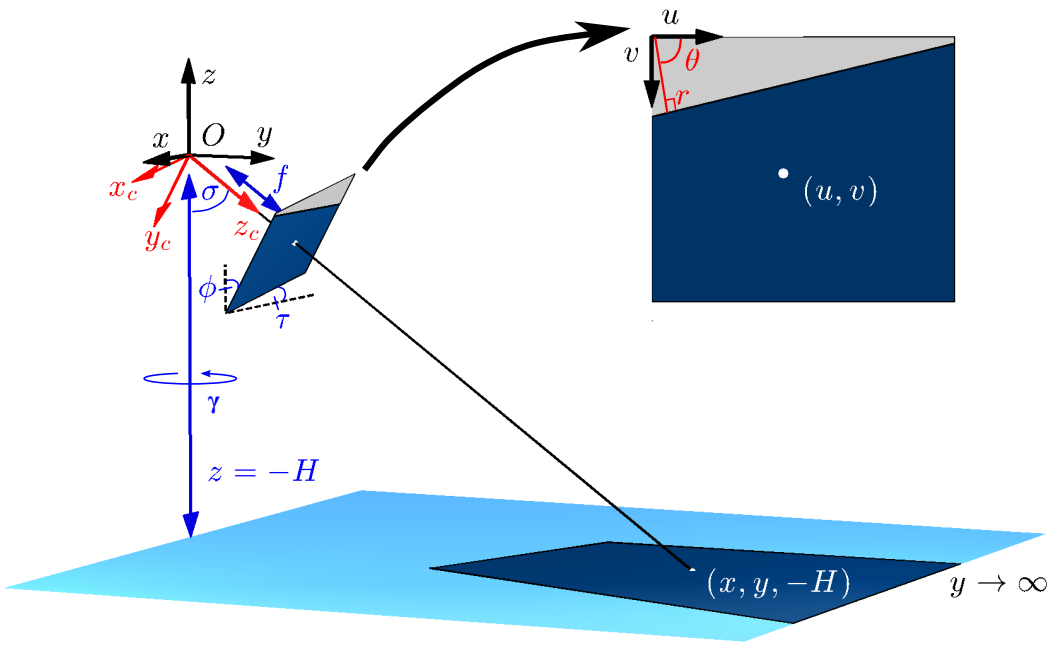

Figure 2.1: Problem schematic, defining the camera parameters and coordinate systems. The sea surface is shown in blue, with dark blue corresponding to the camera field-of-view, while gray areas denote sky. The small, rotated, square represents the camera sensor (not to scale), and the upper right square shows the resulting image.

Hi-Res Sony ExView B/W CCD. The data was sampled at 30 Hz and eight-bit grayscale, and compressed to MPEG-2 video. For the first half of the experiment, the camera was mounted on the top rail ($H = 10.7$ m) facing off the starboard side. On 7 October, it was moved to the ship centerline (still on the top rail) to be able to look off either port or starboard.

The camera was attached to a pan-tilt stabilization system (Directed Perception PTU-D100), which actively corrected for rotation in the incidence ($= 90° -$ pitch) and azimuth angles. This was the same stabilization package used in Schwendeman et al. (2014), in which a time-consuming manual horizon-finding method was used to compensate for the drift in incidence, while roll was left uncorrected. By using active stabilization, the camera

orientation is decoupled from the ship's pitch, roll, and heading angles. Therefore we must make the distinction that in the following sections, all angles are of the camera relative to the sea surface, which are unrelated to the ship's orientation. Although helpful in maintaining a given field of view, the active stabilization has been shown to be insufficient for quantitative processing of moving signals, such as breaking waves. This motivates the post-processing method that follows.

2.2.2 Horizon-Finding Algorithm

This image-based stabilization depends on an automated method for fast, robust, and accurate detection of the horizon line. Possible complications are poor lighting conditions, partial horizon views, and noise from features in the sea surface (e.g. whitecaps) and sky (e.g. clouds). As noted in Section 2.1, horizon detection has proven useful for a number of applications, and several strategies have been described in the literature. Recently, Fefilatyev et al. (2012) developed a "separation criterion" approach for finding the optimal horizon line from a rapidly-moving, buoy-mounted camera. While their problem requires a very robust detection algorithm, here we find that a simpler, faster approach is acceptable for our data and application.

Figure 2.2a shows an example video frame with the horizon clearly visible in the image. In Figure 2.2b, the image has been filtered with the Canny edge detector, which isolates and thresholds local maxima in the image gradient along the direction perpendicular to the gradient direction (Canny, 1986). Because the Canny detection method uses the gradient direction information, it has a number of advantages over other edge filters. First, the user can specify to return only the maximum pixel for a given edge (called "non-maximal suppression"), which leads to sharper edges. Additionally, the Canny detector can find connected edges with a lower threshold through hysteresis and edge linking (see Szeliski, 2010, for more details). Figure 2.2b shows the result of Matlab's Canny detector with an automated threshold that identifies 5% of pixels as edges.

Next, the binary edge image is passed to the Hough Transform, a widely-used method

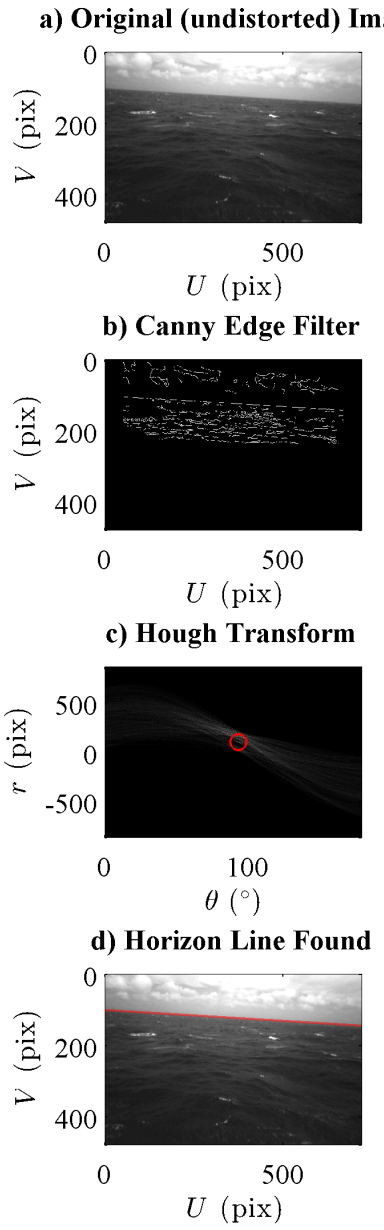

Figure 2.2: An example of the horizon-finding procedure, for a frame from 8 October, 19:58 UTC. (a) The original image after removal of distortion. (b) The binary image resulting from filtering with the Canny edge detector. (c) The Hough Transform accumulator array, with maximum value circled in red. (d) The original image with computed horizon line overlayed. For this image, the calculated camera angles are $\tau = 3.9°$ and $\sigma = 78.7°$.

for identifying lines in images (Duda and Hart, 1972; Illingworth and Kittler, 1988). In the Hough Transform, candidate lines are parameterized in polar coordinates by r, the distance of the line to the image origin, and θ, the direction of the line, as shown in Figure 2.1. Then, the number of edge pixels in the binary edge image is tallied along each line candidate. Thus, an "accumulator array" is assembled, whose elements each correspond to a line in (r, θ) space, and whose values equal the number of edge pixels located along this line. Since the horizon line is usually the longest or most prominent edge in the image, its r and θ parameterization corresponds to the maximum value of the accumulator array. Figure 2.2c shows the resulting accumulator array with the maximum value circled. Finally, Figure 2.2d shows the resulting line drawn on the original frame, exactly aligned with the horizon.

2.2.3 Projection Equations

With the horizon line found, the camera incidence and roll can be calculated from the camera projection equation (also called perspective transform or homography). The geometric basis for the projection equation is the pin-hole camera model, in which all light rays pass through a principal point, O, before hitting the sensor located one focal length, f, from O. Although the sensor physically lies behind the principal point, it can be easier to visualize the problem with it in front, as in Figure 2.1.

A necessary first step is to determine the camera's individual distortion coefficients and intrinsic parameters. This is done using a geometric calibration technique, based on the algorithms of Zhang (2000) and Heikkila and Silven (1997) that are available in the Matlab Computer Vision System Toolbox (or similar open source software packages). Distortion can be thought of as the deviation of the camera from an ideal pin-hole camera, and is often noticeable for wide-angle lenses. After correcting for distortion, the horizon is seen as a straight line in the image, as in Figure 2.2. Here, a distortion correction is used with two radial coefficients, no skew, and no tangential distortion, resulting in average errors of less than one pixel from a pin-hole camera. With distortion removed, the camera is fully characterized by 4 intrinsic parameters. The first of these are f_u and f_v, which are the

Table 2.1: Distortion coefficients and intrinsic parameters for the 3.6 mm "bullet" camera used in this experiment.

Parameter Name	Value
Number of columns, n_u	640
Number of rows, n_v	480
First radial distortion coefficient, κ_1	-0.601
Second radial distortion coefficient, κ_2	0.364
Focal length per pixel width, f_u	673.4
Focal length per pixel height, f_v	610.0
Image column center, c_u	339.2
Image row center, c_v	244.5

camera focal length expressed in terms of the pixel width and pixel height. The other two are c_u and c_v, which correspond to the (u, v) coordinates of the pixel located directly behind O, otherwise known as the image origin. The distortion coefficients and intrinsic parameters for the camera used in this experiment are listed in Table 2.1.

The invertible perspective equation for projecting real-world (x, y, z) coordinates to (u, v) pixel coordinates is,

$$s\,[u,\ v,\ 1,\ d]^T = [\,\mathbf{P}\,]\,[x,\ y,\ z,\ 1]^T \tag{2.1}$$

where $\mathbf{P}$ is the 4×4 "camera matrix," d is the inverse depth or "disparity," and s is an arbitrary scale factor. Eq. 2.1 can be inverted to find (x, y) from (u, v) by assuming $s = d = 1$, then normalizing the resulting (x_0, y_0, z_0) coordinates by $-z_0/H$, leading to coordinates at $(x, y, -H)$, i.e. the flat sea surface. For a pure rotation in incidence, σ, and roll, τ, the

form of $\mathbf{P}$ is

$$[\,\mathbf{P}\,] = \begin{bmatrix} f_u & 0 & c_u & 0 \\ 0 & f_v & c_v & 0 \\ 0 & 0 & 1 & 0 \\ 0 & 0 & 0 & 1 \end{bmatrix} \begin{bmatrix} \cos\tau & \sin\tau\cos\sigma & \sin\tau\sin\sigma & 0 \\ \sin\tau & -\cos\tau\cos\sigma & -\cos\tau\sin\sigma & 0 \\ 0 & \sin\sigma & -\cos\sigma & 0 \\ 0 & 0 & 0 & 1 \end{bmatrix} \tag{2.2}$$

where f_u, f_v, c_u, and c_v are the intrinsic parameters described above.

Angles σ and τ are uniquely determined by the location of the horizon line. In the limit of $y \to \infty$, Eq. 2.1 leads to u and v which lie along a straight line in the image corresponding to the horizon line, and defined by r and θ as found in the previous section. The equations relating these parameters are

$$\tau = \tan^{-1}\left(\frac{-f_u}{f_v \tan(\theta)}\right) \tag{2.3}$$

$$\sigma = \tan^{-1}\left(\frac{f_u \sin(\tau)\cos(\theta) - f_v \cos(\tau)\sin(\theta)}{r - c_u\cos(\theta) - c_v \sin(\theta)}\right). \tag{2.4}$$

Note that the above equations do not include the third camera angle, azimuth, given by γ in Figure 2.1. The azimuth angle may be needed for some applications if it varies significantly across images and directional information is required. Like camera height, however, azimuth cannot be determined with the horizon-finding procedure. Therefore it must be measured or estimated from some other data source, such as the ship's heading. With the pan-tilt stabilization system used here, the camera azimuth is kept relatively constant over timescales of several minutes, but this makes it independent of the ship's heading. We therefore define the line-of-sight of the camera to be at azimuth $= 0°$ unless otherwise noted.

Figure 2.3 demonstrates the rectification from image coordinates to world coordinates, for the same example as Figure 2.2. The red line again shows the accurately detected horizon line, which is used to measure roll and incidence. For the example shown, the camera was found to be oriented at 3.9° roll and 78.7° incidence. The blue rectangle in the original image maps to an oblique near-trapezoidal shape in earth coordinates.

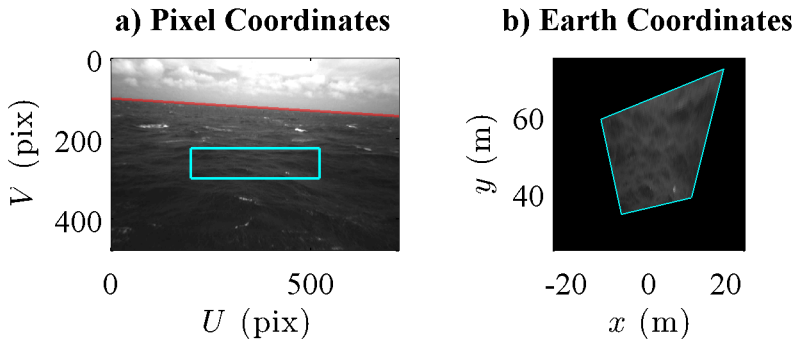

Figure 2.3: Example rectification using the image from Figure 2.2. (a) The image in pixel coordinates, with horizon detected correctly (red) and a sample rectangle (blue). (b) The projection of the pixels within the blue rectangle to earth coordinates.

2.3 Results

2.3.1 Horizon-finding Statistics

Next, we apply the method to the full dataset of 48 hours over 12 days. Images were subsampled at 30 second intervals, for a total of 5761 frames. Figure 2.4 shows 12 sample frames from this set, one for each day of the experiment. This figure demonstrates the robustness of the horizon-finding procedure over the large variety of lighting conditions seen during the experiment. The frames are then all projected as though taken from a stationary camera positioned at 0° roll and 75° incidence. Example videos showing this stabilization for several minutes at a time are also available as online supplemental material.

All 5761 processed images were manually reviewed and classified into one of three categories: horizon visible and correctly identified, horizon visible but incorrect, and horizon not visible. The results of this analysis are shown in Table 2.2, separated by date. The rightmost column of the table shows the percentage of frames in which a visible horizon has been correctly detected. The results totaled over the entire experiment are shown in the bottom row. Overall, 92.3% of visible horizon lines were correctly identified with the Hough Transform method.

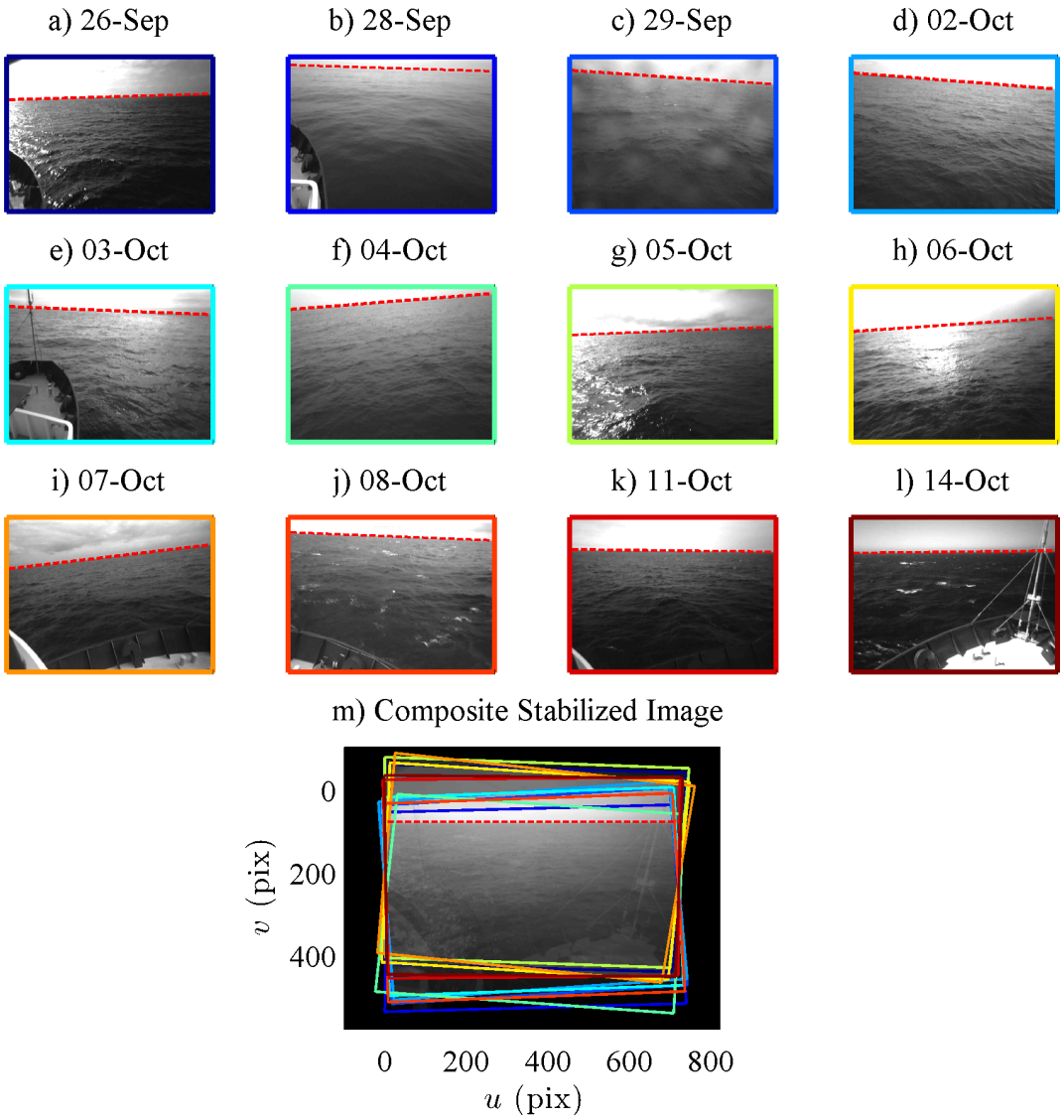

Figure 2.4: (a-l) 12 example video frames showing successful horizon detection (red dashed line), each from a different day of the experiment. (m) Composite image formed by transforming each image as though taken from a camera at 75° incidence and 0° roll, and averaging over all images. The red dashed line shows the expected horizon for this orientation, and the colored rectangles mark the outline of each transformed image.

Table 2.2: Horizon-finding results, separated by day, and totaled over the entire dataset. Images were output every 30 seconds, and manually classified. "Percent Correct" indicates the percentage of visible horizon lines that are correctly identified in the Hough Transform.

Date (2012)	Conditions	Horizon Visible, Correct	Horizon Visible, Incorrect	Horizon Not Visible	Percent Correct [%]
26-Sep	Partly Cloudy	208	17	29	92.4
28-Sep	Low Light Early	189	28	37	87.1
29-Sep	Occasional Rain On Glass	145	31	26	82.4
02-Oct	Partly Cloudy, Occasional Glare	470	8	30	98.3
03-Oct	Partly Cloudy, Late Glare	296	58	13	83.6
04-Oct	Mostly Cloudy	377	1	3	99.7
05-Oct	Clear, Frequent Glare	318	131	59	70.8
06-Oct	Partly Cloudy, Frequent Glare	299	74	8	80.2
07-Oct	Early Glare, Late Darkness	959	37	40	96.3
08-Oct	Partly Cloudy	898	1	5	99.9
11-Oct	Mostly Cloudy	330	0	1	100
14-Oct	Early Glare, Clear Later	598	38	0	94.0
Total		5086	424	251	92.3

The accuracy is quite variable over the experiment, reaching a minimum of 70.8% on 5 October, compared with a perfect 100% on 11 October. This accuracy is primarily a function of lighting, as noted in the "Conditions" column. The most unfavorable conditions are on clear or partly cloudy days when the sun is low in the sky, resulting in high glare and saturation of the image near the horizon. The worst days for these conditions are 5 October and 6 October. This motivated moving the camera to the ship centerline on 7 October, allowing the camera to be directed either port or starboard to avoid glare, thereby dramatically improving the horizon detection. Secondary effects include low light in the

early morning or evening and rain drops on the window of the camera housing.

2.3.2 Quality Control

It is crucial to be able to identify when the horizon finding fails, without relying on the manual inspection described above. Given a series of sequential images, it is possible to identify an incorrect horizon as an outlier from the expected smooth variation in σ and τ. Such a method is unsuitable, however, in cases where the horizon is rapidly moving or when non-sequential images are examined.

Instead, a predictive variable is defined to identify spurious horizons. Since the horizon is chosen as the maximum of the Hough Transform, then the prominence of this maximum is related to the strength of the horizon line. This first peak is compared with second highest peak, and the ratio of these peaks, m, is used as an inverse quality metric. To avoid values nearby to a prominent horizon, the second maximum is found a distance of $r > 10$ pixels and $\theta > 2.5°$ from the first peak. A ratio $m = 1$ indicates that both maxima are identical, whereas $m = 0$ corresponds to an infinitely large primary maximum.

The horizon-finding can fail for two reasons, namely: i) the horizon is not visible in the image, or ii) the horizon is not the strongest line in the image. In both cases, a large value of m is expected. Using the full data set of 5761 images, the ability of m to diagnose false horizons is examined. For a given threshold value, m_t, images with $m < m_t$ are predicted to be successful horizon identifications (positives), while images with $m > m_t$ are predicted failures (negatives). By comparing with the manual classification, images are characterized as true positives (TP), false positives (FP), false negatives (FN), and true negatives (TN). Positive predictive value (PPV), or "precision," is the ratio of true positives to all predicted successful horizon identifications,

$$\mathrm{PPV} = \frac{\mathrm{TP}}{\mathrm{TP} + \mathrm{FP}}. \tag{2.5}$$

Conversely, true positive rate (TPR), or "recall," is the ratio of true positives to all actual

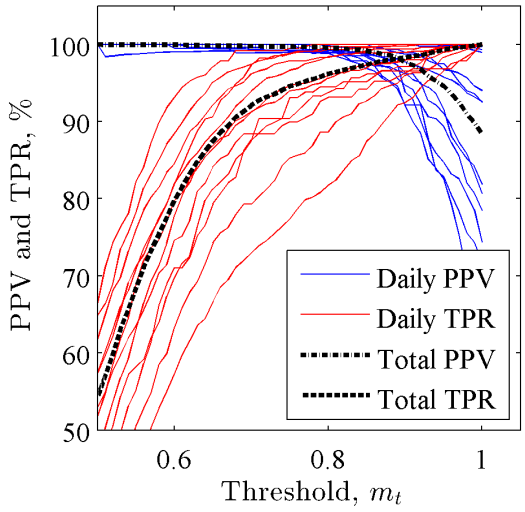

Figure 2.5: Plots of positive predictive value (PPV, or precision), and true positive rate (TPR, or recall) are plotted as a function of the threshold of the Hough Transform peak ratio, m_t. Thin curves in blue (PPV) and red (TPR) are daily values (12 lines each), while the dashed (PPV) and dash-dot (TPR) curves are for the full dataset.

successful horizon identifications,

$$\mathrm{TPR} = \frac{\mathrm{TP}}{\mathrm{TP} + \mathrm{FN}}. \tag{2.6}$$

Figure 2.5 shows the precision and recall curves made by varying m_t. Daily curves are shown, as well as for the full dataset. As with Table 2.2, the results are encouraging overall, but depend greatly on the individual day. For $m_t = 0.8$, the total PPV is 99.6% (4 false positives per 1000 predicted positives) and the total TPR is 96.2% (3.8% unnecessarily discarded images). For the same threshold, the minimum daily PPV and TPR values are 98.9% and 81.8%. Thus, if anything, this cut-off has the potential to be overly conservative when predicting failure in the horizon-finding algorithm.

2.4 Discussion

2.4.1 Uncertainty Analysis

Three uncertainties can be quantified in this method: the uncertainty in the horizon line, (r, θ), the uncertainty in camera angles, (σ, τ), and the uncertainty in the projected real-world coordinates, (x, y, z).

The uncertainty in (r, θ) can be due to the resolution of the camera, the chosen quantization in the Hough Transform, and uncertainty due to ambiguity in the horizon location. Camera intrinsic calibration indicates that the pinhole model is only accurate to within 1 pixel. Similarly, the Hough Transform is discretized by 1 pixel in r. The resolution in θ is specified by the user and was chosen here to be 0.5°, to reduce computation time and ensure robust statistics in the maximization.

Additionally, there is some uncertainty in the actual horizon location. The assumption made in deriving Eqs. 2.3 and 2.4 was of a horizon located infinitely far from the camera. For a number of reasons, including the curvature of the Earth and atmospheric scattering, the distance to the "apparent horizon" is actually finite (see French, 1982; Bohren and Fraser, 1986). Ignoring atmospheric effects, and assuming an observer height much less than the Earth's radius, the apparent horizon distance is

$$D \approx \sqrt{2RH}, \tag{2.7}$$

where R is the radius of the Earth and H is the height of the observer. So, for our camera located at $H = 10.7$ m, the distance to the apparent horizon is roughly 11.7 km. This distance can be shortened due to atmospheric scattering, which decreases the contrast between sea and sky (Bohren and Fraser, 1986). Alternatively, the distance can be lengthened as much as 10% due to atmospheric refraction (French, 1982).

Figure 2.6 shows the errors in r from assuming an infinite horizon, for $\sigma = 75°$, $\tau = 0°$, and $H = 10.7$ m. This camera pose is representative of a typical view during this experiment, and will be used repeatedly in the following analysis. At the estimated horizon distance of

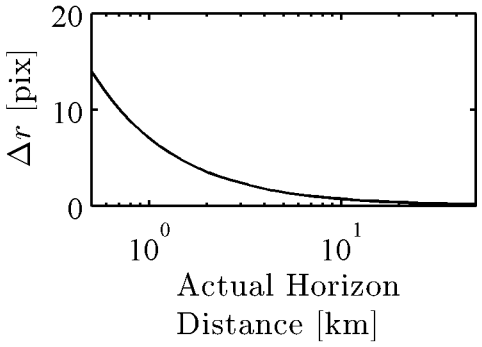

Figure 2.6: Uncertainty in image horizon location (Δr, in pixels) for finite horizon distances. The line shown is for $\sigma = 75°$, $\tau = 0°$, and $H = 10.7$ m.

11.7 km, the error in r is only 0.6 pixels, which is less than the uncertainty noted above. As the apparent horizon nears the camera, the horizon appears lower in the image, and the errors in r increase. This error is not sensitive to changes in σ, but scales proportional to H. Since D scales with $H^{1/2}$, these errors will become slightly more pronounced for higher cameras. This plot is also useful in estimating the errors stemming from using the horizon information under non-ideal conditions. For example, if a coastline obscures the horizon at a distance of 1 km, an error of 6 pixels can be expected in r.

The uncertainty in σ and τ is directly related to the uncertainty in r and θ through Eqs. 2.3 and 2.4. Around the reference orientation ($\tau = 0°$, $\sigma = 75°$), an error of $\pm 0.5°$ in θ leads to errors of $\pm 0.55°$ in τ and $\pm 0.26°$ in σ. Around the same value, errors of ± 1 pixel in r have no effect on τ, but correspond to errors of $0.09°$ in σ. Therefore, under ideal lighting, the horizon method as described here is accurate to within $0.6°$ in τ and $0.3°$ in σ.

In Section 2.2, it was shown that the projected coordinates (x, y, z) are functions of the pixel coordinates (u, v), the intrinsic parameters (f_u, f_v, c_u, c_v), the camera angles (σ, τ, γ), and the camera height, H. Since z of the water surface is taken to be $-H$, the uncertainty in z is simply equal to the uncertainty in H. However, the errors in x and y are functions of

the uncertainties of all the parameters,

$$\begin{aligned}\Delta x = x\left(u, v; H + \Delta H, \sigma + \Delta\sigma, \tau + \Delta\tau, \gamma + \Delta\gamma, f_u, f_v, c_u, c_v\right) \\ -x\left(u, v; H, \sigma, \tau, \gamma, f_u, f_v, c_u, c_v\right),\end{aligned} \tag{2.8}$$

$$\begin{aligned}\Delta y = y\left(u, v; H + \Delta H, \sigma + \Delta\sigma, \tau + \Delta\tau, \gamma + \Delta\gamma, f_u, f_v, c_u, c_v\right) \\ -y\left(u, v; H, \sigma, \tau, \gamma, f_u, f_v, c_u, c_v\right).\end{aligned} \tag{2.9}$$

Potential errors in f_u, f_v, c_u, and c_v are not addressed here based on the positive results of the calibration procedure, which showed average errors of less than one pixel in the calibration images. In the section above it was shown that after stabilization, the error in incidence and roll angles were on the order of $\Delta\sigma \sim 0.3°$ and $\Delta\tau \sim 0.6°$. The horizon technique cannot be used to estimate H and γ, so these uncertainties must be estimated from other sources. ΔH is a function of the sea surface elevation variability, or wave height. During this experiment, the average wave height was roughly 2 m, which will be used as a representative value of ΔH. The specifications for the pan-tilt stabilization unit give azimuth errors of $\Delta\gamma < 0.25°$ for underlying sine-wave motions at 1 Hz, although the system tended to drift in azimuth on longer timescales.

Figures 2.7 and 2.8 show the errors in x and y resulting from these sources, around the reference state of $\sigma = 75°$, $\tau = 0°$, $\gamma = 0°$, and $H = 10.7$ m. Figure 2.7 shows the camera field-of-view in pixel coordinates, with the area above the horizon colored gray. Pixels are colored by error components Δx and Δy for the errors in τ, σ, γ, and H discussed above. In Figure 2.8, these errors are shown as a function of y, for vertical slices in the left, middle, and right of the image. The errors grow as y increases for both components and all uncertainty sources. For all sources except γ, uncertainty in y is larger than in x. The most severe source of error is in Δy due to ΔH. For uncertainty in H, the relative errors, $\Delta y/y$ and $\Delta x/x$, are equal to $\Delta H/H$, or 18.6% in this case. So at a distance of 100 m, Δy is nearly 20 m for $\Delta H = 2$ m, whereas all other errors are less than 5 m at this distance. Although this error analysis was performed around one camera pose, with single values for $\Delta\tau$, $\Delta\sigma$, $\Delta\gamma$, and ΔH, it would be easy to adapt this procedure to different camera views and error

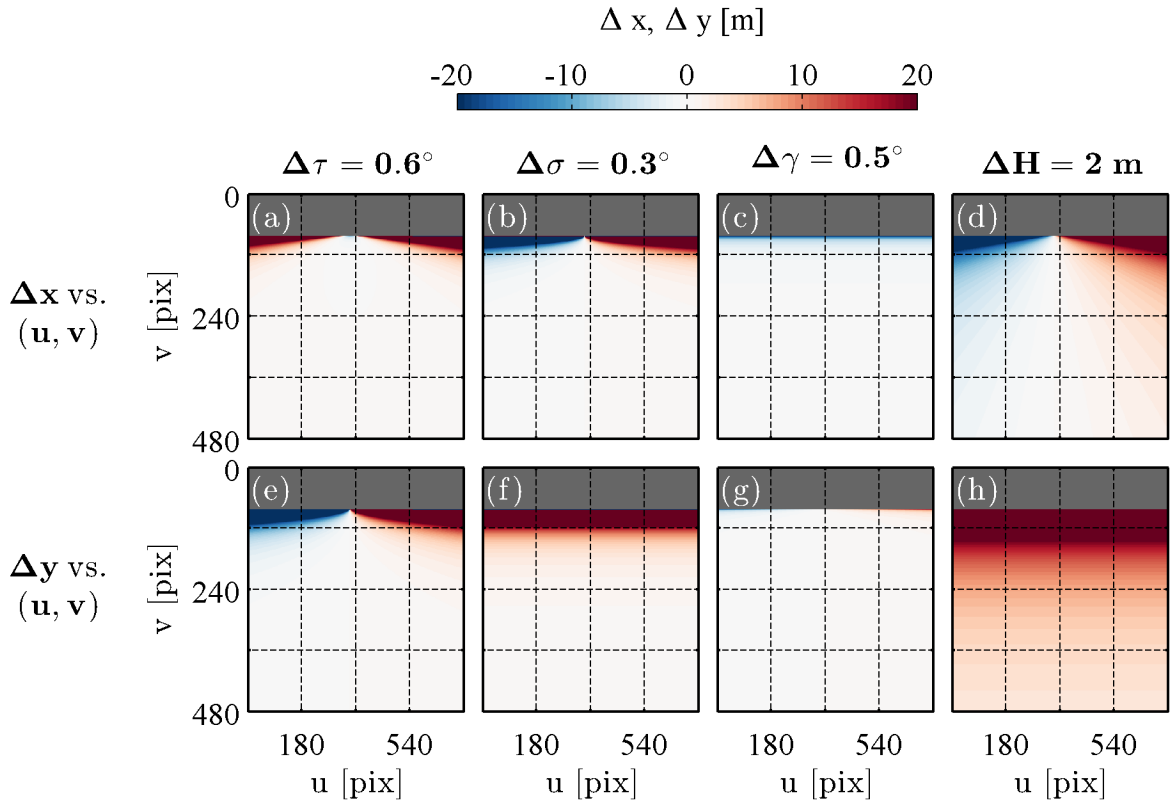

Figure 2.7: Uncertainty in rectification around a reference camera orientation of $\sigma = 75°$, $\tau = 0°$, $\gamma = 0°$, and $H = 10.7$ m. The errors are shown in x (a-d) and y (e-h) at each pixel (u, v) for corresponding errors of $\Delta\tau = 0.6°$ (a, e), $\Delta\sigma = 0.3°$ (b, f), $\Delta\gamma = 0.5°$ (c, g), and $\Delta H = 2$ m (d, h). The gray region represents the pixels above the horizon in the image.

magnitudes.

2.4.2 Uncertainty in $\Lambda(c)$

Figure 2.7 demonstrates that errors in the assumed camera height can lead to large uncertainties during rectification, even after stabilization in roll and incidence. The manifestation of these uncertainties will vary depending on the application. As a case study, we demonstrate the result of such errors on estimates of the breaking wave distribution, $\Lambda(c)$, a common remotely-sensed wave measurement (see, for example, Gemmrich et al., 2008; Thomson et al.,

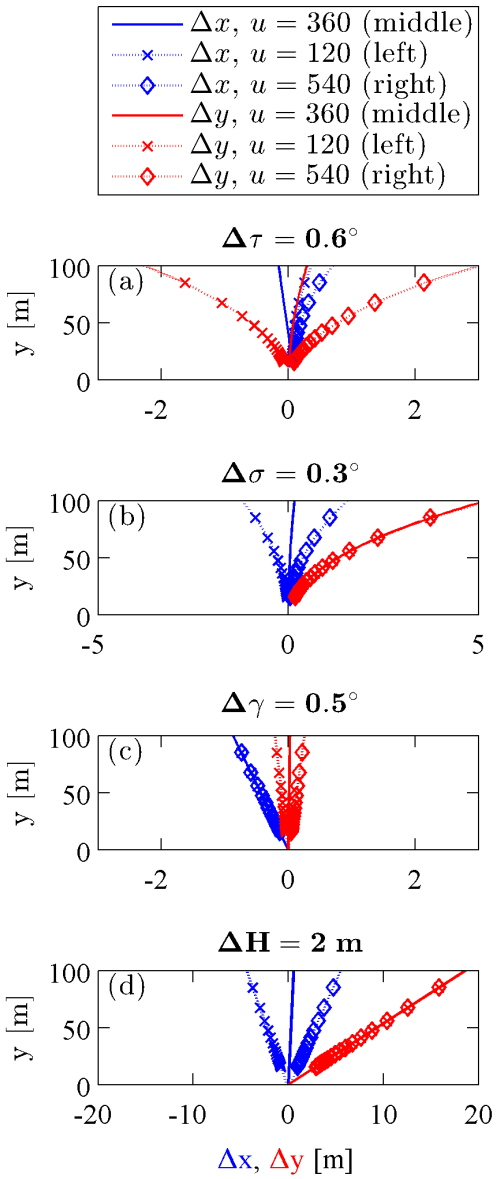

Figure 2.8: Uncertainty in rectification around a reference camera orientation of $\sigma = 75°$, $\tau = 0°$, $\gamma = 0°$, and $H = 10.7$ m. The Δx (blue) and Δy (red) errors are shown as a function of distance from the ship (y) for corresponding errors of $\Delta\tau = 0.6°$ (a), $\Delta\sigma = 0.3°$ (b), $\Delta\gamma = 0.5°$ (c), and $\Delta H = 2$ m (d). Curves are plotted for three constant pixel columns, corresponding to lines in the middle ($u = 360$, solid line), left ($u = 120$, dotted line with crosses), and right ($u = 540$, dotted line with diamonds) of the image.

2009; Kleiss and Melville, 2010; Schwendeman et al., 2014).

$\Lambda(c)$ is defined as the sum of all breaking wave crest lengths per unit area and speed. It has become commonly used in estimating wave energy dissipation due to breaking (see Phillips, 1985). Calculation of $\Lambda(c)$ requires the estimation of wave crest length, L_i, and speed, c_i, for many breaking events. Then the calculation is carried out by binning the events by c_i, summing over L_i, and applying the proper normalization. The final formula for $\Lambda(c)$ is

$$\Lambda(c) = \frac{\sum_i L_i}{ANdc} \tag{2.10}$$

where N is the total observed events, A is the spatial domain, and dc is the speed bandwidth such that the summation is over all L_i with speeds $(c - dc/2) < c_i < (c + dc/2)$. If the breaking waves are observed from a moving camera, it is clear that estimates of the crest lengths and speeds will be affected by the camera motion, but it is not apparent how these errors will propagate through the $\Lambda(c)$ computation.

The sensitivity of $\Lambda(c)$ to errors of this kind can be examined through the use of synthetic data. These synthetic data have a known distribution of L and c, making errors easy to determine. Moreover, in practice there are many subtle variations for determining L_i and c_i, which are mostly avoided with the synthetic data. The creation of the synthetic data proceeds as follows: Line segments with constant length 2 m are randomly given a starting position within a domain of 30 m $< y <$ 50 m and -10 m $< x <$ 10 m. They are assigned a speed from a Gaussian distribution centered around 3 m/s with standard deviation of 1 m/s. They are propagated forward with that speed, over a duration of 2 s, with their position recorded every $dt = 1/(15$ Hz). Next, these crests are "observed" from a camera at the familiar pose of $\sigma = 75°$, $\tau = 0°$, $\gamma = 0°$, and $H = 10.7$ m. The camera is subject to a sinusoidal oscillation in height, with $\Delta H = 2$ m (i.e. amplitude of 1 m), at a period of $T = 4$ s, to simulate a shipboard camera in a rough sea state. Each wave crest is randomly given a start time, which determines the camera phase during the event. The "observer" is not aware that the camera height is changing, however, and therefore attributes the camera

motion to the crests themselves. Examples of true and apparent crest motions are shown in Figure 2.9a,b for two scenarios: crests moving directly across the image, in the $+x$ direction, or directly away from the camera, in the $+y$ direction.

Figure 2.9c,d shows the results of calculating $\Lambda(c)$ as in Eq. 2.10 for the true and apparent crest motion. Over 10,000 crests were simulated in each case to ensure robust statistics. In making Figure 2.9c, L_i is calculated as the Δy between the two endpoints of the crest, and c_i is $\Delta x/dt$ (visa versa for Figure 2.9d). The true $\Lambda(c)$ distribution is shown in black. Five cases are tested for each scenario, the first being the base case from Figures 2.9a,b ($\Delta H = 2$ m, $T = 4$ s), in blue. The red line shows the results for halving ΔH ($\Delta H = 1$ m, $T = 4$ s), and the green line for doubling T ($\Delta H = 2$ m, $T = 8$ s). The cyan curve is a low motion case ($\Delta H = 0.25$ m, $T = 4$ s). The magenta distribution is for a similar scenario, with the exception that the camera is looking down from a nadir position ($\sigma = 0°$).

The results from the synthetic data lead to a number of conclusions. First, in all cases, sinusoidal errors in camera height tended to broaden the observed $\Lambda(c)$ from the true distribution, while the total sum of breaking crests (equal to the integral of $\Lambda(c)$) stayed within 1%. Thus, the measurement of crest length was unbiased by the camera motion, but the crests speeds were biased towards more extreme values. This is especially true for the scenario with crests moving away from the camera, where for the large camera motions, the peak is obscured completely. This orientation appears to be a worse-case scenario for observing $\Lambda(c)$, although the errors may be manageable for lower sea states, as the $\Delta H = 0.25$ m case shows. For both geometries, the curves are nearly identical for halving wave height (red) as for doubling wave period (green), suggesting that the errors scale with the vertical velocity of the camera motion. Finally, these plots show that the errors are not restricted to oblique views, and in fact are as large for nadir camera orientations (magenta) as for x-propagating crests under similar sea states (left, blue).

It should of course be noted that the above case study is an idealized model for shipboard camera motion. The relationship between sea state and ship motion will depend greatly on the ship, and in most cases the vertical motion of the camera will be less than the significant

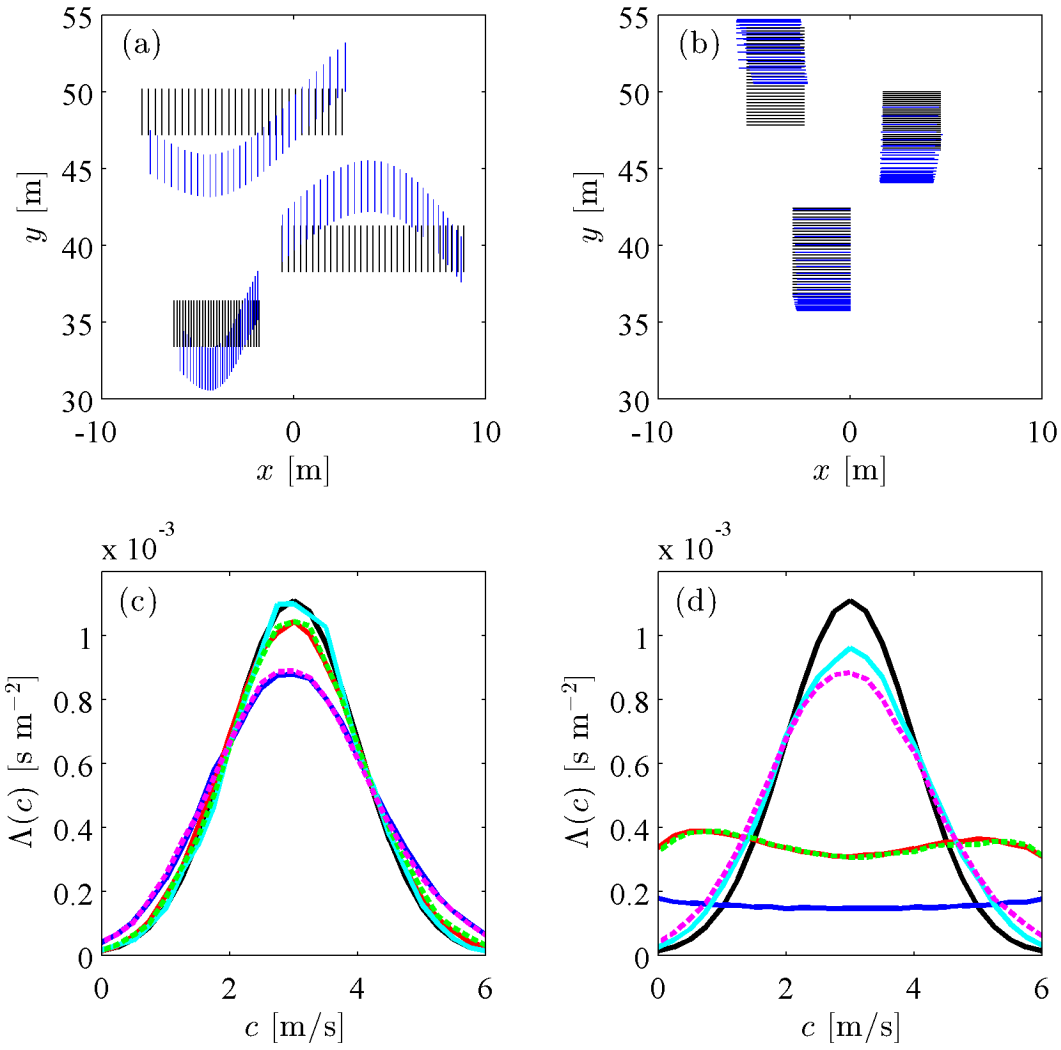

Figure 2.9: Error in $\Lambda(c)$ due to varying camera height with synthetic breaking waves, for (a, c) breaking waves propagating in the $+x$ direction, and (b, d) breaking waves propagating in the $+y$ direction. (a, b) Three examples of the true breaker propagation (black) and the apparent propagation (blue) for sinusoidal camera motion of $\Delta H = 2$ m at $T = 4$ s. (c, d) The resulting $\Lambda(c)$ for gaussian input centered at 3 m/s (black), for $\Delta H = 2$ m, $T = 4$ s (blue), $\Delta H = 1$ m, $T = 4$ s (red), $\Delta H = 2$ m, $T = 8$ s (green, dashed), $\Delta H = 0.25$ m, $T = 4$ s (cyan), and $\Delta H = 2$ m, $T = 4$ s, at $\sigma = 0°$ (i.e. nadir) (magenta, dashed).

wave height. Additionally, the frequency of camera motion will depend on the size of the ship relative to components in the incident wave spectrum. However, even for a camera without any underlying motion, there are uncertainties in this rectification due to projecting a wavy sea surface onto a flat plane. Acceptable uncertainties will vary with application; these simulations of $\Lambda(c)$ suggest that camera height variations less than 1 m are necessary for high quality results.

2.4.3 Limitations

Here we summarize the limitations of this horizon stabilization method, many of which have already been mentioned. The most fundamental requirement is that the horizon be visible in the camera field-of-view. This is not guaranteed if the platform is subject to large motions or the camera lens has a narrow field-of-view. The accuracy assessment reveals that the method is especially sensitive to the lighting conditions (see Table 2.2). Possible complications include glare from direct or reflected sunlight, and lack of contrast due to low light, heavy clouds, or rain. Furthermore, the Hough Transform detection method requires the horizon to be the most well-defined line in the image, meaning obstacles or other instrumentation in the field-of-view may impede its detection. In that case, one of the several other horizon detection algorithms (for example: Bao et al., 2005; Morris et al., 2007; Zhang et al., 2011; Thurrowgood et al., 2009; Moore et al., 2011a; Fefilatyev et al., 2012) may be more suitable. Finally, if a coastline is used in place of the horizon, at distances less than roughly 10 km, the camera angle calculation will be negatively impacted, as shown Figure 2.6.

The horizon only provides information on the camera incidence and roll angles, and cannot be used to calculate the heading angle and x, y, and z position. On large ships and in low sea states, as in this dataset, the assumption of small motions in these other degrees-of-freedom may be reasonable. The two most problematic of these unknowns are the heading and camera height, because small errors in these variables lead to rectification errors which become large as the distance from the camera increases (as shown in Figures 2.7 and 2.8). One option is to use some combination of GPS, IMU, and magnetic compass data to estimate these

other motions. Here, the overlapping pitch and roll estimates from the video and GPS/IMU may be useful simply to synchronize the data streams. This unfortunately does not solve the issue of noise (at short timescales) and drift (at longer timescales) that these systems can suffer from. Ideally, the camera frames themselves could also be used to estimate these other variables. Towards that end, Moore et al. (2011b) and Thurrowgood et al. (2014) showed that by using two cameras with fisheye lenses oriented skyward, they could create a "visual compass" — a nearly complete sky panorama which they could compare with an individual view to calculate the relative heading of their UAV. Unfortunately, our limited view of the sky in this dataset make this approach challenging, but future experiments may take advantage of this method. Similarly, the height of the camera could be estimated visually using a stereo camera system and fitting a plane to the three-dimensional points on the water-surface, as in Benetazzo (2006). This assumes that the camera field-of-view covers a sufficiently large footprint that the fitted plane approximates the mean water level. Note also that this provides its own estimate of the camera pitch and roll, potentially making the horizon method redundant. However, stereo imaging brings with it a host of significant processing challenges, and thus researchers may still be drawn to this relatively simple method if the conditions are suitable.

2.5 Conclusion

The horizon line, if it is visible and unobstructed, can be used to calculate the incidence (or pitch) and roll angles of shipboard cameras in the absence of stationary ground control points or external IMU systems. The Hough Transform is shown to be a robust and computationally efficient means for horizon detection, and a derived quality control metric is effective for isolating spurious horizons. Upon detecting the horizon, the conversion to the incidence and roll of the camera is exact, and given in Eqs. 2.3 and 2.4. The performance of the horizon tracking is largely dependent on the lighting conditions.

For images shown here, the uncertainties in incidence and roll were determined to be on the order of 0.3° and 0.6°, respectively. The effect of horizon distance is negligible in this case,

though larger uncertainties are possible if the apparent horizon is within a few kilometers of the camera due to poor atmospheric conditions or distant land. The largest source of uncertainty in rectification is due to camera height variations from waves. The percent errors in x and y are similar to the ratio of $\Delta H/H$. These errors can in turn negatively affect estimates of such quantities as $\Lambda(c)$, due to the biasing of wave crest speeds.

The implementation of our method in Matlab is available as an open source toolbox via the Matlab File Exchange under the name "Horizon Stabilization." The package includes all codes for horizon detection, image stabilization, rectification, and error analysis. These codes require either the Matlab Computer Vision System Toolbox or the Image Processing Toolbox for implementation of the Hough Transform.

Chapter 3

OBSERVATIONS OF WHITECAP COVERAGE AND THE RELATION TO WIND STRESS, WAVE SLOPE, AND TURBULENT DISSIPATION[1]

3.1 Introduction

Whitecaps are a primary mechanism associated with many of the interactions between the atmosphere and the ocean. They drive mixing near the air-water interface, and facilitate the transfer of energy, momentum, heat and mass (Melville, 1996). This makes whitecapping a critical component of the global climate system (Cavaleri et al., 2012). Since whitecaps dissipate surface wave energy, primarily in the form of turbulence and bubble production, they are also fundamentally important in the evolution of the wavefield. Therefore, understanding the energetics of the whitecaps is critical for improving upon the present operational wave forecasts (Cavaleri et al., 2007).

Whitecaps are a visual signature of breaking waves. Wave-breaking is a complex nonlinear phenomenon, which occurs at scales much smaller than most global ocean models can resolve. Therefore, breaking is often implemented using empirical parameterizations based on field observations. Toward that end, we present observations of open-ocean whitecapping, accompanied by concurrent wind, wave, and turbulent dissipation measurements.

A common visual measurement of wave-breaking is the whitecap coverage, W, which is the average fraction of sea surface covered by whitecaps. Whitecap coverage is frequently characterized as a function of the 10-meter wind speed, U_{10}, since measurements or hindcasts

[1]This chapter was originally published in the Journal of Geophysical Research - Oceans as:
M. Schwendeman and J. Thomson. Observations of whitecap coverage and the relation to wind stress, wave slope, and turbulent dissipation. *J. Geophys. Res. Oceans*, 120, 2015b. doi: 10.1002/2015JC011196.

of U_{10} are often readily available. Common parameterizations are power law functions,

$$W = aU_{10}^{n}, \tag{3.1}$$

or cubic equations,

$$W = a(U_{10} - b)^{3}. \tag{3.2}$$

Unlike the power law, the cubic equation contains a threshold, b, below which there is no visible whitecapping. Conversely, the power law allows for variation of the exponent of wind speed, n.

Aggregating the many reported fits to U_{10}, as in Anguelova and Webster (2006), shows variability in predicted whitecap coverage of orders of magnitude across all wind speeds. Such fits date back decades (e.g. Monahan, 1969), so it is possible that some of this scatter is due to differences in experimental methods over the years. Most conspicuously, early W estimates required manual inspection of a limited collection of photographs, while modern studies tend to use large batches of digital imagery and pixel-wise thresholding techniques (see Callaghan and White, 2009; Kleiss and Melville, 2011). In addition, images have been used from a variety of geometries and instrumentation, leading to significant differences in resolution and image quality.

Still, it is likely that some of the variability in the literature fits of W to U_{10} has physical origins. For example, the wind stress, τ, is a better descriptor of the wind energetics, and is less sensitive to atmospheric stability effects. Thus, the wind friction velocity, $u_* = \sqrt{\tau/\rho}$, is often used in place of U_{10}. Furthermore, several recent studies have shown variations in W related to wave age (Sugihara et al., 2007), wave height (Stramska and Petelski, 2003), and wind history (Callaghan et al., 2008a). This is not surprising, since the process of wave-breaking is almost entirely driven by wave mechanics, rather than direct wind forcing (Babanin, 2011).

The wave steepness, or slope, is fundamentally important to breaking, therefore average wave slope parameters have often been proposed to replace wind variables in parameteriza-

tions of whitecapping. Bulk wave steepness variables commonly take the form

$$S = \frac{Hk}{2}, \tag{3.3}$$

where H and k are a characteristic wave height and wavenumber. The significant wave height, H_s, is often used for H. Alternatively, Kleiss and Melville (2010) found good correlation between W and steepness using a peak wave height,

$$H_p = 4\left[\int_{0.7f_p}^{1.3f_p} E(f)df\right]^{1/2}, \tag{3.4}$$

based on the work of (Banner et al., 2000). Here, f_p is the frequency at the peak of the omnidirectional spectrum, $E(f)$. The corresponding peak wavenumber, k_p, is often used for the characteristic wavenumber value. Peak variables such as f_p, k_p, and H_p are easily defined in unimodal seas, as in fetch-limited conditions. However, wave spectra from the open ocean routinely exhibit several apparent peaks at different frequencies. Therefore, the energy-weighted mean frequency, f_m, is sometimes used instead:

$$f_m = \frac{\int fE(f)df}{\int E(f)df}. \tag{3.5}$$

Similar definitions can be written for mean wavenumber, k_m, and wave height H_m. Note that the cyclic wavenumber, rather than radial wavenumber, is used throughout this paper.

However, measurements of the propagation speeds of whitecaps indicate that most whitecaps are associated with waves shorter than the peak or mean waves (see Gemmrich et al., 2008). On average, these waves are much steeper than the dominant waves or swell waves. Therefore, other wave slope variables are often used to describe the energy in the short to intermediate wind waves, i.e. the spectral "tail."

To describe the breaking probability at a desired frequency scale, Banner et al. (2002) used the azimuth-integrated spectral saturation,

$$B(f) = k^4E(k) = \frac{(2\pi)^4f^5E(f)}{2g^2}. \tag{3.6}$$

The spectral saturation is related to wave steepness through its association with the mean square slope (mss). Given a range in frequency, $f_1 < f < f_2$, the mss of the waves in these frequencies can be calculated as

$$mss = \int_{f_1}^{f_2} \frac{2B(f)}{f} df. \tag{3.7}$$

In addition, Banner et al. (2002) showed better consistency in their results after normalizing $B(f)$ by the directional spread, $\Delta\theta(f)$. A number of studies have since used the mss or mean saturation ($\overline{B}$), either normalized or unnormalized, to parameterize breaking (Kleiss and Melville, 2010; Gemmrich et al., 2013; Hwang et al., 2013).

It has frequently been suggested that a better dynamic predictor of W is the rate of energy dissipation from wave-breaking, S_{ds}. The idea was proposed early on by Cardone (1970) to correct for atmospheric stability effects in the data of Monahan (1969). Kraan et al. (1996) derived a theoretical prediction for W based on the WAM dissipation source function and a JONSWAP spectrum, which showed reasonable agreement with their measured whitecap coverage. Hanson and Phillips (1999) used estimates of dissipation from the Phillips (1985) equilibrium range theory, and showed improved correlation over U_{10} fits. Most recently, Hwang and Sletten (2008) derived a dissipation parameterization based on a total equilibrium with wind energy input. Using a collection of whitecap coverage measurements, they proposed a linear fit of the form

$$W = a(S_{ds} - b). \tag{3.8}$$

Much of the energy lost from the waves during breaking is dissipated as turbulence in the ocean surface layer. In measurements, this is seen as a region of "enhanced dissipation," above a standard logarithmic boundary layer (Craig and Banner, 1994). Gemmrich (2010) found most of the breaking turbulence to be concentrated in the very near-surface, especially in the wave crest. Thomson (2012) introduced a drifting measurement platform called the SWIFT (Surface Wave Instrument Float with Tracking), which is designed to measure the near-surface dissipation profile, $\epsilon(z)$, in a wave-following reference frame. Schwendeman et al.

(2014) used SWIFTs to measure $\epsilon(z)$ for fetch-limited waves in the Strait of Juan de Fuca. They showed good agreement between the wave dissipation rate based on a fetch-limited energy balance, and the integrated turbulent dissipation,

$$S_{ds} \approx \rho_w \int \epsilon(z) dz. \tag{3.9}$$

Sutherland and Melville (2015) measured turbulent dissipation from the R/V FLIP using a combination of sub-surface acoustic measurements and stereo infrared (IR) imagery of the sea surface. They showed excellent correlation between integrated turbulent dissipation and estimated wave-breaking dissipation for wave ages below approximately $c_m/u_* = 50$.

A different statistic, which is often used to estimate breaking dissipation, is the breaker crest distribution, $\Lambda(c)$. This variable was introduced in Phillips (1985), based on laboratory work from Duncan (1981), showing a proportionality between the rate of energy loss from a breaking wave and its phase speed to the fifth power. In this formulation, the total breaking dissipation becomes

$$S_{ds} = \rho_w g^{-1} \int b c^5 \Lambda(c) dc, \tag{3.10}$$

where $\Lambda(c)$ is the total length of breaking crests per unit area, c is the breaker speed, and b is a scaling factor sometimes called the "breaking strength." $\Lambda(c)$ is a more complete description of the kinematics of the breaking waves than whitecap coverage. However, the use of $\Lambda(c)$ in practice (i.e. in Equation 3.10) has shown varying degrees of success. In particular, it is strongly suspected that b is not a constant. For example, the laboratory experiments of Drazen et al. (2008) demonstrated that b increases with the wave steepness, while Schwendeman et al. (2014) showed orders of magnitude variations in b in both their data and the published literature. Meanwhile, Banner et al. (2014b) highlighted the large impacts of differing interpretations of the breaking speed, c.

Conversely, Sutherland and Melville (2013) showed estimates of wave dissipation from $\Lambda(c)$ that were well-matched with modeled dissipation values. However, the method of Sutherland and Melville (2013) differs from the majority of previous studies in two important ways. First is in the use infrared cameras, leading to measurements of micro-scale breaking

waves, or "microbreakers," which are not visible as whitecaps. Sutherland and Melville (2015) noted that anywhere between 20% and 90% of their total estimated dissipation may have come from microbreaking. Additionally, they employed a spectral breaking strength, $b(c)$, introduced in Romero et al. (2012), which uses the spectral saturation (Equation 3.6) to approximate the dependence on wave slope identified in Drazen et al. (2008).

In this chapter, the focus is on the relationship of whitecap coverage to measurements of wind, waves, and turbulent dissipation. We choose to avoid $\Lambda(c)$ for several reasons. First, the results of Sutherland and Melville (2013) and Schwendeman et al. (2014) strongly indicate that estimating S_{ds} from $\Lambda(c)$ is not feasible without measurements of microbreaking, especially in mature wind seas. Furthermore, although $\Lambda(c)$ has the potential to provide more information on the whitecap kinematics, Kleiss and Melville (2011), Schwendeman et al. (2014), and Banner et al. (2014b) have shown that it can be very sensitive to changes in processing. Moreover, apart from the total magnitude, Kleiss and Melville (2010) showed very little variation in their measured $\Lambda(c)$ from whitecapping. Despite (or perhaps due to) its simplicity, whitecap coverage remains a useful representation of the overall breaking conditions. As such, W is frequently used in parameterizations of gas transfer (Woolf, 2005) and sea spray aerosol production flux (de Leeuw et al., 2011). The layout of this chapter is as follows: the data collection and processing is described in Section 3.2; the results are shown and discussed in Sections 3.3 and 3.4; and Section 3.5 summarizes the important points.

3.2 Methods

3.2.1 Field Experiments

The data used here come from two roughly three-week cruises in the North Pacific. The first cruise, onboard the R/V *New Horizon*, departed San Diego CA on 26 September 2012 and returned on 16 October 2012. The second, onboard the R/V *Thomas G. Thompson*, departed Seattle WA on 27 December 2014 and returned on 14 January 2015. The primary objective of both cruises was the replacement of a long-term moored wave buoy (Datawell

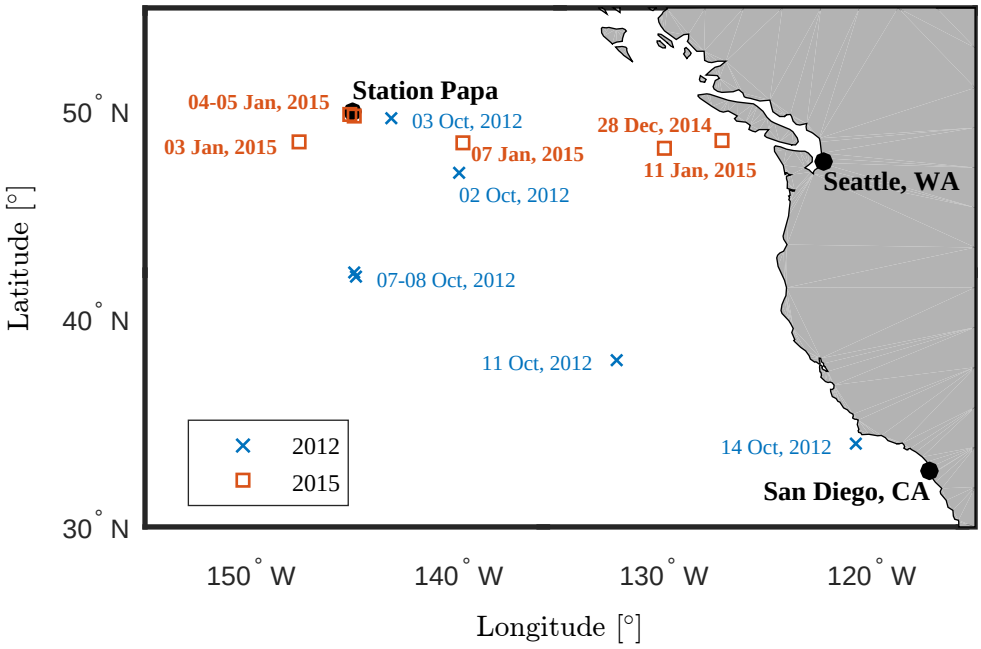

Figure 3.1: Map showing average ship locations during observations of both 2012 (blue crosses) and 2015 (orange squares) cruises.

Waverider MK III) at Ocean Station Papa (50° N, 145° W). Measurements from this buoy can be found in Thomson et al. (2013) and (Thomson et al., 2016). The remaining cruise time was left for further data collection. Figure 3.1 maps the ships' average location and proximity to Station Papa during days of successful data collection. Drifting instruments were used in both experiments, often deployed from the ship at dawn and retrieved later the same day. The most common combination of drifters was one Waverider buoy (Datawell DWR-G4) supplemented by two SWIFT buoys. Concurrent with the drifter deployments, wind and video measurements were made from the ship. During measurement operations, the ship was directed into the oncoming wind to limit distortion of the wind and waves.

Figure 3.2 shows histograms of the wind, waves, and dissipation measured during both experiments, averaged over 30-minute intervals coinciding with the video data (see below). The amount of data is roughly equal between the two cruises. U_{10} ranges from 5.5 m/s to 16.0 m/s, and H_s from 1.5 m and 5.8 m. Overall, the 2015 experiment resulted in more measurements of high winds, large and long waves, and high dissipation rates than 2012. Further details of the measurements are provided below.

3.2.2 In Situ Methods

Wind speed and direction were measured at 10 Hz using a tri-axis R. M. Young 8100 Sonic Anemometer mounted on the ships' jack staff. The anemometer height above sea level was 11.8 meters in 2012, and 15.7 meters in 2015. After despiking, the mean speed and direction are calculated over five-minute bursts. The wind friction velocity, u_*, is estimated using the inertial dissipation method (Edson et al., 1991; Yelland et al., 1994). Wind speed is corrected to the 10-meter estimate, U_{10}, using a standard turbulent boundary layer assumption with roughness z_0 given by the Charnock relation with constant Charnock parameter, $c_h = 0.014$ (Garratt, 1977).

Wave spectral measurements come from the Datawell DWR-G4 waveriders, which use GPS to measure the horizontal (east-west and north-south) and vertical wave orbital velocities. Datawell's built-in processing techniques are applied to the velocity measurements to calculate the frequency spectrum, $E(f)$, mean wave direction, $\overline{\theta}(f)$ and directional spread, $\Delta\theta(f)$ (de Vries, 2014). These were used to calculate the bulk parameters (H_s, f_m, etc) described in Section 3.1 and shown in Figure 3.2 .

Figure 3.3a shows the frequency spectra measured during the experiments, as well as the fourth and fifth moments of the spectra, and directional spread, all colored by U_{10}. After normalizing by the mean frequency, f_m, several frequency regimes are apparent. At low frequencies below f_m there is often significant swell energy, with some swell peaks on the order of the dominant wave energy. There is little relationship between the swell energy and the wind speed, as these waves were not generated by the local winds. The absolute peak

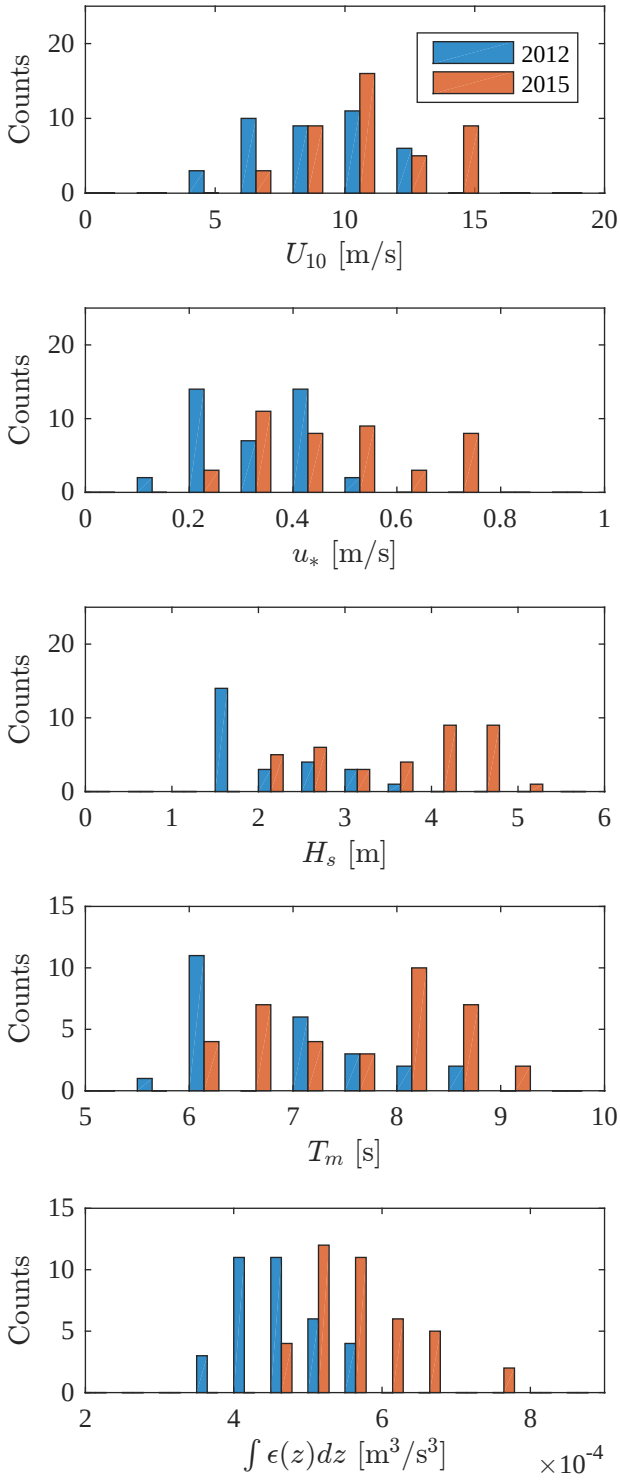

Figure 3.2: Histograms of wind, wave, and integrated turbulent dissipation measurements during both 2012 (blue) and 2015 (orange) experiments.

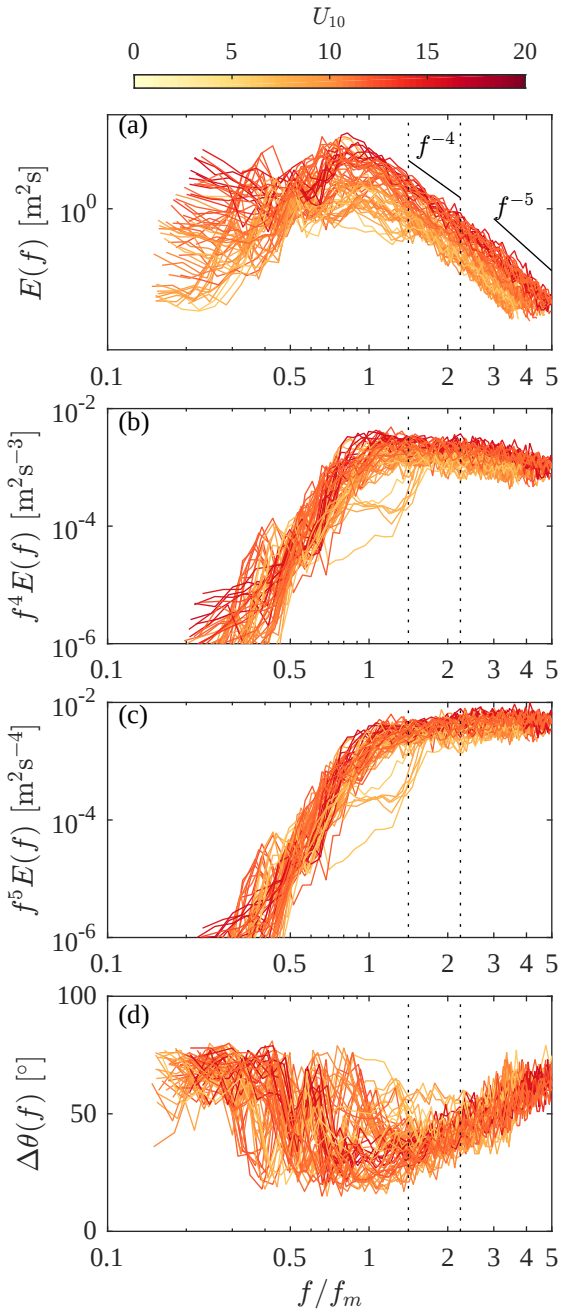

Figure 3.3: Measured wave spectra (a), plus their fourth (b) and fifth (c) moments, and directional spread (d), all colored by U_{10} and plotted against normalized frequency, f/f_m. Dotted lines mark the limits of the clearest f^{-4} decay, $\sqrt{2}f_m \leq f \leq \sqrt{5}f_m$. At higher frequencies, the decay is more consistent with saturation, f^{-5}.

in $E(f)$ often occurs in the vicinity of $f_m = 1$, but they do not match exactly. Above f_m, the spectra initially decay as f^{-4}, consistent with the equilibrium range theory of Phillips (1985). According to Phillips' theory, in this regime the spectral source terms of wind input, dissipation, and nonlinear energy flux are all in equilibrium, and the total energy is proportional to the local wind stress. Beyond these frequencies there is a transition to an f^{-5} tail, as has been observed in several previous measurements (e.g. Kahma and Calkoen, 1992; Romero and Melville, 2010) and which is often called the saturation range. This transition is more clearly visible in the fourth and fifth moments of the spectra. Based on the spectra, we define the equilibrium range to extend from roughly $\sqrt{2}f_m$ to $\sqrt{5}f_m$ ($2k_m$ to $5k_m$), as shown in dotted lines on Figure 3.3.

The fundamental principles of the SWIFT platform are detailed in Thomson (2012). The SWIFTs are equipped with a Nortek Aquadopp HR current profiler, which measures water velocities from a depth of 0.6 meters up to the free surface. The SWIFTs follow the wave orbital motion at the surface, effectively filtering the orbital velocity from their measurement. What remains are only the turbulent velocity fluctuations. The second-order structure function is calculated from the time series of velocity profiles at five-minute intervals. Using the method of Wiles et al. (2006), based on Kolmogorov's theory, leads to profiles of the turbulent dissipation rate. Throughout this paper, a bulk turbulent dissipation rate is used from integrating the profiles in depth, as in Equation 3.9. The turbulence profiles themselves are analyzed in further detail in a separate paper using the 2015 data (Thomson et al., 2016).

3.2.3 Video Methods

The camera configuration differed slightly between the two experiments. In 2012, a single serial "bullet" camera with a wide field-of-view (FOV) was mounted on a Pan/Tilt system to the foreword rail of the second deck of the R/V *New Horizon*, at a 10.8 meter height, similar to the setup of Schwendeman et al. (2014). The Pan/Tilt provided active stabilization and the capability to look either starboard or port, depending on lighting conditions. In 2015,

the bullet camera was replaced with several Pt. Grey Flea2 and Flea2G cameras, which were mounted directly to the ship's port and starboard rails, 11.0 meters above the waterline. One camera on each side had a FOV similar to the bullet camera. To test the effect of better resolution, another camera on each side was fitted with a narrower lens. Video was recorded synchronously from both cameras, and the side was again chosen based on the lighting. Table 3.1 summarizes the camera configuration and specifications from both experiments. Camera settings such as exposure time and gain were adjusted before every video capture to maximize contrast and minimize saturation.

Table 3.1: Camera specifications and geometry.

Year	Camera	Focal Length	Height	Pixels	Rectified Resolution
2012	Mini Bullet, Sony ExView	3.6 mm	10.8 m	720×480	1.2×10^{-2} m^2
2015	Pt. Grey Flea2G	2.8 mm	11.0 m	1288×964	1.2×10^{-2} m^2
2015	Pt. Grey Flea2	9 mm	11.0 m	1032×776	1.5×10^{-3} m^2

Figure 3.4 shows the steps involved in the video processing. First, the resulting video data is georectified from pixel coordinates to meters. Schwendeman and Thomson (2015a) showed that, in the absence of other data sources, adequate georectification can be performed using an automatic detection of the horizon. This is the method used on the 2012 video data. In 2015, a NovAtel SPAN-IGM-A1 receiver and dual antennas were mounted on the rail next to the port side cameras to aid in the georectification. NovAtel's SPAN products combine an inertial navigation system (INS) with global navigation satellite system (GNSS) for a more robust and accurate position measurement than can be achieved with either method alone. The horizon method is still used, as a means to synchronize the camera frames and INS-GNSS data stream. The rectified images are interpolated onto a rectangular grid for further processing. In each case, the grid was set between 40 and 60 meters from the ship, to avoid reflections from the ship while maintaining acceptable camera resolution. The pixel

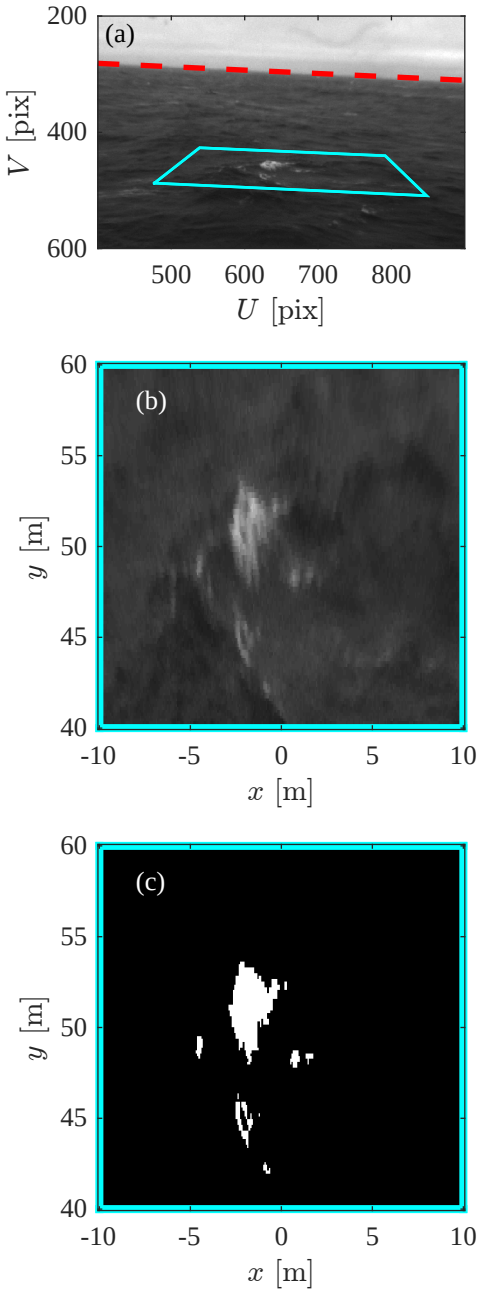

Figure 3.4: Example of rectification and thresholding for a single video frame. (a) The original frame, undistorted and cropped, showing the sample area (cyan) and detected horizon (red dashed line). (b) The sample area, rectified to world coordinates. (c) The area after thresholding.

footprint in the rectified image is specific to the camera geometry, the details of which can be found in Table 3.1.

Next, a brightness threshold is applied to the rectified video to isolate the whitecaps. A method similar to that of Kleiss and Melville (2011) and Schwendeman et al. (2014) works well for the large quantity of video used here. In this technique, a histogram of pixel brightness is calculated over 5-minute lengths of video. The second derivative of the logarithm of the histogram yields a peaked shape, indicating a change of curvature separating the bright foam of the whitecaps from the otherwise dark sea surface. The threshold is set as the brightness at 20% of the peak in the curvature, as recommended in Kleiss and Melville (2011).

Finally, the 5-minute thresholded bursts are gathered into half-hour segments for calculation of whitecap coverage, W. Averaging over 30 minutes reduces the scatter in the W estimate, and matches the duration of the Waverider measurements. Since video was recorded at 15 frames-per-second (fps) in the 2012 experiment, and 5 or 7.5 fps in 2015, this amounts to between 9000 and 27000 images per 30 minutes. This is well above the 500 images which Callaghan and White (2009) recommended to reduce the variability of W to $\pm 3\%$. Still, uncertainty exists due to non-stationarity of the whitecapping and lighting conditions, as well as in the choice of threshold. Variability in the 5-minute bursts is used to make error estimates in the 30-minute averages. A bootstrapping of the bursts is performed, and error bars are calculated corresponding to one standard deviation around the mean. Some errors were particularly large, on the order of W, and were found to correlate with poor thresholding or low data quality in one or more of the bursts. Therefore, these points are removed from the subsequent analysis.

The two cameras from the 2015 experiment are used to determine the effect of the pixel resolution on whitecap coverage. Schwendeman et al. (2014) postulated that their data was biased by inadequate resolution of small whitecaps. The narrow FOV camera improved upon the previous resolution by roughly a factor of 10 (Table 3.1), but Figure 3.5 shows little difference in W from the larger FOV. Therefore, to avoid double-counting the 2015

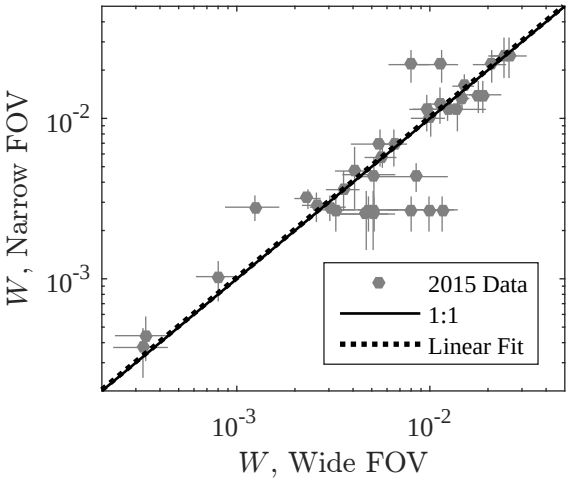

Figure 3.5: Comparison of whitecap coverage, W, for video from wide field-of-view and narrow field-of-view cameras in the 2015 experiment. The linear fit is barely visible next to the one-to-one line.

data in curve-fitting, only the wide FOV results are used in the remainder of the paper.

Figure 3.5 indicates that the limiting factor for identifying small breaking events may not be camera resolution. This is encouraging for comparisons of W measurements across studies, given that there has been little attempt to standardize equipment and image acquisition. However, there is another factor which may preclude measurement of small whitecaps, namely, lack of contrast due to less production of bubbles and foam. Visual inspection of our images indicates that the quantification of these small events is highly dependent on proper illumination and optimal camera settings (exposure, shutter speed, etc.). Glare, sun glitter, and low light at dawn and dusk can all impede the detection of small breakers. In the limiting case of microbreaking, no foam is produced, meaning that these events cannot be measured from traditional video cameras regardless of camera settings and lighting.

3.3 Results

3.3.1 W vs. U_{10} and u_*

As discussed in Section 3.1, the most common parameterization of whitecap coverage is to U_{10}. Figure 3.6a shows the North Pacific data along with three fits from the recent literature, plus the widely used relation of Monahan and O'Muircheartaigh (1980). The three more recent studies were chosen because their experimental methods closely match those used here. In each of these studies, whitecap coverage was calculated using digital images from a camera set 10-20 m above sea level with an oblique view 6-33° below horizontal, and with a pixel-wise brightness threshold. Stramska and Petelski (2003) and Callaghan et al. (2008a) both used shipboard photographs from the North Atlantic Ocean, while the video in Sugihara et al. (2007) came from a tower in Tanabe Bay, Japan, roughly 2 km offshore. In all cases, the local winds were measured *in situ* and adjusted to U_{10}, without a correction for atmospheric stability. Each fit line is plotted for only the range of the available measurements, with maximum U_{10} of 14 m/s (Stramska and Petelski, 2003), 16.3 (Sugihara et al., 2007), and 23.1 (Callaghan et al., 2008a). All of these fits are of the cubic variety (Equation 3.2), although Callaghan et al. (2008a) found that their data was best described by two distinct cubics, with a transition between 9.25 and 11.25 m/s. The literature curves tend to diverge for $U_{10} < 7$ m/s, when whitecapping is infrequent and microbreaking may have a larger impact. In the range of $7 < U_{10} < 14$ m/s, the fits agree to within roughly a factor of 2. This wind speed range also brackets the majority of the North Pacific data.

The W data used in Monahan and O'Muircheartaigh (1980) were calculated manually, using the method described in Monahan (1969). This may explain why the classical Monahan and O'Muircheartaigh (1980) fit is biased high relative to the other curves, which were made using thresholded digital images. In addition, the Monahan and O'Muircheartaigh (1980) fit is in the form of a power law (Equation 3.1), which diverges from the cubic fits at low wind speeds.

A fit to the North Pacific data is also plotted in Figure 3.6a, and closely resembles those

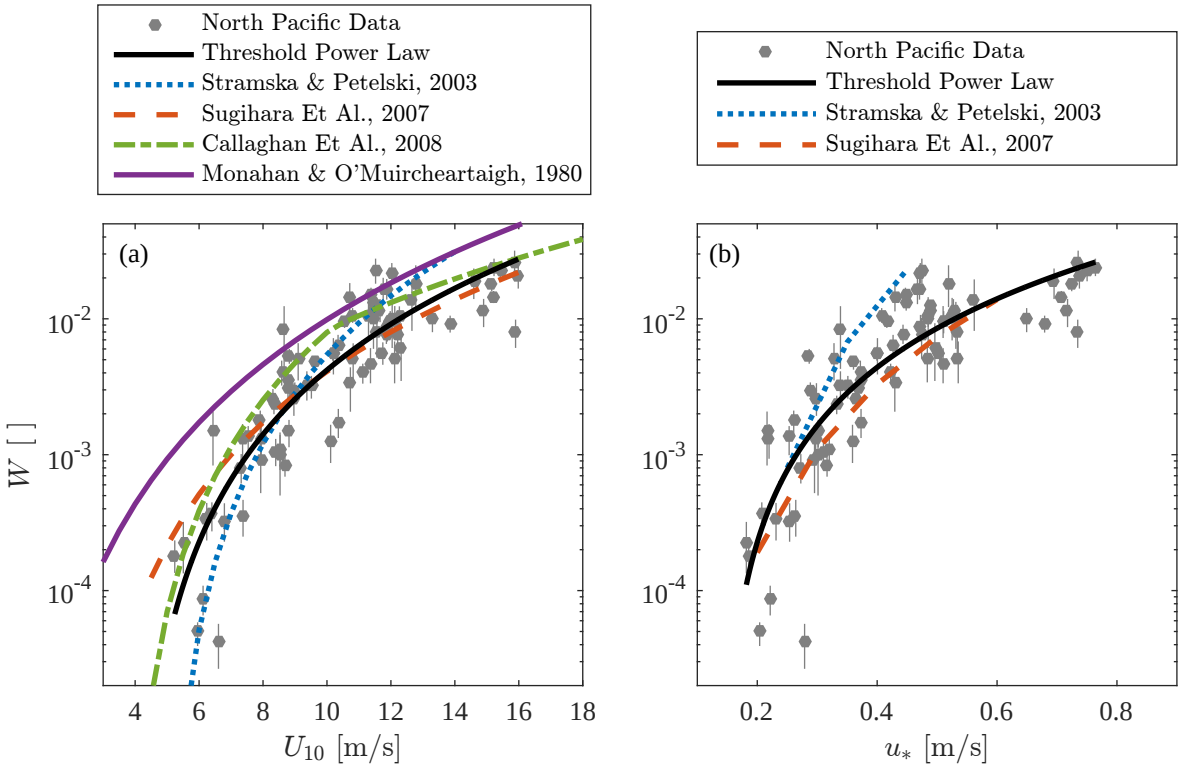

Figure 3.6: Whitecap coverage vs. (a) U_{10} and (b) u_*, as well as the threshold power law fit for each (black solid line). Included are relations from Stramska and Petelski (2003) (blue dotted), Sugihara et al. (2007) (red dashed), Callaghan et al. (2008a) (green dash-dot), and Monahan and O'Muircheartaigh (1980) (purple solid) plotted over the range of conditions from which they were calculated.

of the recent literature. A hybrid of Equations 3.1 and 3.2 is used,

$$W = a(x - b)^n, \tag{3.11}$$

were x is the explanatory variable, in this case U_{10}. This style of fit is used throughout the remainder of this paper, and will be called the "threshold power law." It incorporates the threshold behavior which is a common feature of whitecap parameterizations (e.g. Banner et al., 2000), as well as the ability to tune the exponent, n. The threshold power law is more versatile than either Equations 3.1 or 3.2, however, the coefficients of this function cannot be solved for linearly. Instead, the Levenberg-Marquardt algorithm is used to compute the best fit by minimizing the sum of the squares of the log residuals,

$$W_{res} = \log_{10} W - \log_{10} \left[a(x - b)^n\right]. \tag{3.12}$$

The log residuals are used to give equal weight to the whitecap data across several orders of magnitude. Table 3.2 shows the best fit values of a, b, and n from Equation 3.11. In addition, 90% confidence intervals are estimated for each coefficient, again using a bootstrap-style technique. The full dataset is randomly resampled (with replacement) 100 times, with a best fit calculated after each resampling. The confidence intervals on each coefficient correspond to the 5th lowest and 95th highest value in the set of all fits. It should be noted that because the threshold power law has three coefficients, these confidence intervals are sometimes quite large, particularly when the variables are highly scattered. In the case of U_{10}, the cubic equation likely would have been adequate, as $n = 2.8$ is the exponent of the best fit, and $n = 3$ is within the confidence interval ($1.94 \leq n \leq 3.39$).

Table 3.3 lists the error metrics for each fit, which are also calculated from the log residuals. The root mean square error (RMSE) is defined as

$$RMSE = \sqrt{\frac{\sum W_{res}^2}{N}}, \tag{3.13}$$

where N is the number of observations. This RMSE can be thought of as an average order of magnitude deviation from the fit. The other quantity shown is the coefficient of

Table 3.2: Results of the threshold power law fit, $W = a(x-b)^n$, with 90% confidence intervals in parenthesis.

Fit Variable, x	a	b	n
$\mathbf{U_{10}}$	$\mathbf{2.81 \times 10^{-5}}$	$\mathbf{3.87 \times 10^{0}}$	**2.76**
(Interval)	$(4.88 \times 10^{-6}, 2.19 \times 10^{-4})$	$(2.77 \times 10^{0}, 5.21 \times 10^{0})$	(1.94, 3.39)
$\mathbf{u_*}$	$\mathbf{6.82 \times 10^{-2}}$	$\mathbf{1.39 \times 10^{-1}}$	**2.04**
(Interval)	$(5.08 \times 10^{-2}, 1.03 \times 10^{-1})$	$(9.49 \times 10^{-2}, 1.67 \times 10^{-1})$	(1.63, 2.56)
$\mathbf{U_{10}/c_m}$	$\mathbf{2.71 \times 10^{-2}}$	$\mathbf{3.85 \times 10^{-1}}$	**2.66**
(Interval)	$(1.48 \times 10^{-3}, 3.31 \times 10^{-2})$	$(-2.19 \times 10^{-1}, 5.41 \times 10^{-1})$	(1.55, 5.32)
$\mathbf{u_*/c_m}$	$\mathbf{9.64 \times 10^{0}}$	$\mathbf{1.69 \times 10^{-2}}$	**1.92**
(Interval)	$(9.54 \times 10^{-1}, 6.24 \times 10^{1})$	$(1.34 \times 10^{-2}, 2.00 \times 10^{-2})$	(1.25, 2.50)
$\mathbf{u_*/c_p}$	$\mathbf{4.80 \times 10^{-1}}$	$\mathbf{1.14 \times 10^{-2}}$	**1.09**
(Interval)	$(1.02 \times 10^{-1}, 6.89 \times 10^{3})$	$(-6.49 \times 10^{-2}, 1.32 \times 10^{-2})$	(0.67, 5.36)
$\mathbf{H_s k_p/2}$	$\mathbf{5.43 \times 10^{3}}$	$\mathbf{-3.33 \times 10^{-2}}$	**4.48**
(Interval)	$(4.16 \times 10^{-2}, 3.09 \times 10^{6})$	$(-3.76 \times 10^{-1}, 2.51 \times 10^{-3})$	(0.43, 9.99)
$\mathbf{H_s k_m/2}$	$\mathbf{6.85 \times 10^{2}}$	$\mathbf{5.78 \times 10^{-3}}$	**2.66**
(Interval)	$(3.09 \times 10^{0}, 5.00 \times 10^{5})$	$(-1.79 \times 10^{-3}, 9.10 \times 10^{-3})$	(1.40, 4.47)
$\mathbf{H_m k_m/2}$	$\mathbf{8.26 \times 10^{1}}$	$\mathbf{1.28 \times 10^{-3}}$	**2.19**
(Interval)	$(1.47 \times 10^{-1}, 5.72 \times 10^{3})$	$(-6.54 \times 10^{-4}, 5.78 \times 10^{-3})$	(0.70, 3.27)
$\mathbf{H_p k_p/2}$	$\mathbf{1.47 \times 10^{5}}$	$\mathbf{-6.81 \times 10^{-2}}$	**6.71**
(Interval)	$(1.60 \times 10^{2}, 3.35 \times 10^{5})$	$(-3.65 \times 10^{-1}, -1.68 \times 10^{-2})$	(2.81, 17.42)
mss	$\mathbf{7.63 \times 10^{7}}$	$\mathbf{3.26 \times 10^{-4}}$	**4.01**
(Interval)	$(2.61 \times 10^{7}, 1.05 \times 10^{8})$	$(-2.05 \times 10^{-4}, 5.10 \times 10^{-4})$	(3.88, 4.09)
$\mathbf{mss/(\Delta\theta)}$	$\mathbf{1.46 \times 10^{5}}$	$\mathbf{9.36 \times 10^{-4}}$	**3.07**
(Interval)	$(2.94 \times 10^{0}, 1.02 \times 10^{7})$	$(4.66 \times 10^{-4}, 2.52 \times 10^{-3})$	(1.03, 3.87)
$\mathbf{mss/(\Delta f \Delta\theta)}$	$\mathbf{2.82 \times 10^{1}}$	$\mathbf{1.44 \times 10^{-2}}$	**2.39**
(Interval)	$(1.90 \times 10^{0}, 1.05 \times 10^{2})$	$(1.26 \times 10^{-2}, 2.12 \times 10^{-2})$	(1.45, 2.81)
$\mathbf{\int \epsilon(z) dz}$	$\mathbf{1.73 \times 10^{4}}$	$\mathbf{1.97 \times 10^{-4}}$	**1.89**
(Interval)	$(1.30 \times 10^{3}, 6.02 \times 10^{7})$	$(1.40 \times 10^{-4}, 3.11 \times 10^{-4})$	(1.47, 2.92)
$\mathbf{\int \epsilon(z) dz \ \ (n = 1)}$	$\mathbf{2.80 \times 10^{1}}$	$\mathbf{3.46 \times 10^{-4}}$	**1**
(Interval)	$(2.20 \times 10^{1}, 3.52 \times 10^{1})$	$(3.26 \times 10^{-4}, 3.76 \times 10^{-4})$	

determination (R^2), here defined as,

$$R^2 = 1 - \frac{\sum W_{res}^2}{\sum \left(\log_{10} W - \overline{\log_{10} W}\right)^2}, \tag{3.14}$$

where the overbar implies an average. As will be discussed further, the fit to U_{10} has the best statistics (RMSE=0.28 , R^2=0.81) of any shown in this paper.

In Figure 3.6b, W is plotted against u_*, with a threshold power law fit and literature relations from Stramska and Petelski (2003) and Sugihara et al. (2007). u_* was not calculated in Callaghan et al. (2008a). The scatter is slightly more than for U_{10}, as indicated by the fit statistics (RMSE=0.32, R^2=0.74). In addition, the fit from Stramska and Petelski (2003) is qualitatively distinct from the others. This is probably explained by the fact that while u_* was estimated here and in Sugihara et al. (2007) using the inertial dissipation method, Stramska and Petelski (2003) use an empirical relation from U_{10}.

One feature that is apparent in this dataset is a leveling off of W at the highest winds, $U_{10} > 14$ m/s. In many ways this is similar to the results of Callaghan et al. (2008a), which also show a muted whitecapping response in the high wind speed regime. Unfortunately, these conditions are not frequently measured, so it is difficult to ascertain whether this is a persistent feature or a product of small sample size. For example, the data above 14 m/s shown here come from a single day (07-Jan, 2015). Similarly, Sugihara et al. (2007) show only two data points above 14 m/s and Stramska and Petelski (2003) do not make any measurements above 14 m/s.

Stramska and Petelski (2003), Sugihara et al. (2007), and Callaghan et al. (2008a) each identify wave development as a source of scatter in their $W(U_{10})$ plots. Stramska and Petelski (2003) separate their data using the difference between their (visually-estimated) H_s and the fully-developed significant wave height, H_{Full}, from the Pierson-Moskowitz spectrum (Pierson and Moskowitz, 1964). They find markedly less whitecapping when the waves are "undeveloped," defined as $H_s < (H_{Full} - 0.5$ m), in comparison with the "developed" waves in similar wind speeds. Sugihara et al. (2007) note a similar separation by wave age, c_p/u_*, but only in the case of pure windseas. For $8 < c_p/u_* < 16$, W is noticeably less than the

Table 3.3: Statistics of the threshold power law best fit.

Fit Variable, x	$RMSE$	R^2
U_{10}	0.28	0.81
u_*	0.32	0.74
U_{10}/c_m	0.34	0.69
u_*/c_m	0.30	0.76
u_*/c_p	0.43	0.49
$H_s k_p/2$	0.56	0.13
$H_s k_m/2$	0.44	0.48
$H_m k_m/2$	0.47	0.40
$H_p k_p/2$	0.57	0.10
mss	0.39	0.58
$mss/(\Delta\theta)$	0.38	0.61
$mss/(\Delta f \Delta\theta)$	0.30	0.75
$\int \epsilon(z)dz$	0.50	0.27
$\int \epsilon(z)dz \;\; (n=1)$	0.51	0.26

remainder of the data ($16 < c_p/u_* < 29$). Finally, Callaghan et al. (2008a) concentrate on the wind history, or wind acceleration, similar to Hanson and Phillips (1999). They show that when the wind is increasing (as measured over a 2.5 hour period) and U_{10} is above 9 m/s, W is significantly reduced. To summarize, each study found that when the waves were growing or highly forced, the whitecap coverage was less than otherwise expected.

These ideas are tested using the residuals of the U_{10} threshold power law fit. Figure 3.7a shows the W_{res} data plotted against c_m/u_*. A linear fit of the residuals is also shown to highlight the trend. Interestingly, over the whole dataset there is a decreasing trend with wave age (W reduced in older waves). However, for $c_m/u_* < 29$, as in the Sugihara et al. (2007) dataset, W_{res} strongly increases with wave age. In other words, W is less than predicted in both particularly young and particularly old waves. This is similar to the results of Lafon et al. (2007) in a coastal region, showing a peak in W at around $c_p/U_{10} = 0.69$. A fit of W to (inverse) wave age alone was also attempted, however, the overall statistics are not significantly improved (see Table 3.3) and no peak is apparent. Of the wave age variables, the best fit is to u_*/c_m, rather than c_p or U_{10}.

Next, the residuals are examined as a function of the 2.5-hour average wind acceleration, $\Delta U_{10}/\Delta t$, as in Callaghan et al. (2008a) (Figure 3.7b). The linear fit is plotted for all the residuals, as well as for only $U_{10} > 9$ m/s. As predicted, the residuals are negative (W reduced) for accelerating winds, and the effect is more pronounced in the higher wind regime. Even for the higher winds, however, the trend is small in comparison with the overall scatter. Finally, the residuals are plotted against the Stramska and Petelski (2003) wave development metric, $H_{Full} - H_s$. For this variable almost no trend can be seen. This is likely due to the influence of swell on H_s. Indeed there are many points for which $H_s > H_{Full}$, which could not occur in the absence of swell energy.

3.3.2 W vs. Wave Slope

Figure 3.7 shows that wave development can modulate the general relationship of W to U_{10}. Next we test how well the whitecap coverage can be predicted from measurements of the

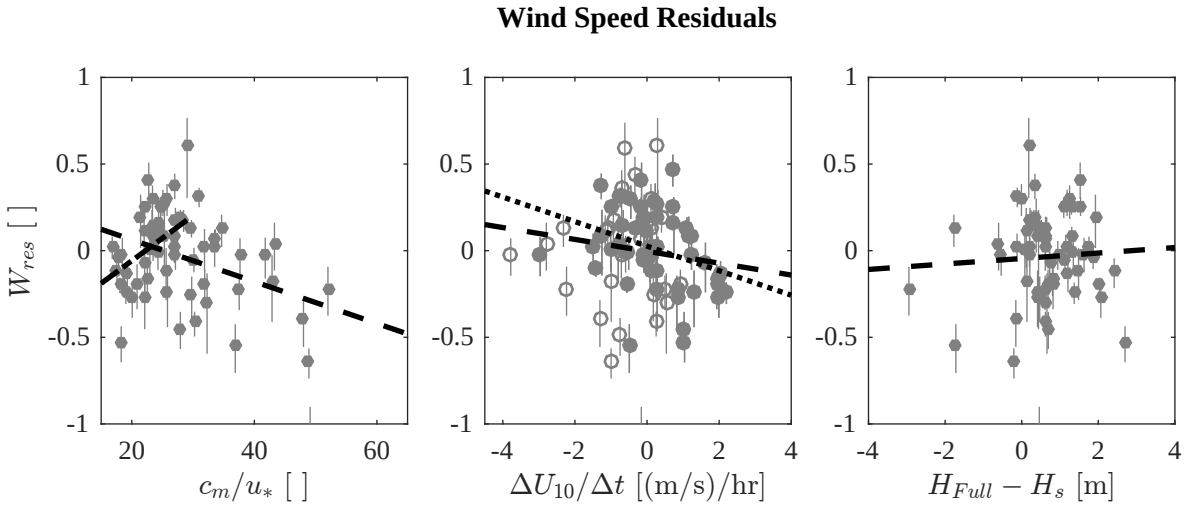

Figure 3.7: Residuals of the U_{10} fit, plotted against (a) wave age, (b) wind acceleration, and (c) wave height difference from fully-developed. Dashed lines show linear fits to all the residuals. The dash-dot line in (a) is for only $c_m/u_* < 29$. The dotted line in (b) is for $U_{10} > 9$ m/s ($U_{10} < 9$ m/s data are shown with open circles).

waves alone. As discussed in Section 3.1, an increase in the overall wave steepness is expected to lead to more whitecaps. In Figure 3.8a, W is plotted against wave steepness using the significant wave height, H_s, and the mean wavenumber, k_m. There is a clear correlation, but several points look to be extreme outliers. In particular, the points in the lower right of the plot, with relatively large steepness but little whitecapping. These are likely points with a significant fraction of swell energy, leading to an unsuitable significant wave height. Again, a threshold power law fit is used to quantify the correlation, as shown in Tables 3.2 and 3.3. In addition, the results using several alternative steepnesses of the form $Hk/2$ are also reported. Despite the issues visible in Figure 3.8a, $H_s k_m/2$ was found to have the best statistics of these fits (RMSE=0.44, R^2=0.48). The fits using peak variables H_p or k_p are particularly poor for this data. This is important to note, because while breaking parameterizations that have been developed in young wind seas often use these variables (e.g. Hwang and Sletten, 2008; Kleiss and Melville, 2010), in the open ocean the peak waves may not be related to

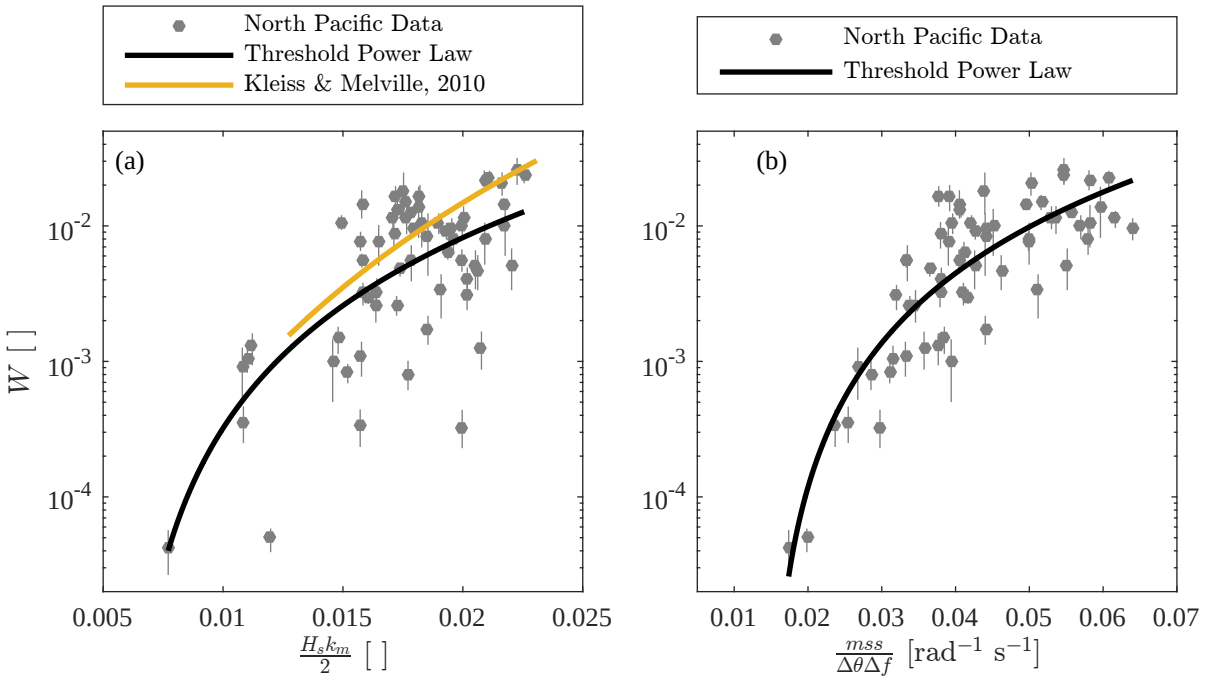

Figure 3.8: Whitecap coverage vs. (a) $H_s k_m/2$ and (b) equilibrium range mss, using the frequencies $\sqrt{2}f_m \leq f \leq \sqrt{5}f_m$, and normalized by the mean directional spread, $\Delta\theta$, and frequency bandwidth, Δf. Black lines are the current fits, and the orange line comes from Kleiss and Melville (2010), using $H_p k_p$.

the breaking waves at all. The fit from Kleiss and Melville (2010) to $H_p k_p/2$ is shown for comparison in Figure 3.8a. Aside from the scatter, the overall behavior is quite similar over the range of their measurements. Note that Kleiss and Melville (2010) use a standard power law fit, which is acceptable since their steepnesses are all relatively large. However, the North Pacific whitecaps show a clear threshold around $H_s k_m/2 \approx 0.01$, which the power law could not reproduce.

Better agreement is found using steepness parameters that focus on the short or intermediate wind waves. In particular, the mss of the equilibrium range waves shows good correlation (RMSE=0.39, R^2=0.58). Again, the definition of the equilibrium range used here is $\sqrt{2} \leq f/f_m \leq \sqrt{5}$, as shown in Figure 3.3. Extending the mean square slope calculation to

higher frequencies in the saturation range tends to degrade the correlation. This may have to do with the scale of waves that form whitecaps. The corresponding equilibrium range phase speeds are 0.44 to 0.71 times c_m. Although the peak in estimates of $\Lambda(c)$ from whitecaps tends to be in the $0.2c_m$ to $0.5c_m$ range, these equilibrium range waves are well-represented in the overall whitecapping. Moreover the results of Gemmrich et al. (2013) indicate that after weighting by c^5, the equilibrium waves produce the majority of the whitecap energy dissipation. This gives a physical reasoning as to why the slopes of these particular waves best explain the whitecap coverage.

In Figure 3.8b, W is plotted against mss after further normalizing by directional spread, $\Delta\theta$, and frequency bandwidth, Δf. The resulting fit nearly matches the performance of the wind variables (RMSE=0.30, R^2=0.75). The success of the normalization shows that, for similar mss, wavefields that are more unidirectional will exhibit more breaking. Note that Figure 3.3 shows significant variation in the directional spread with frequency. For consistency with mss, the value used in the normalization is the mean value over the equilibrium range frequencies. The mss normalized by $\Delta\theta$ is similar to the "weighted, band-averaged saturation" used in Gemmrich (2010) and Gemmrich et al. (2013),

$$\sigma_b = \int_{f_p}^{4f_p} \frac{B(f)}{f\Delta\theta(f)} df, \tag{3.15}$$

where $\Delta\theta(f)$ is the frequency-dependent directional spread and the factor of $1/f$ relates the saturation, $B(f)$, to mss (as in Eq. 3.7). In addition, normalizing by frequency bandwidth, $\Delta f = (\sqrt{5} - \sqrt{2})f_m$, also improves the quality of the fit. Since $f^{-1}B(f) \propto f^4E(f)$ is approximately constant in the equilibrium range, this normalization removes the erroneous dependence on f_m from the limits of integration.

Compared to Figure 3.6, the plots of W with wave steepness variables show less evidence of leveling off at the high winds (steep waves). Thus the unexpectedly low W for these wind conditions is perhaps explained by the wave slope, which is also lower than expected. This effect is also shown and discussed in Thomson et al. (2016). Although the overall fit to mss is not quite as good as that of U_{10}, it may be that young, highly-forced waves are a case

where wave slope parameters outperform the wind variables.

3.3.3 W vs. Turbulent Dissipation Rate

Finally, the whitecap coverage is compared with the turbulent dissipation rate, as measured by the SWIFT drifters. Again, the SWIFTs measure profiles of dissipation, $\epsilon(z)$, but since we are only interested in total dissipation, we integrate the profiles to a single value, $\int \epsilon(z)dz$. This bulk turbulent dissipation rate is in good agreement with the wave dissipation rate in many conditions (see Thomson et al., 2013; Schwendeman et al., 2014). Figure 3.9a shows W plotted against $\int \epsilon(z)dz$. It is clear that the scatter is much larger than both the wind speed and wave steepness parameterizations. This is reflected in the statistics of the threshold power law fit to the dissipation data (RMSE=0.50, R^2=0.27). In particular, for integrated dissipation rates below 5 $\mathrm{m^3 s^{-2}}$, the variability is more than two orders of magnitude. Although the confidence intervals on the best fit exponent ($1.47 \leq n \leq 2.92$) do not support the linear model proposed by Hwang and Sletten (2008), the statistics are not made significantly worse by constraining the fit to be linear (RMSE=0.51, R^2=0.26). In Figure 3.9b, the same results are plotted using a linear vertical axis for an alternative view of the data.

In Figure 3.10, the residuals of the fit to dissipation are examined, using c_m/u_* as in Figure 3.7a. This time the young waves ($c_m/u_* \leq 29$) show no clear pattern. However, for older waves there is an even stronger negative trend. The lowest residuals come from the periods when whitecap coverage is least, yet there is still significant turbulent dissipation. This could be evidence of the contribution of microbreaking to the dissipation. It is consistent with Sutherland and Melville (2015), who suggest that the percentage of dissipation from microbreaking increases with wave age, to as much as 90%.

Alternatively, uncertainty in the *in situ* measurements of turbulent dissipation may be responsible for both the overall scatter and the bias. There are three broad categories of uncertainties here. First are uncertainties from sources of turbulent dissipation not related to wave breaking. These could be due to direct input from the wind, non-breaking "swell

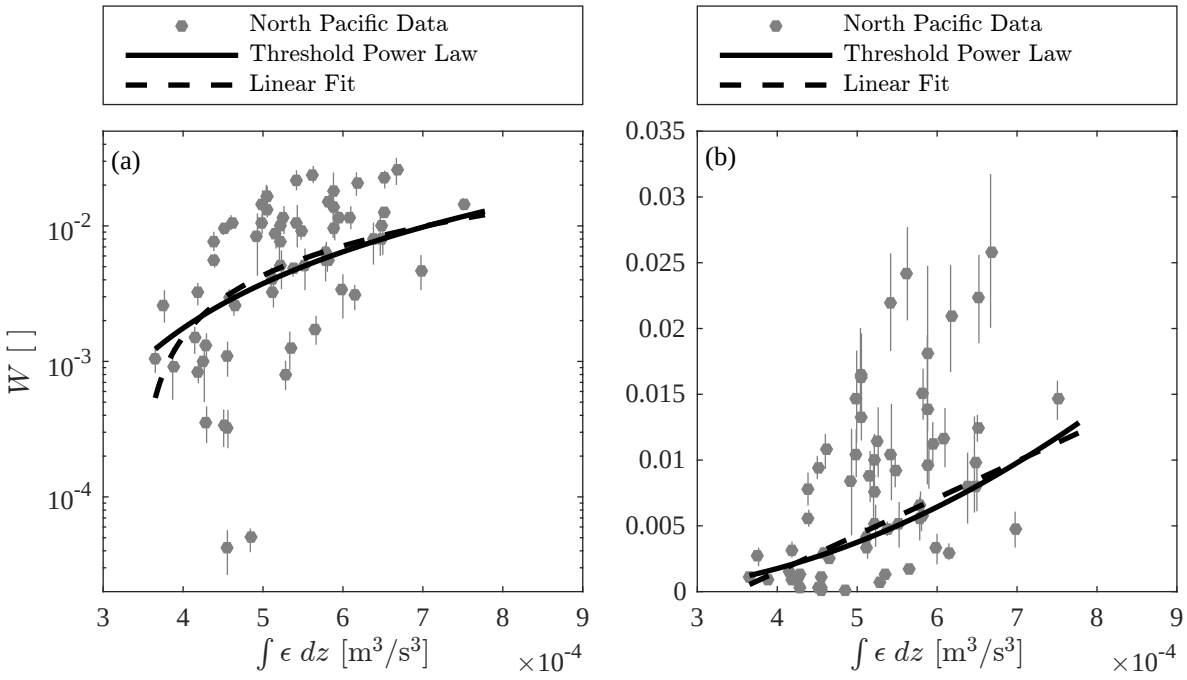

Figure 3.9: Whitecap coverage vs. integrated turbulent dissipation rate, shown on (a) logarithmic and (b) linear axis. Solid lines are the threshold power law fit, while dashed lines are a linear fit.

dissipation," or the SWIFTs' own turbulent wake. The first two have been estimated to be only minor contributions to the total turbulent dissipation (see Terray et al., 1996; Schwendeman et al., 2014), while the latter is minimized by using acoustic beams directed out and away from the SWIFT hull. Conversely, the turbulent dissipation is only one of several mechanisms for breaking-related dissipation. Most importantly, these measurements cannot quantify the dissipation due to the entrainment of air in the whitecap bubble plume, which Lamarre and Melville (1991) estimated to be as much as 50% of the dissipation in laboratory breakers. Finally, there are the uncertainties in the measurement of turbulent dissipation inherent to the SWIFT instrumentation and methodology. Thomson (2012) estimated these errors to be on the order of 10%, however, these estimates were made for much smaller wave heights ($H_s < 1$ m). More recently, Thomson et al. (2016) have demonstrated the difficulty

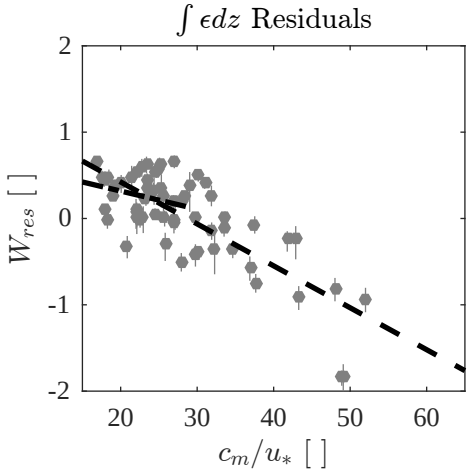

Figure 3.10: Residuals of the threshold power law fit to turbulent dissipation, plotted against wave age. The dashed line is a linear fit to all the residuals, and the dash-dot line is for only $c_m/u_* < 29$.

in measuring turbulent velocities in the bubble cloud produced by large breaking events. Therefore, it may be that some of the dissipation occurring during active whitecapping is not resolved in the SWIFT measurements.

3.4 Discussion

Figure 3.6a stands in stark contrast to Anguelova and Webster (2006), who suggest discrepancies of two orders of magnitude in the literature $W(U_{10})$ fits across all wind speeds. By comparing only studies using modern digital image processing and similar camera geometry, many of the main methodological sources of scatter are eliminated. There is a clear distinction from the widely-used fit of Monahan and O'Muircheartaigh (1980), which was derived from manual tracing of whitecaps in relatively small batches of photographs. The modern fits agree to within roughly a factor of two between wind speeds of 7 and 14 m/s. Large intermittence of whitecapping is likely responsible for the deviations at low wind speeds. Meanwhile at high winds, the relative lack of measurements leads to biases associated with

the small sample size. Still, despite all the known issues, the fit to U_{10} has the least error of all the variables examined here. This is similar to the conclusions of Kleiss and Melville (2010), Goddijn-Murphy et al. (2011), and Salisbury et al. (2013), who all show little to no improvement using parameterizations that incorporate the wave conditions.

Wave-breaking is related to the local wind speed through the concept of equilibrium. According to the Phillips (1985) theory, the spectral energy density of the equilibrium range waves is proportional to u_*. Since mss is calculated from the fourth moment of the wave frequency spectrum, and the equilibrium range spectrum decays as f^{-4}, the mss of the equilibrium waves is approximately proportional to u_*, as shown in Thomson et al. (2013). Thus, the success of the fit of W to equilibrium range mss is no coincidence. The Phillips theory also accounts for the directional spread of the waves through the $I(p)$ function, although this variable is more challenging to measure.

Thomson et al. (2013) also demonstrated that total wind input and total wave dissipation are often in near-equilibrium (i.e. not just in the spectral equilibrium range). This was also shown in Hwang and Sletten (2008), based on a scaling of fetch-limited wave growth. Their proposed dissipation scaling (Equation 3.8) was actually validated using the wind input, which is primarily dependent on u_*, with a small modulation by wave variables. To summarize: the U_{10} and u_* parameterizations are successful because they are variables that are closely linked to both the equilibrium wave steepness and wave-breaking dissipation, yet are measured more precisely than either steepness or dissipation themselves.

An unresolved question is whether to differentiate "active" whitecaps from "residual" foam, as is often done in the literature (e.g. Scanlon and Ward, 2013). It has been hypothesized that measurements of purely active breaking may be more closely related to wave dynamics, since the behavior of residual foam is dependent on water chemistry (Callaghan et al., 2008b). The experiments of Callaghan et al. (2013) show that whitecap foam can indeed be stabilized by high levels of surfactants. Meanwhile, satellite estimates of W indicate that U_{10} parameterizations are biased low when the sea surface temperature is high, perhaps because of increased water viscosity or other bubble dynamics (Salisbury et al., 2013). How-

ever, ongoing laboratory work has shown an approximately linear relationship between the volume of a whitecap's submerged bubble plume and its dissipation of wave energy (A. H. Callaghan, personal communication). A similar conclusion was presented in Lamarre and Melville (1991). The bubble plume volume is in turn correlated with the surface decay of the whitecap foam patch, although water chemistry (e.g. large surfactant concentrations) may modify this relationship. In this way, the appearance and decay of residual foam may actually be a more useful expression of the breaking energetics than previously thought.

As discussed in Scanlon and Ward (2013), it is difficult to separate active and residual breaking on the basis of pixel brightness alone. Instead, we use an implicit calculation to determine the influence of residual foam in W. This strategy is based on the observation that as a whitecap propagates through the camera field-of-view, it "flips" pixels from zero to one in the thresholded images (Figure 3.4c). For an idealized whitecap, these pixels remain "flipped" until the residual foam fully decays. In this case, only the newly flipped pixels are associated with active whitecapping, while the total whitecap coverage also incorporates residual foam. The ratio of these quantities, multiplied by the time between images, dt, produces a characteristic foam timescale,

$$\tau = \frac{\sum I_{total}}{\sum I_{flipped}} dt, \tag{3.16}$$

where dt is needed to account for differences in camera frame rate. It should be noted that, though related, this τ is not directly comparable to the average whitecap duration as calculated from $\Lambda(c)$ (as in Kleiss and Melville, 2010), or from tracking individual breakers (as in Callaghan, 2013). Rather, τ represents the average residence time of whitecap foam over an individual image pixel.

Unfortunately, visual inspection of the thresholded images shows that the actual whitecaps do not necessarily behave like the idealized whitecap described above. Instead, real whitecaps leave patchy foam which may be further advected by the subsequent wave orbitals. This means that pixels may flip several times over the course of a single breaking event. Therefore, a further condition is implemented to better isolate the foam timescales.

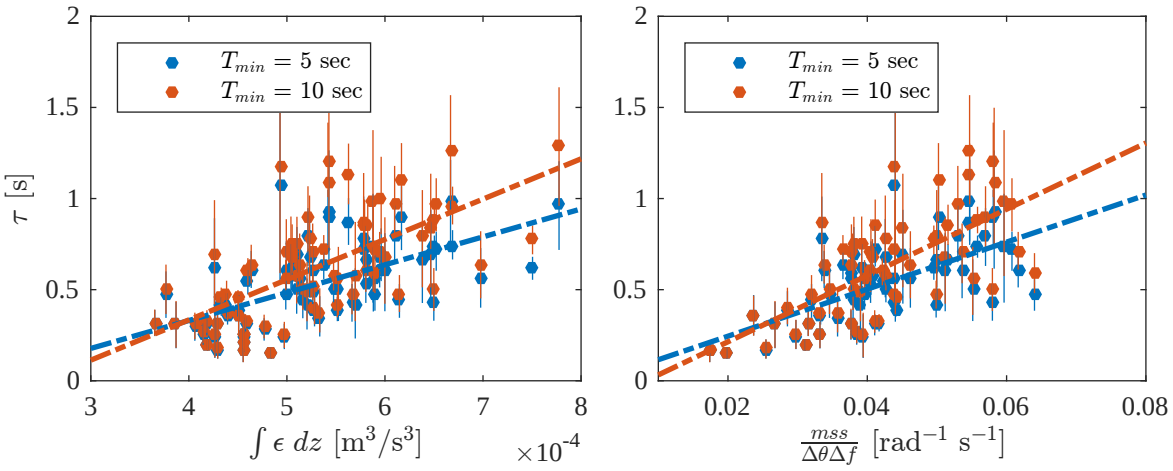

Figure 3.11: The characteristic residual foam time, τ, calculated using T_{min} = 5 seconds (blue), and T_{min} = 10 seconds (orange), plotted against (a) the turbulent dissipation rate, and (b) normalized mean square slope. The dashed lines are linear best fits.

Specifically, pixels are only counted in $I_{flipped}$ the first time they flip within a defined time frame, T_{min}. This assumes that all subsequent flips within T_{min} are assumed to be due to the same wave, therefore T_{min} should be on the order of the mean wave period, T_m, or between 5 and 10 seconds (see Figure 3.2).

In Figure 3.11, τ is plotted against the turbulent dissipation rate and normalized mss, for T_{min} equal 5 seconds and 10 seconds. Increasing T_{min} leads to slightly larger values of τ, but in either case a similar trend is apparent, namely, that steeper waves and increased dissipation are associated with an increase in residual foam. As mentioned above, this is likely due to bubbles being injected deeper into the water column for breaking under these conditions. This also shows that the increase in whitecap coverage with these quantities (as in Figures 3.6, 3.8, and 3.9) is not due to an increase in the rate of breaking alone, but is also the result of a transition to larger, longer-lasting, whitecap events.

Finally, in relating whitecap measurements to wave dissipation, it is tempting to switch from W to $\Lambda(c)$. But would it improve the results? The potential gain is from the additional

dependence on the breaker speeds. However, as discussed in Section 3.1, not only is the measurement of breaking speed problematic, most studies have shown the overall shape of $\Lambda(c)$ to be remarkably consistent. All together, Gemmrich et al. (2008), Thomson et al. (2009), Kleiss and Melville (2010), Gemmrich et al. (2013), Schwendeman et al. (2014) produce dozens of $\Lambda(c)$ with similar unimodal distributions, peaking somewhere in the range of 0.2 to 0.5 times the dominant phase speed, and decaying at a rate of around c^{-6}. In other words, the main dynamic parameter in $\Lambda(c)$ is its amplitude, or the total length of breaking crests per area, which is similar to the whitecap coverage. It is not surprising that the large scatter in W over the years (see Anguelova and Webster, 2006) is mirrored by similar variability in the breaking strength, b (see Schwendeman et al., 2014), since these approaches share many similar sources of uncertainty (e.g. image processing, microbreaking and residual foam, noisy ancillary measurements). For example, the negative residual trend of W with wave age shown here is a similar result to the increase in b with wave age shown in Gemmrich et al. (2008). One advantage of $\Lambda(c)$ is that it is a spectral measurement, and could potentially be used to calculate spectral wave dissipation. In practice, however, small errors in $\Lambda(c)$ are exaggerated by the calculation of the fifth moment, particularly for large c. Furthermore, if the breaking strength is indeed spectral (as in Romero et al., 2012), that value has not yet been well validated.

3.5 Conclusion

Whitecap coverage was measured during two experiments in the North Pacific Ocean, and was found to correlate in varying degrees with wind speed and wind stress, wave steepness, and turbulent dissipation. Interestingly, no significant differences in W were found when decreasing the camera pixel footprint by an order of magnitude in the 2015 experiment. The coefficients and errors for a threshold power law fit to W and each variable are compiled in Tables 3.2 and 3.3. The residuals of these fits were used to investigate potential biases in the parameterizations.

The fit to U_{10} has the best overall statistics, and shows good agreement with U_{10} relations

from similar recent studies (Stramska and Petelski, 2003; Sugihara et al., 2007; Callaghan et al., 2008a), particularly where the density of data is high (roughly $7 \leq U_{10} \leq 14$ m/s). There is a general leveling off of whitecap coverage at high winds, as was also shown in Callaghan et al. (2008a). There is some minor evidence of bias in the $W(U_{10})$ relation due to wave development, as inferred from measurements of wind acceleration and wave age. However, the variability in the residuals is large relative to these secondary trends.

Of the wave slope parameterizations, the best correlation is with the mean square slope of the equilibrium range waves, defined as $\sqrt{2}f_m \leq f \leq \sqrt{5}f_m$. This is probably because the majority of whitecaps form in this range. Meanwhile, other bulk steepness values are based on the dominant waves or are influenced by swell. The worst parameterizations involve the "peak" variables, which may be completely associated with swell. The fit to equilibrium range mss is further improved by normalizing by the directional spread and frequency bandwidth.

Whitecap coverage does correlate with turbulent dissipation, but the variability is larger than for the wind or wave parameters. The best fit is not linear, as has frequently been proposed, but the large scatter means a linear trend cannot be completely dismissed. The residuals show a strong trend with wave age, possibly related to microbreaking. There are clear parallels to the $\Lambda(c)$ literature, due to many similar sources of uncertainty.

Chapter 4

MEASUREMENTS OF WHITECAP GEOMETRY AND STEEPNESS FROM A SHIP-BASED STEREO VIDEO SYSTEM[1]

4.1 Introduction

The breaking of surface waves in deep water has been an active topic of research for decades, due to its importance for safety at sea, wave forecasting, and air-sea interactions (Melville, 1996). Progress has been slow, as the physics of breaking are complex, and the necessary measurements challenging. Two questions in particular remain unresolved: what causes a wave to break (breaking onset), and how much wave energy is lost during breaking (breaking dissipation) (Babanin, 2011). Advances have been primarily made through numerical and laboratory simulations, as measurements of oceanic breakers, or "whitecaps," are particularly difficult (Perlin et al., 2013). In the following paper, observations of whitecaps are presented from a ship-based stereo video system. The focus is on the geometry of the breaking waves, especially their steepness, which is thought to be a critical factor for both onset and dissipation.

In deep water, the geometry of a linear monochromatic wave is fully determined by just two parameters, the wave height, H, and wave length, L, and thus the steepness may be described as simply the ratio H/L. In a real wave environment, however, the waves are neither monochromatic nor linear, which complicates the description of the wave geometry. Still, the steepness is often discussed using the familiar H/L ratio, or sometimes ak, where $a = H/2$ is the wave amplitude and $k = 2\pi/L$ is the radian wavenumber. Stokes (1880) was the first to derive a limiting condition for the geometry of propagating surface waves, which

[1]This chapter will soon be submitted to the Journal of Physical Oceanography.

is a sharp crest forming a 120° corner. Others have shown that such a crest is formed for a monochromatic nonlinear wave with steepness $H/L \approx 1/7$ or $ak \approx 0.443$ (e.g. Williams, 1981). Mathematically, the peak of the limiting crest forms a singularity where the underlying fluid velocity exactly matches the phase speed of the crest.

The Stokes limit was thus the first supposed breaking criterion, the assumption being that waves would grow until this limiting geometry, at which point they would break. However, measurements from laboratory waves (Rapp and Melville, 1990) and field experiments (Holthuijsen and Herbers, 1986; Weisman et al., 1984) have suggested that waves break well below the Stokes steepness. In a field study using buoy estimates of steepness and human observers to detect breaking, Holthuijsen and Herbers (1986) found that whitecaps could not be distinguished from non-breaking waves by steepness alone (although the breaking waves were found to be slightly steeper on average than the non-breaking waves).

However, some laboratory experiments, including those of Brown and Jensen (2001) and Tian et al. (2010), have shown waves breaking near the Stokes limiting steepness. In particular, Babanin et al. (2007) made a renewed case for the applicability of the Stokes limit. In that study, measurements of breaking were presented in numerical and laboratory simulations of an initially monochromatic wavetrain. Due to the Benjamin-Feir instability mechanism, these waves quickly evolved into modulating wave groups, which led to wave steepening and eventual breaking. The numerical simulations were carried out using the fully nonlinear Chalikov-Sheinin model of Chalikov (2005), which is capable of simulating waves up to the point just before surface overturning. The waves simulated in this method became significantly steeper than previous simulations, such as Song and Banner (2002). Prior to breaking, the local steepness of the numerical and laboratory waves closely matched the Stokes limit.

Chalikov and Babanin (2012) used the same numerical method as Babanin et al. (2007), initialized from a JONSWAP spectrum and random phase components. In this configuration, which more closely resembles the natural ocean environment, the simulations no longer showed waves consistently approaching the Stokes steepness prior to breaking. Instead,

individual waves often became unstable at much lower bulk steepness. Additionally, the superposition of waves of different scales made defining a wave more difficult, and introduced large scatter to the wave-by-wave analysis. The most consistent indication of imminent breaking was the presence of large surface slopes or curvature (also noted in Tian et al., 2012). However, these features were highly localized, often developing within fractions of a wave period from the breaking point.

Wave steepness has also been shown to be an important factor in the dissipation of wave energy during breaking. For example, Rapp and Melville (1990) showed that the relative energy loss was strongly dependent on the wave steepness, with some scatter due to the packet bandwidth and central wavenumber. Similar results have since been shown in Banner and Pierson (2007), Drazen et al. (2008), and Tian et al. (2010). Subtle differences in calculating the energy flux and wave steepness makes comparing across the studies somewhat difficult. However, the general agreement is that steeper waves lose a larger percentage of their energy flux during breaking.

Steepness may also be incorporated into the Duncan/Phillips dissipation framework, which comes from the experiments of Duncan (1981) and the analysis of Phillips (1985). In scaling the dissipation, Phillips (1985) introduced a "breaking strength" parameter, b, which was assumed to be constant. However, Melville (1994) showed experimental evidence that b depends on the wave steepness. Drazen et al. (2008) argued that

$$b \propto (ak)^{5/2} \tag{4.1}$$

where ak is the breaking wave steepness, based on a "ballistic scaling" of a plunging breaker. This scaling was supported by a series of laboratory experiments.

The idea of using stereo imagery to measure ocean waves has a long history (see, for example, Holthuijsen, 1983), but only recently has it become realizable for most researchers. This is due to the rapid growth in computing power and camera technology, as well as the increasing availability of sophisticated computer vision algorithms. In stereo video, pixels are matched between images from two or more cameras overlooking the same patch of the sea

surface. Through triangulation, the distance to the water surface is estimated at each pixel, which produces a three-dimensional reconstruction of the surface. The ability to resolve the spatial wave geometry is a distinct advantage over point-based *in situ* wave measurements, such as buoys and wave staffs.

Still, measuring waves with stereo imagery has its own difficulties. Jähne et al. (1994) provides a critical review of the theoretical limitations, including resolution, occlusion, and specular reflection. Benetazzo (2006) gives a good overview of early efforts at stereo video, and provides quantitative estimates of the errors involved. Benetazzo (2006), Wanek and Wu (2006), and de Vries et al. (2011) showed that measurements of waves with stereo video compared well with more traditional *in situ* measurements. However, these studies were of small waves (significant wave heights between 20-60 centimeters), and taken from stationary nearshore platforms. In the last five years, innovations in the stereo methodology have led to its use in increasingly diverse conditions. For example, the work of Benetazzo et al. (2012) improved upon the image processing of Benetazzo (2006) and moved the system to an offshore platform, such that they measured significant wave heights greater than 2 meters.

Researchers have used stereo wave measurements to explore a variety of scientific questions. For example, Sutherland and Melville (2013) used stereo-processed infrared imagery to estimate the dissipation of breaking waves, including micro-scale breakers, using the Duncan/Phillips scaling. Fedele et al. (2013) compared the wave statistics in space-time stereo images with nonlinear theoretical predictions. Most recently, Benetazzo et al. (2015) investigated the statistics of extreme waves and Leckler et al. (2015) examined the shape of the full frequency-wavenumber spectrum in young wind waves.

In this chapter, we present measurements of open ocean waves from a shipboard stereo video system installed on the R/V *Thomas G. Thompson* during a recent cruise to Station P in the North Pacific. This contrasts with the above studies, which have each utilized stereo measurements from stationary towers or platforms. A similar ship-mounted system has recently been described in Benetazzo et al. (2016). The additional difficulties of ship-based measurements include accurate camera calibration and the removal of underlying ship

motion. For example, they describe an auto-calibration procedure for determining the camera intrinsic and extrinsic parameters needed to perform the stereo processing. In addition, Benetazzo et al. (2016) show that a planar fit to the stereo point cloud could be used to determine and remove the motion of the ship, but only when the field-of-view encompasses several full wavelengths. Here, a more traditional "checkerboard" calibration was found to be adequate, and the ship motion was measured independently from a combined inertial motion unit and global navigation satellite system, as noted in Section 4.2. One similarity with the method of Benetazzo et al. (2016) is in the use of the Hirschmuller (2008) "semi-global" stereo matching algorithm, which has many advantages over traditional "block-matching" methods, including sub-pixel accuracy. Finally, although Benetazzo et al. (2016) propose several practical uses of ship-based stereo imagery, they do not emphasize the study of breaking waves. Here, we focus on the geometry and steepness of open ocean whitecaps. The chapter proceeds as follows: Section 4.2 describes the stereo methodology, while Section 4.3 validates the results against linear theory and *in situ* wave measurements. In Section 4.4, the whitecaps are investigated in further detail. Section 4.5 provides discussion, and Section 4.6 concludes.

4.2 Methods

4.2.1 Instrumentation

Measurements were made during a research cruise onboard the R/V *Thomas G. Thompson* in the North Pacific Ocean. The ship departed from Seattle WA on 27 December 2014 and returned on 14 January 2015, with the primary objective of replacing a moored wave buoy at Station P (50° N, 145° W). On several days the ship paused in the transit to hold station into the wind and collect measurements of the local wave conditions. The R/V *Thompson* is equipped with bow and stern thrusters and a dynamic positioning system, which allow it to keep a relatively stationary position even in rough seas. Conditions varied from quite calm ($U_{20} < 1$ m/s, $H_s = 1.3$ m) to large winter storms ($U_{20} = 23$ m/s, $H_s > 6.0$ m).

A stereo video system was installed for this cruise, which consisted of two Pt. Grey Flea2 cameras. The cameras were separated by two meters along the rail just forward of the bridge, approximately 12 meters above the mean sea surface, with a look angle approximately 12.5° below horizontal. Identical systems were located on both the port and starboard sides, making it easy to switch sides depending on the position of the sun or clouds. Each stereo camera was equipped with a 9 mm fixed focal lens, and placed in a weather-proof housing. Each side had an additional Pt. Grey Flea2G camera recording a wider field-of-view (2.8 mm focal length). This camera was used heavily in Schwendeman and Thomson (2015b) for estimating whitecap coverage. It also kept the horizon in view in most frames, allowing for calculation of the camera pitch and roll as described in Schwendeman and Thomson (2015a). The port side cameras were mounted next to a Novatel combined inertial motion unit (IMU) and global navigation satellite system (GNSS), which measured the cameras' position and rotation.

While the ship held station with the stereo system recording, *in situ* measurements were made of the local wave spectra. Two varieties of drifting buoys were used, usually deployed at dawn and recovered at dusk. Datawell DWR-G4 Waveriders measured the horizontal wave orbital velocities with GPS, from which the wave frequency spectrum, $E(\omega)$, mean wave direction, $\overline{\theta}(\omega)$ and directional spread, $\Delta\theta(\omega)$ were calculated. The spectral calculations were made over 30-minute intervals using Datawell's built-in processing (de Vries, 2014). Meanwhile, custom-built SWIFT drifters, described in Thomson et al. (2016), used an onboard IMU to measure the buoy acceleration and orientation, and produced frequency spectra and directional moments on 10-minute intervals. The ship's sonic anemometer measured the true wind speed throughout the cruise, at a height of roughly 20 meters above the mean water line.

4.2.2 Stereo Processing

Proper stereo measurements require good synchronization and calibration of the cameras. Synchronization to within 10 μs was achieved by using a Pt. Grey IEEE 1394 (Firewire)

hub, and the cameras were calibrated using the checkerboard routine included in Matlab's Computer Vision Toolbox. For the calibration procedure, a 10×5 array of 4" black and white squares was shown to both cameras in their ship-mounted positions, which allowed the calibration algorithm to optimize both the extrinsic and intrinsic camera parameters. Prior to 01 January, the stereo cameras were run at 5 Hz; afterwards the frame rate was set to 7.5 Hz. The Novatel IMU/GNSS data was recorded on a separate computer from the stereo imagery, which resulted in a small unknown time offset between the two data streams. This was determined in post-processing using a cross-correlation of the time series of pitch and roll from the camera horizon method (Schwendeman and Thomson, 2015a) with pitch and roll from the Novatel system. The IMU/GNSS data was then shifted to line up with the images.

The steps of the stereo image processing are outlined in Figures 4.1 and 4.2, on a pair of images showing a large whitecap in the center of the field of view (this same example whitecap is also used in Figures 4.8 and 4.10). The first step is stereo rectification, which is the process of transforming images such that pixel rows are epipolar lines. With the stereo cameras facing approximately parallel to one another, the rectification only slightly warps the images. The rectified images are shown in Figure 4.1a,b. Next, the semi-global algorithm from Hirschmuller (2008), as implemented in the Matlab Computer Vision Toolbox, is used to calculate the disparity map, which is the image that maps pixels from the left rectified image to the right rectified image. Figure 4.1c shows the disparity result. The missing data on the left of the disparity map corresponds to the region of the images which do not overlap. Some points in the disparity have more uncertainty than others, due to low texture in the image. Matlab's implementation allows for several options to exclude the low quality data. There is an unavoidable trade-off, since excluding pixels leads to holes in the disparity map, but including more points results in errors and noise. A number of quality control settings were tested, with the best results shown in Figure 4.1c. These use the Matlab default block size of 15 pixels and contrast threshold of 0.5, and a slightly larger uniqueness threshold of 25. In addition, a 5-pixel square median filter was applied to the disparity images to reduce

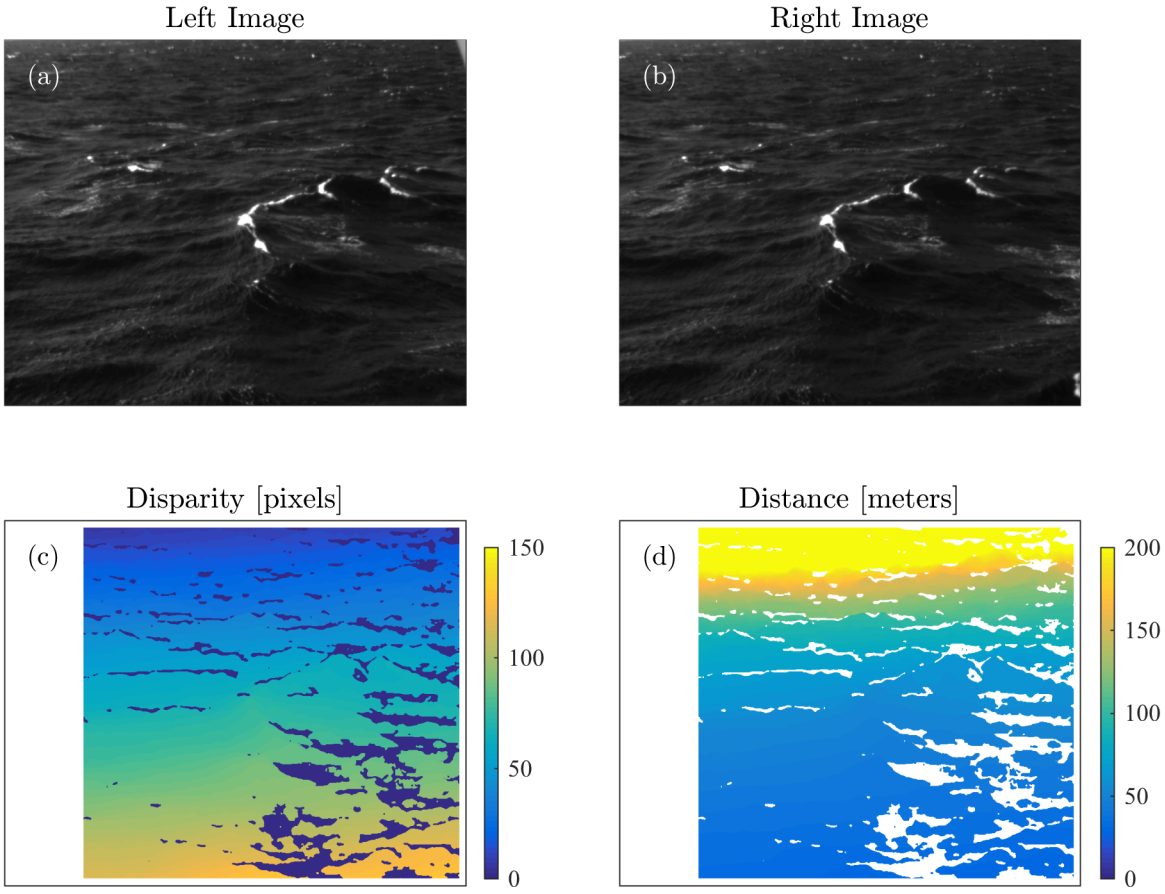

Figure 4.1: An example showing (a,b) a pair of rectified stereo images, (c) the resulting disparity map, and (d) the subsequent image projection. The left side of the disparity is cut-off where the images do not overlap, and the holes in the disparity are where the confidence in the solution is low. The same example whitecap is shown in Figures 4.2, 4.8, and 4.10.

speckle noise.

At each pixel, the value of the disparity is inversely related to the range distance, r, of the sea surface to the camera,

$$r_{i,j} = \frac{f}{d_{i,j}} \tag{4.2}$$

where f is the camera focal length and $d_{i,j}$ is the disparity at pixel (i, j). Figure 4.1d shows the pixel-wise distance image calculated from Equation 4.2. The dominant signal is the tilt of the roughly flat sea surface relative to the oblique camera.

To reveal the waves, the measurements are rotated into an earth reference frame, in which the long-time mean sea surface is a plane at height zero with normal vector aligned with gravity. The rotation is performed using the synchronized IMU-GNSS data. Alternatively Benetazzo et al. (2016) show that this rotation can be made by fitting a plane to each image, however, this method requires a large spatial field-of-view relative to the length of the waves. The data now make up a scattered point cloud, with each point corresponding to a pixel in the disparity map. The point cloud data is unstructured and difficult to analyze. Therefore, the final step is to interpolate the data onto a regular grid, as shown in Figure 4.2, using a scattered bilinear interpolation. The grid spacing is 25 cm, which is similar to the average spacing in the unstructured point cloud. The gridded elevation product (Figure 4.2a) is heavily used in the following sections. Additionally, a similar interpolation can be performed on the original image pixel brightness values, resulting in an earth-referenced radiance product, as shown in Figure 4.2b. The radiance image looks blurred because the interpolation to a uniform grid tends to smear out the small, rough waves that provide much of the texture. However, the bright foam from whitecapping still shows up clearly, as seen in Figure 4.2b. An additional translation and rotation is performed to bring the origin to the center of the field-of-view and the x-axis inline with the average wind vector. Usually the ship was pointed directly into the wind, such that this rotation is small. A video example of the rendered elevation/radiance products is included as supplemental material.

Although roughly 45 hours of stereo video were taken, the data quality was highly variable, due to variations in the natural lighting conditions and occasional rain. Ten video

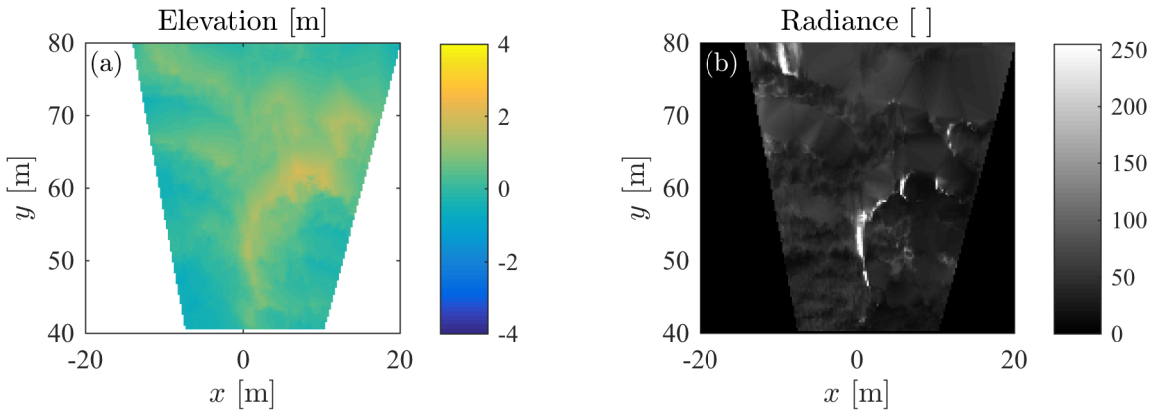

Figure 4.2: The same example from Figure 4.1, showing the (a) elevation and (b) radiance data products found by interpolating the stereo result onto a rectangular grid. These gridded products are later rotated such that the wind is in the +x direction.

bursts stood out as the highest quality, and data products were calculated for their full durations, between 20 and 60 minutes each. A further 45 recordings were found to be of mostly good quality, from which five minutes each of video were processed. The remaining data were found to be too poor to warrant further examination and were not processed.

4.3 Validation

The stereo wave measurements are first validated using the *in situ* measurements of the SWIFT and Waverider buoys. For this comparison, each point in the gridded elevation product is processed as an independent time series. Frequency spectra, $E(\omega)$, are calculated from the elevation time series at each point and averaged to a single spectrum for each video burst, from which the significant wave height, $H_s = 4[\int E(\omega)\, d\omega]^{1/2}$, and mean wave period,

$$T_m = \frac{2\pi \int E(\omega)\, d\omega}{\int \omega E(\omega)\, d\omega}, \tag{4.3}$$

are calculated. These are plotted as a time series over the whole experiment in Figure 4.3, along with the SWIFT and Waverider quantities when available. The time series show the

wide range of conditions observed over the course of the experiment. During video recording, the buoys measured significant wave heights between 1.2 and 5.5 meters, and mean wave periods between 5.7 and 9.4 seconds.

These measurements are subject to small amounts of uncorrected ship motion, including from surge and sway (RMS velocity fluctuation ≈ 0.3 m/s), heading (RMS angle $\approx 2°$), and a small net drift (mean velocity ≈ 0.8 m/s). Still, it can be seen that the stereo measurements follow the buoy data quite well overall, with a few exceptions. For example, the stereo measurements overestimate H_s on 31-Dec and 01-Jan, and underestimate T_m on 03-Jan. The H_s overestimation is likely a result of noise, which increases the variance in the data. The underestimate of T_m may be due to missed energy at the low frequencies, which is discussed more below.

The stereo and buoy data are further compared in Figure 4.4, from which a few additional trends can be seen. The H_s data agree quite well for wave heights up to about 4 meters, but for larger waves the stereo measurements have the tendency to overestimate H_s. Meanwhile, the stereo T_m on average underestimate the buoy values. The mean wave steepnesses, H_s/L_m, are also compared, using L_m calculated from the linear dispersion relation. The small scatter in H_s and T_m are amplified in this calculation. Despite this, the buoy and stereo measurements are still clearly consistent.

Three frequency spectra from the stereo video are compared to SWIFT and Waverider spectra in Figure 4.5. These examples are drawn from the full video captures (crosses on Figures 4.3 and 4.4) from three different days (note that no SWIFT data is available for the December 28th example). The measurement times do not overlap exactly, as the Waverider spectra are calculated every 30 minutes, the SWIFT spectra every 10 minutes, and the stereo measurements last between 30 and 60 minutes. Plotted in gray are spectra from each stereo grid point, with the average spectra in black. Overall, the frequency spectra are similar in shape to those calculated from the buoy. Figure 4.5 also shows wavenumber spectra calculated from the stereo data for the same examples. The wavenumber spectra are calculated in x (the wind direction) for each video frame, at every y. Here the light gray

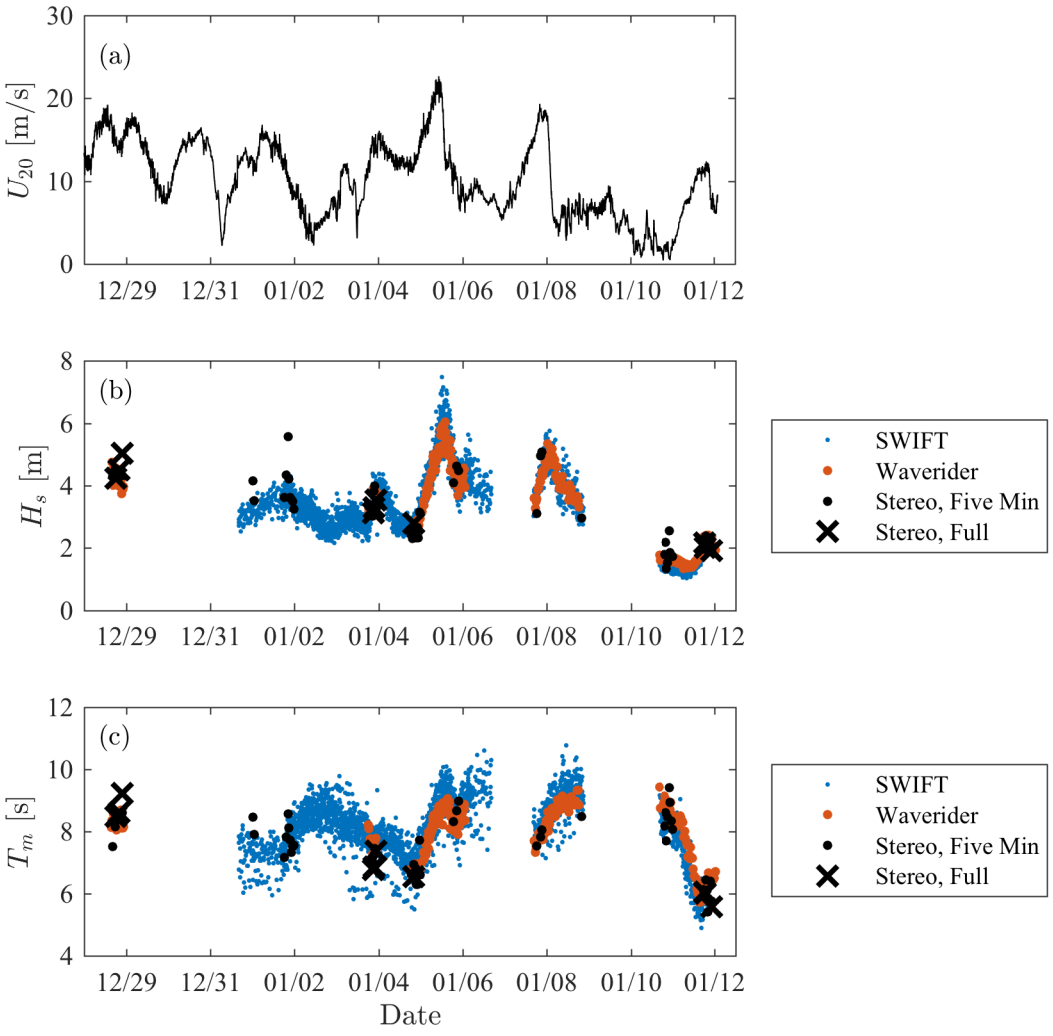

Figure 4.3: Time series of (a) 20-meter wind speed, U_{20}, (b) wave height, H_s, and (c) energy-weighted mean period, T_m. The wind speed is measured from the ship, while the wave quantities are measured from SWIFT (blue circles) and Waverider buoys (orange circles), and from the stereo video (black circles = 5-minute video segments, black x's = full video segments).

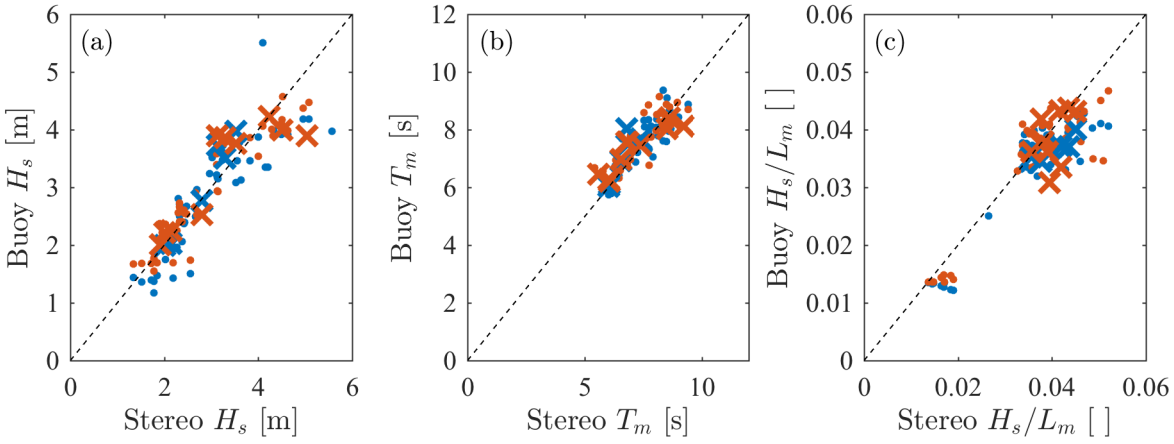

Figure 4.4: Comparison of (a) significant wave height, H_s, (b) mean period, T_m, and (c) significant steepness, H_s/L_m, from the stereo video and buoys (SWIFT in blue, Waverider in orange). Circles are from the 5-minute video segments, and x's are from the full video segments.

curves show the average spectra at each y, while the red line shows the total average. These direct measurements of the wavenumber spectrum are compared with the frequency spectra transformed to wavenumber using linear dispersion with no current.

Although the spectral comparisons provide good validation for the stereo processing, they also point to some of the limitations of the stereo data. The main difference with the buoy spectra is in the lower frequencies, less than 0.5 rad/s, where the stereo measurements do not reproduce some of the buoy energy. This is likely the reason that the stereo T_m are slightly less than the buoy values, as shown in Figure 4.4. For example, in the January 11th example there is a peak in the swell around 0.4 rad/s (16 second period), that is not seen at all in the stereo spectrum. Since these swell waves are much longer than the width of the stereo FOV, correctly measuring them depends on the shipboard IMU/GNSS to accurately account for the vertical motion of the cameras. Unfortunately, this measurement is prone to drift, and required the application of a high-pass filter. This filter was designed to pass energy for frequencies above $\pi/10$ rad/s, however, which does not explain the difference at

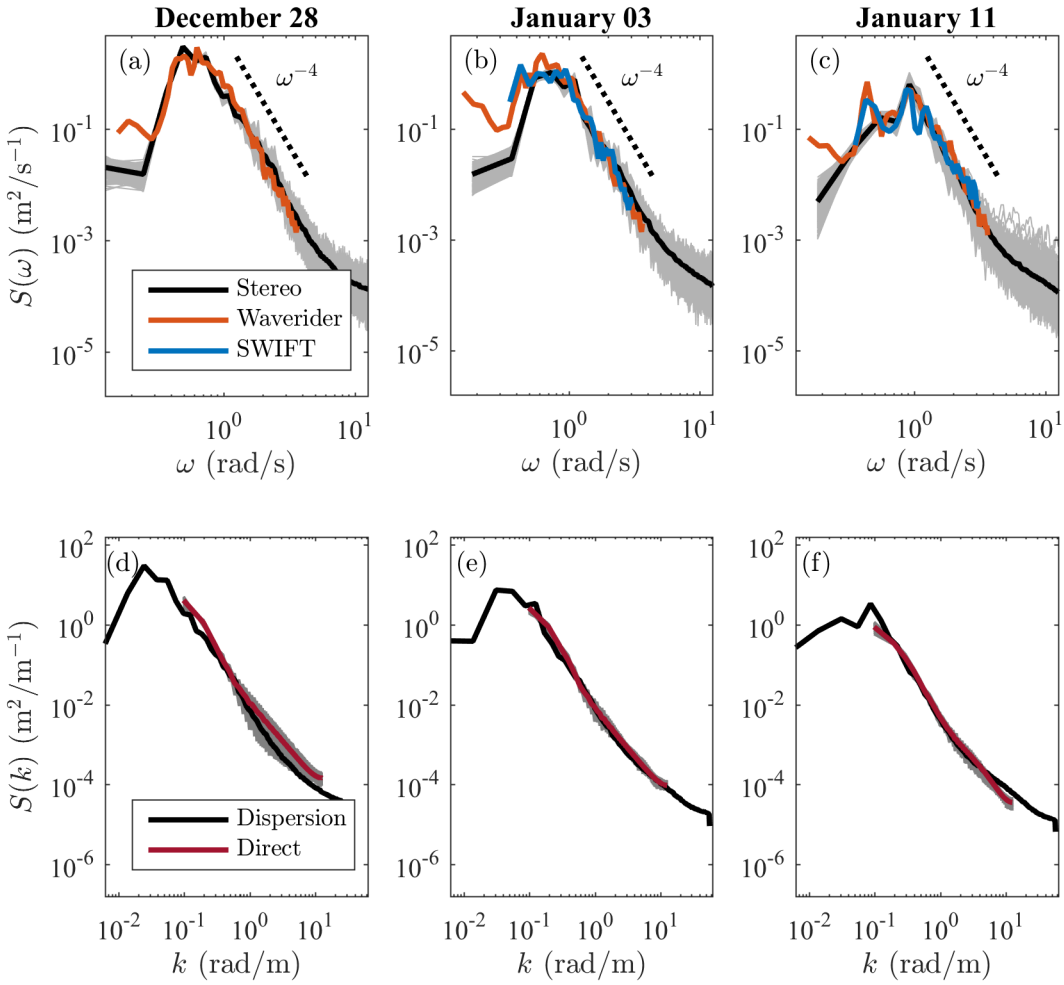

Figure 4.5: Comparison of three wave spectra, from three different days during the experiment. (a-c) Frequency spectra, measured from the SWIFT (blue), Waverider (orange), and stereo video. Gray lines are the spectra measured at each (x, y) in the stereo elevation product, with the black line as the average. (d-f) Wavenumber spectra, measured directly from the stereo video along the x direction (each y shown in gray, overall average in red), and from the frequency spectra transformed using the linear dispersion relation (black).

0.4 rad/s. Regardless, the effect on the remainder of the analysis should be minimal, as these long-period swells are not of primary importance for the wave breaking.

At the higher frequencies, the spectra are expected to decay as a power law, $S(\omega) \propto \omega^{-n}$, where n approximately equals 4 or 5 (see Banner, 1990). Indeed, the stereo spectra show such behavior initially, but at larger frequencies noise begins to flatten the signal. This noise is likely related to small errors in the disparity calculations and in the linear interpolation of the data onto the rectangular grid. The noise starts to be noticeable around roughly 5 rad/s, corresponding to waves of 2.5 meter wavelength. Small differences are seen in the comparison between the directly calculated wavenumber spectra and the transformed frequency spectra, particularly on December 28th. These may be due to the secondary ship motions (small oscillations in surge, sway, and heading, plus a slow drift) or small surface currents, which introduce a Doppler shift in the frequency spectra that is not present in the wavenumber spectra.

Most importantly, the wavenumber spectra reveal the effect of the relatively small field-of-view of the cameras, which is between 20 and 40 meters in the x direction (depending on the range). The field-of-view does not resolve a full wavelength of the most energetic waves, which are between 50 and 200 meters long. Fortunately, previous studies have shown that many of the breaking waves are shorter than the peak or dominant waves (e.g. Gemmrich and Farmer, 1999). Still, the limited field-of-view does make certain analysis difficult or impossible, such as tracking the evolution of wave groups or measuring the dissipation from individual waves breaking. The spectra show that the region of best performance in the stereo data is for wave periods between 2 to 10 seconds and wavelengths between 5 to 50 meters.

Finally, the probability density function (PDF) of the stereo surface elevation data is examined. PDFs are calculated over all x and y, and Figure 4.6 shows the average for each of the 10 full videos. The elevations are expected to be quasi-Gaussian (Forristall, 2000), such that large deviations from a Gaussian distribution would indicate bias in the stereo data. In particular, because of the oblique camera angle, a major concern is occlusion, or

shadowing, of the wave troughs in the far-field by the crests in the near-field. Figure 4.6 confirms that the surface elevations are near-Gaussian to at least three standard deviations. Beyond this point, there is a noticeable deviation from the Gaussian distribution, with more large positive elevations than low negative elevations. However, this is physically expected due to wave nonlinearity, and is not necessarily indicative of measurement bias (Longuet-Higgins, 1963). The plot is cut off where the statistics become less reliable, as the time scale of occurrence approaches the length of the video records. Overall, the effect of occlusion appears relatively small in the elevation PDFs.

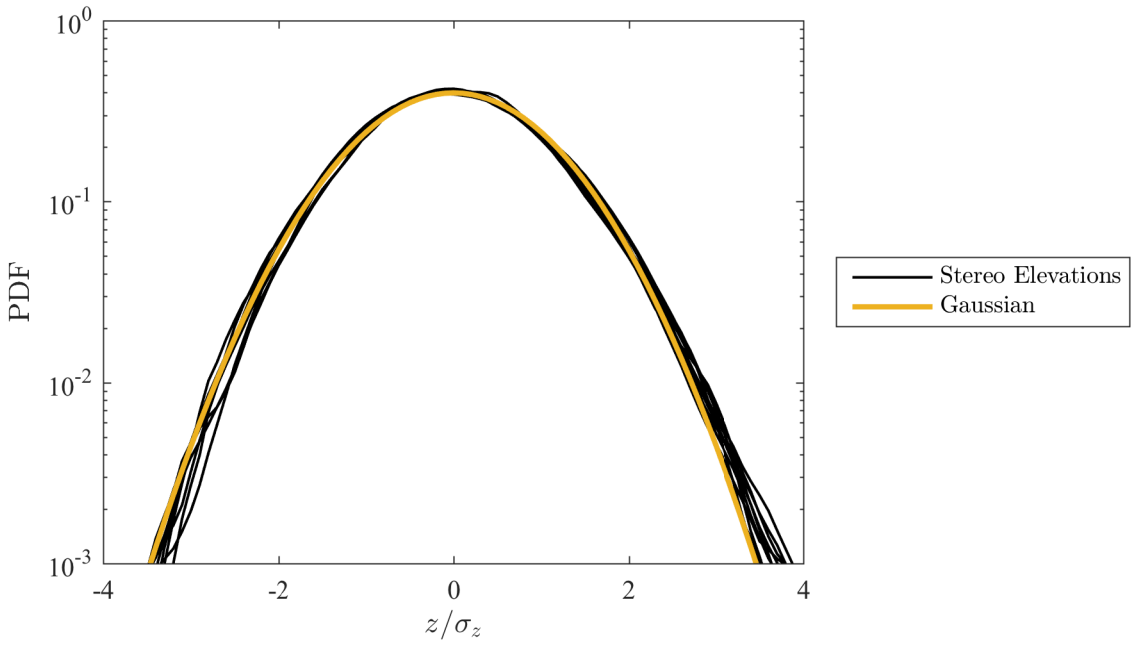

Figure 4.6: The probability density function of surface elevation from the 10 full stereo video bursts (black), compared with a normal Gaussian distribution (yellow).

In summary, comparison of the stereo elevation product with buoy data and linear wave theory reveals the data to be good overall, with some notable limitations. In particular, the small size of the field of view, the effect of noise on the high frequency waves, and the small uncorrected ship motions must all be acknowledged. With this in mind, the following

analysis of the wave-breaking focuses on the prominent, intermediate-length whitecaps, which are well-resolved by the stereo measurements.

4.4 Results

4.4.1 Bulk metrics and distributions of wave steepness

Traditionally, estimates of steepness are only available from temporal measurements, which usually employ frequency spectra or zero-crossing analyses. Most commonly, the average wave steepness is given as the significant wave height, H_s, divided by a characteristic wavelength, such as the spectral peak wavelength (L_p) or energy-weighted mean wavelength (L_m). The characteristic wavelength is usually calculated in frequency space and transformed to a wavelength using the linear dispersion relation. Studies such as Holthuijsen and Herbers (1986) instead partition the time series of surface elevation into individual waves using a zero-crossing method, which allows a steepness, $S_i = H_i/L_i$, to be measured for each wave. In either approach, linear dispersion is needed to transform the time domain signal from a point measurement into a wavelength for measuring steepness.

The stereo video data are uniquely suited for more direct estimates of steepness. Since the gridded elevation product contains both spatial and temporal information, the actual surface slope can be measured rather than inferred from dispersion. The magnitude of the surface gradient, $|\nabla z(x,y)| = [(\partial z/\partial x)^2 + (\partial z/\partial y)^2]^{1/2}$, is calculated from the gridded elevation data using the central difference to approximate the partial derivatives. A circular Gaussian filter of 1-meter standard deviation is applied prior to differencing to reduce the effect of high-frequency noise in the discrete difference.

Figure 4.7 shows how $|\nabla z(x,y)|$ relates to the steepness calculated from point measurements (using spectral or zero-crossing methods). First, Figure 4.7a shows the probability density function (PDF) of $|\nabla z(x,y)|$, colored by the significant steepness, H_s/L_m, as calculated from the stereo frequency spectra. It is clear that for larger H_s/L_m, the distribution of $|\nabla z|$ is also skewed higher. This is also seen in Figure 4.7c, which shows a roughly linear

relationship between H_s/L_m and the median gradient, $\overline{|\nabla z|}$.

Normalizing the gradient by $\overline{|\nabla z|}$, as in Figure 4.7e, shows that for moderate values of $|\nabla z(x,y)|$, the distributions are highly similar. The curves are well fit by the theoretical probability density function of slope derived by Liu et al. (1997),

$$P(|\nabla z|) = \frac{n}{n-1}\frac{|\nabla z|}{\sigma^2}\left[1+\frac{|\nabla z|}{(n-1)\sigma^2}\right]^{-(n-2)/2} \tag{4.4}$$

using $\sigma = 0.83\overline{|\nabla z|}$ and $n = 7.0$. This model assumes independent distributions of wave height and wave period. As discussed in Liu et al. (1997), deviations from this assumption increase the probability density of high surface slopes, which can be be reproduced by decreasing n. The observations show that above 2 to 3 times $\overline{|\nabla z|}$, the individual PDFs begin to diverge. Also shown is the fit to the data using $n = 3$ (the upper curve at large gradients) and $n = 40$ (lower curve), which also match the distributions in the low and moderate slopes, but bracket the data at high slopes. For comparison, Liu et al. (1997) found that the measurements of Cox and Munk (1954) could be fit using a range of $6 \leq n \leq 100$. Physically, large values of n indicate a narrow distribution of the wave frequency. As discussed in Babanin (2011), the frequency bandwidth is related to the modulational properties of the dominant waves (i.e. the wave groups). Thus, the probability of large surface slopes increases when wave groups are pronounced.

The distribution of wave steepness is also shown using a zero down-crossing method, as in Holthuijsen and Herbers (1986). Specifically, elevation time series are made from (x,y) points taken every 5 meters, resulting in 81 virtual wave gauges (although several have no data due to the shape of the field-of-view). In each time series, waves are identified as lying between the two nearest points where the elevation crosses from positive to negative. For each wave, a steepness S is calculated as the difference between the maximum and minimum elevation, divided by the estimated wavelength, using linear dispersion and the period between down-crossings. Figure 4.7b shows the PDFs of S, again colored by H_s/L_m. It should be noted that the zero-crossing method is not ideal for these broad-band waves, where short waves riding on long waves may fully lie below or above the mean water line.

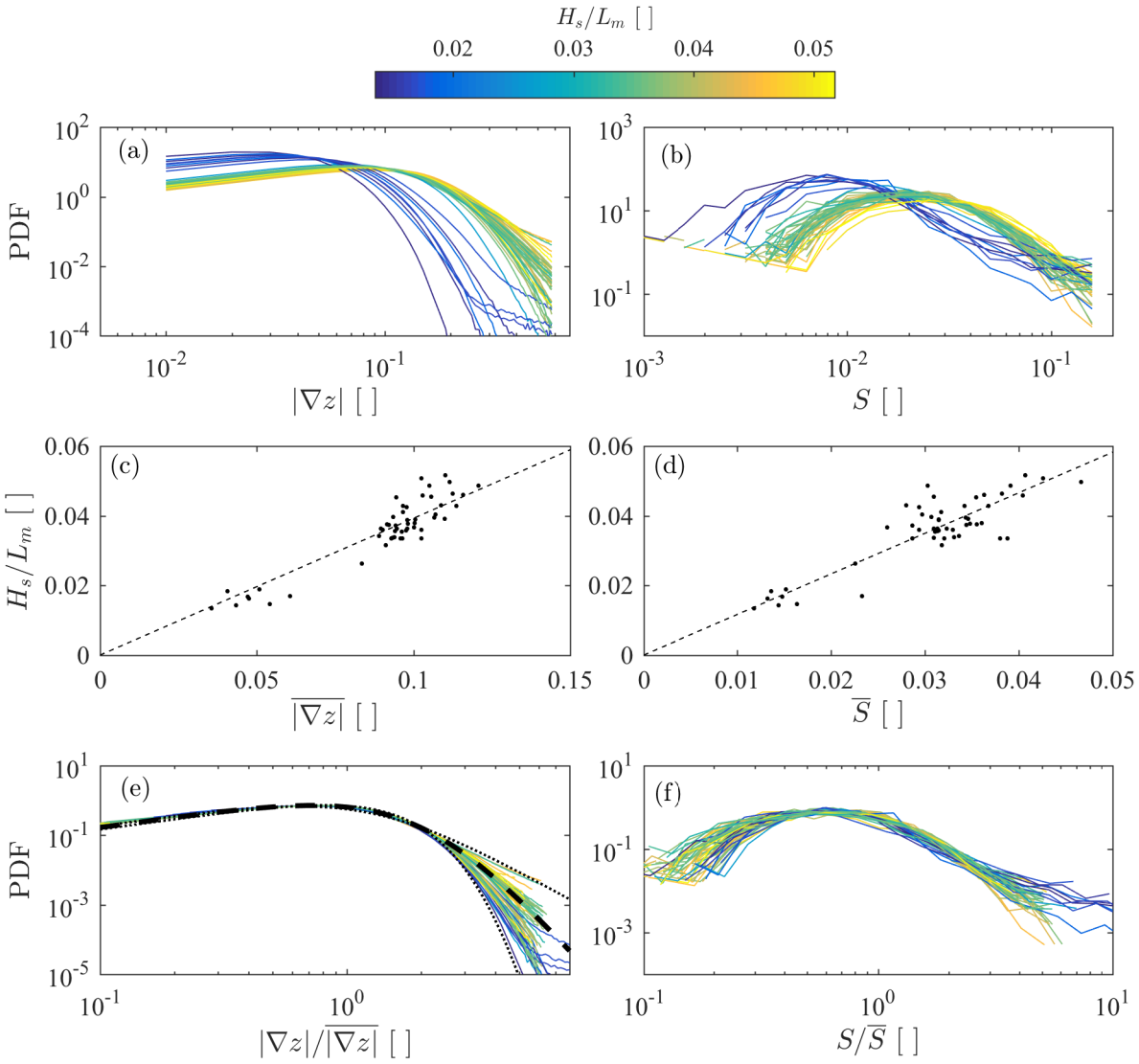

Figure 4.7: Probability density functions (PDFs) of (a) surface gradient magnitude, $|\nabla z|$, and (b) wave steepness from zero down-crossings, S, each colored by significant steepness, H_s/L_m. (c-d) H_s/L_m plotted against the median values of $|\nabla z|$ and S. (e-f) The PDFs scaled by their median values. The dashed line in (e) corresponds to the theoretical distribution of Liu et al. (1997) with $\sigma = 0.83\overline{|\nabla z|}$ and $n = 7.0$. Dotted lines are for fits using $n = 3$ (upper curve at large $|\nabla z|$) and $n = 40$ (lower curve).

Still, as with the surface gradient, Figure 4.7d reveals that the median wave steepness $\overline{S}$ is linearly related to H_s/L_m, and Figure 4.7f shows that the distributions are largely similar after scaling by $\overline{S}$. The main difference in using the zero-crossing steepness S is that each wave is assigned a single value of steepness, whereas the surface gradient magnitude $|\nabla z|$ captures variations in the instantaneous and local wave slope. The increase in data causes the PDFs of $|\nabla z|$ to be much smoother than those of S. Additionally, the PDFs of $|\nabla z|$ show a clear variability near the tail of the distribution, which is not visible in the PDFs of S. This is consistent with the hypothesis of Liu et al. (1997), who argue that the variation in the shape of the $|\nabla z|$ distribution is a nonlinear effect, which would not be captured by the zero-crossing method.

The statistics of the extreme surface slopes at the tails of the PDFs are important to understand physically, as they are likely related to the wave-breaking. Unfortunately, the tails of the distributions are also affected by noise. Thus, the PDFs of both $|\nabla z|$ and S were cut off at high steepness based on the Stokes limiting wave. Specifically, S was plotted out to $H/L = 0.1443$ and $|\nabla z| = \cot(120°/2) = \tan 30° = 0.5774$. To better understand the relationship of wave steepness to wave breaking, it is necessary to focus on the highest quality data, and to concentrate on the relative differences between the breaking and non-breaking waves.

4.4.2 Statistics of surface gradients and curvatures near whitecaps

In this section, the surface gradients are compared for whitecaps and non-whitecaps. For this and the remainder of the paper, the data come from only the 10 best-case video segments, each lasting between 20 and 60 minutes. At each frame, the maximum of $z(x, y)$ and $|\nabla z(x, y)|$ are calculated, as well as of the negative surface Laplacian, $-\nabla^2 z(x, y)$. As with $|\nabla z|$, smoothing is needed to prevent noise from dominating the signal of $\nabla^2 z$. Here, a Gaussian is used with standard deviation of 2.5 meters. The Laplacian of the elevation can be thought of as a measure of curvature, or "peakedness." A wave has negative $\nabla^2 z$ at its crest, and positive at the trough. Figure 4.8 shows the evolution of the example whitecap

shown in Figures 4.1 and 4.2 (it has been centered and rotated into the wind direction, as discussed in Section 4.2). The surface elevation, z, slope, $|\nabla z|$, and curvature, $-\nabla^2 z$, are all large in the vicinity of the whitecap. A thin region of large local steepness is visible on the front face of the whitecap, near the crest, about 1 second prior to the appearance of the whitecap (note the residual foam seen at $t = -2$ and $t = -1$ is from a previous whitecap). The sharp crest is reflected in the large negative surface curvature.

Meanwhile, whitecap pixels are detected by thresholding the radiance data product (i.e. the gridded pixel brightness), using the method of Kleiss and Melville (2011). This gives a 3-dimensional array of Boolean values, $W(x, y, t)$, in which a value of 1 indicates the presence of whitecap foam. However, W does not distinguish between the recently formed foam from active breaking, and the decaying foam left behind from past breakers. Therefore another variable, $\Delta W(x, y, t)$ is used which more closely follows the active breaking. This was introduced in Schwendeman and Thomson (2015b), and is calculated from W by simply negating pixels in W for a period of several seconds after they are initially flipped from 0 to 1. Since the residual whitecap foam tends to remain mostly stationary, these pixels are ignored in ΔW.

For each frame in the video, the total area of new foam is calculated as

$$\Delta W_t(t) = \sum_{x,y} \Delta W(x, y, t) dx dy. \tag{4.5}$$

Peaks in $\Delta W_t(t)$ indicate an active breaking event, and a threshold of $\Delta W_t(t) \geq 10$ m^2 is used to identify such events. The choice of this threshold is based on a visual examination of the data. A lower threshold identifies more breaking events, but is more likely to falsely identify breakers based on noise in $\Delta W(x, y, t)$, for example, from advection of residual foam. On the other hand, a higher threshold more accurately identifies true whitecaps, but ignores the frequent small events.

For comparison, non-breaking crests are identified from the statistics of the surface elevation alone. At each frame, the 95th percentile of the surface elevation is calculated. This gives a time series, $z_{95\%}(t)$ of the highest 5% of elevations in the spatial domain. A peak

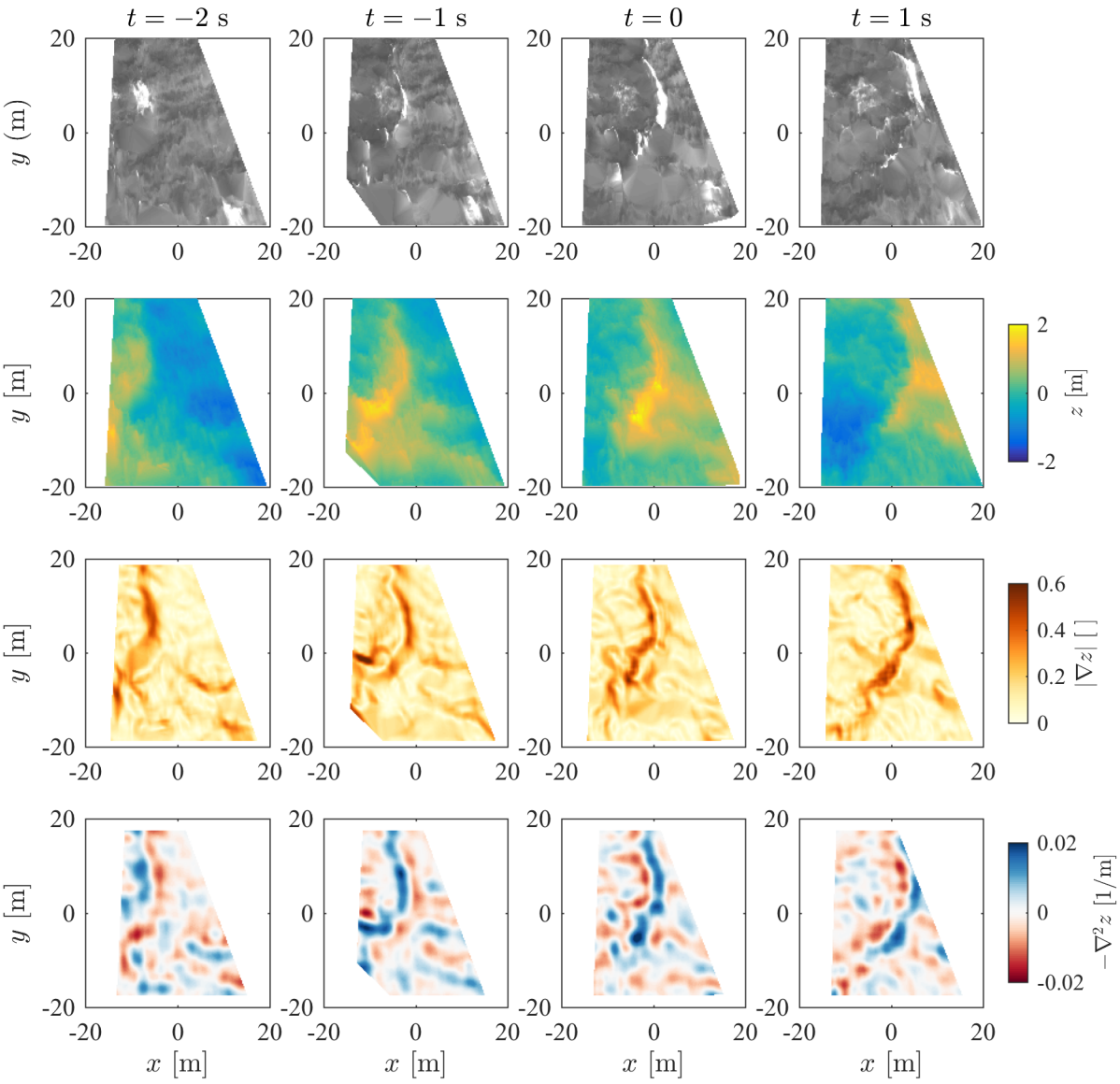

Figure 4.8: A series of measurements around the whitecap from Figures 4.1, 4.2, and 4.10. The progression of the surface radiance (top row), surface elevation (z, second row), surface slope ($|\nabla z|$, third row), and surface curvature ($\nabla^2 z$, bottom row) is shown from $t = -2$ to $t = +1$ seconds.

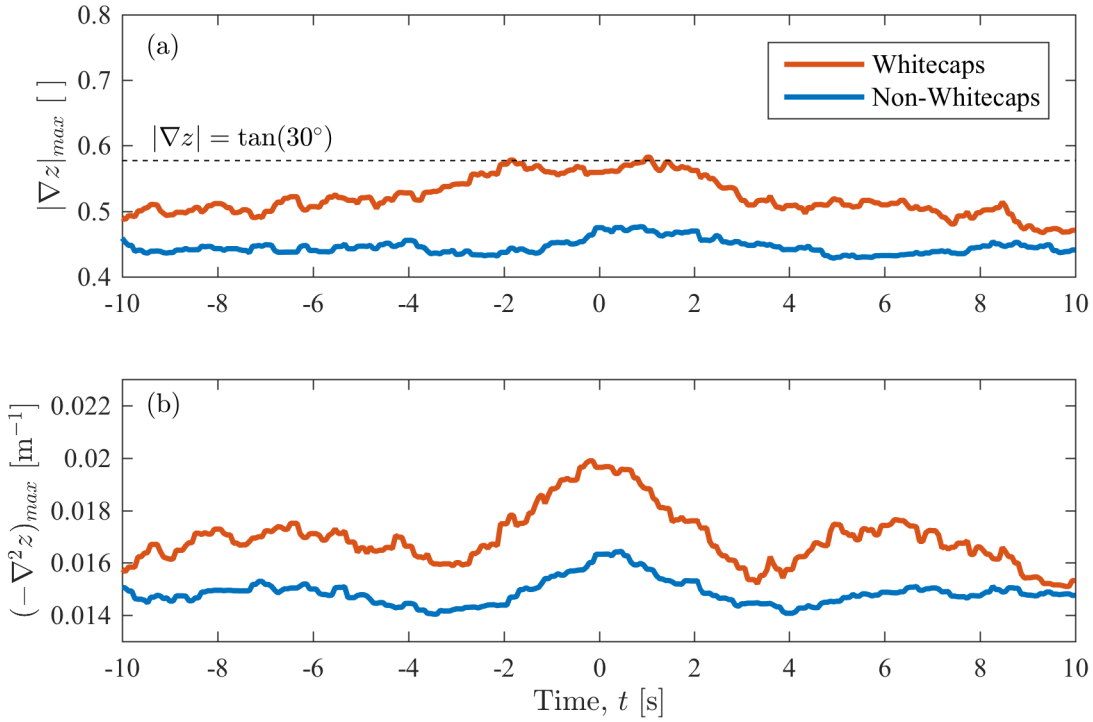

Figure 4.9: Ensemble-averaged time series of (a) maximum surface gradient, $|\nabla z|_{max}$, and (b) maximum negative surface curvature $(-\nabla^2 z)_{max}$, around breaking (orange) and non-breaking (blue) waves.

in $z_{95\%}(t)$ indicates the presence of a prominent wave in the field-of-view. In particular, non-breaking wave events are identified as peaks in $z_{95\%}(t)$ that are one standard deviation above the mean in $z_{95\%}(t)$ and are not within 10 seconds of the breaking events as determined previously. This yields a total of 856 non-breaking waves.

Figure 4.9 shows the ensemble-average time series of the maximum surface slope, $|\nabla z|_{max}$, and negative surface curvature, $(-\nabla^2 z)_{max}$, leading up to and following the peaks in active foam (i.e. whitecaps) and extreme surface height (i.e. non-whitecaps). There is a clear increase in the maximum slope and curvature around the breaking waves, which is not seen in the large, but non-breaking, waves. The time series of $|\nabla z|_{max}$ is particularly interesting. For the breaking waves, the maximum slope is roughly constant within $-2 \leq t \leq 2$ seconds

of the peak of new foam generation, at a value of approximately 0.57. This is very near the slope of $\tan(30°) \approx 0.577$, which is the slope on either side of the 120° corner of a Stokes limiting wave.

The above results suggest that large surface slopes and curvatures are present during whitecapping, however, the details are obscured in the frame-based statistics. What is needed is an algorithm for identifying distinct whitecap events. This is not straightforward, partly because the whitecap foam does not always stay connected through the breaking process, often separating into several groups of pixels. Additionally, although the new whitecap foam is a better proxy for active breaking, the definition of $\Delta W(x, y, t)$ prevents the whitecaps from overlapping between frames. To correct both issues, a topological dilation is applied to the binary $\Delta W(x, y, t)$ array. The dilation step essentially connects all whitecap pixels within 1 meter of each other in the current, preceding, or following frames. Each group of spatially or temporally connected pixels in the dilated $\Delta W(x, y, t)$ is considered as a potential whitecap event. A minimum duration of two seconds is used to avoid transient events (often on the boundary of the field of view) or noise (often from advected residual foam). A somewhat similar procedure for identifying distinct whitecap events in visual imagery was described in Gemmrich et al. (2008).

Next, a box is drawn around each group of whitecap pixels, as shown in Figure 4.10, again for the same example whitecap. One large bounding box (in red) encompasses the most prominent whitecap, which is clearly undergoing active breaking. Smaller whitecaps are detected near to this breaker (orange and blue). It might be argued that these are all a part of the same whitecap, but the distinction will not affect the following analysis. Additionally, a separate whitecap (in yellow, top left in Figure 4.1) is also boxed.

Distributions derived from these bounding boxes show that both surface slopes and curvatures are likely to be high near whitecaps. Figure 4.11a compares the probability density of $|\nabla z|$ and $-\nabla^2 z$ from inside and outside of the boxed whitecap regions. It is clear that within the boxed regions, the distribution of $|\nabla z|$ is skewed high. For example, the ratio of the two functions (Figure 4.11b) shows that values of $|\nabla z| = 0.5$ are approximately 10 times

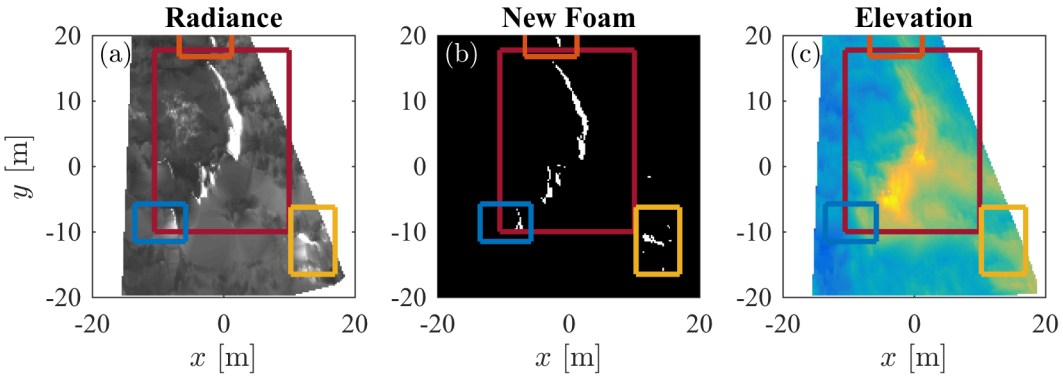

Figure 4.10: The results of the whitecap detection procedure for the whitecap shown in Figures 4.1, 4.2, and 4.8.

more likely to occur in the neighborhood of actively breaking whitecaps. At slopes above 0.55 (not shown), the PDFs converge due to noise contamination, which occurs with equal probability inside and outside of the whitecap boxes. Interestingly, the maximum difference between the breaking and non-breaking distributions occurs very near to the Stokes corner slope of $\tan(30°) = 0.577$.

Similarly, the boxed regions contain a much higher percentage of points of extremely negative curvature (4.11c). The probability ratio peaks around 0.025, where values are 20 times more likely to be found in the boxed whitecap regions. Applying the smoothed discrete Laplacian operator to a long-crested limiting Stokes wave, using the one-term approximation of Rainey and Longuet-Higgins (2006), shows that the maximum of $-\nabla^2 z$ is between 0.022 and 0.029 for waves of length 10–50 meters, which again corresponds with the peak of the anomaly. Again, at the more extreme values (not shown on the plots), random noise brings the distributions back together.

Although less frequent, points of high surface slope and negative curvature do occur in the absence of visible whitecapping. Figure 4.11c compares the histograms of $|\nabla z|$ from within the boxed whitecaps to the overall histogram, to determine what percentage of the extreme values correspond to breaking waves. The ratio of these curves reveals that around

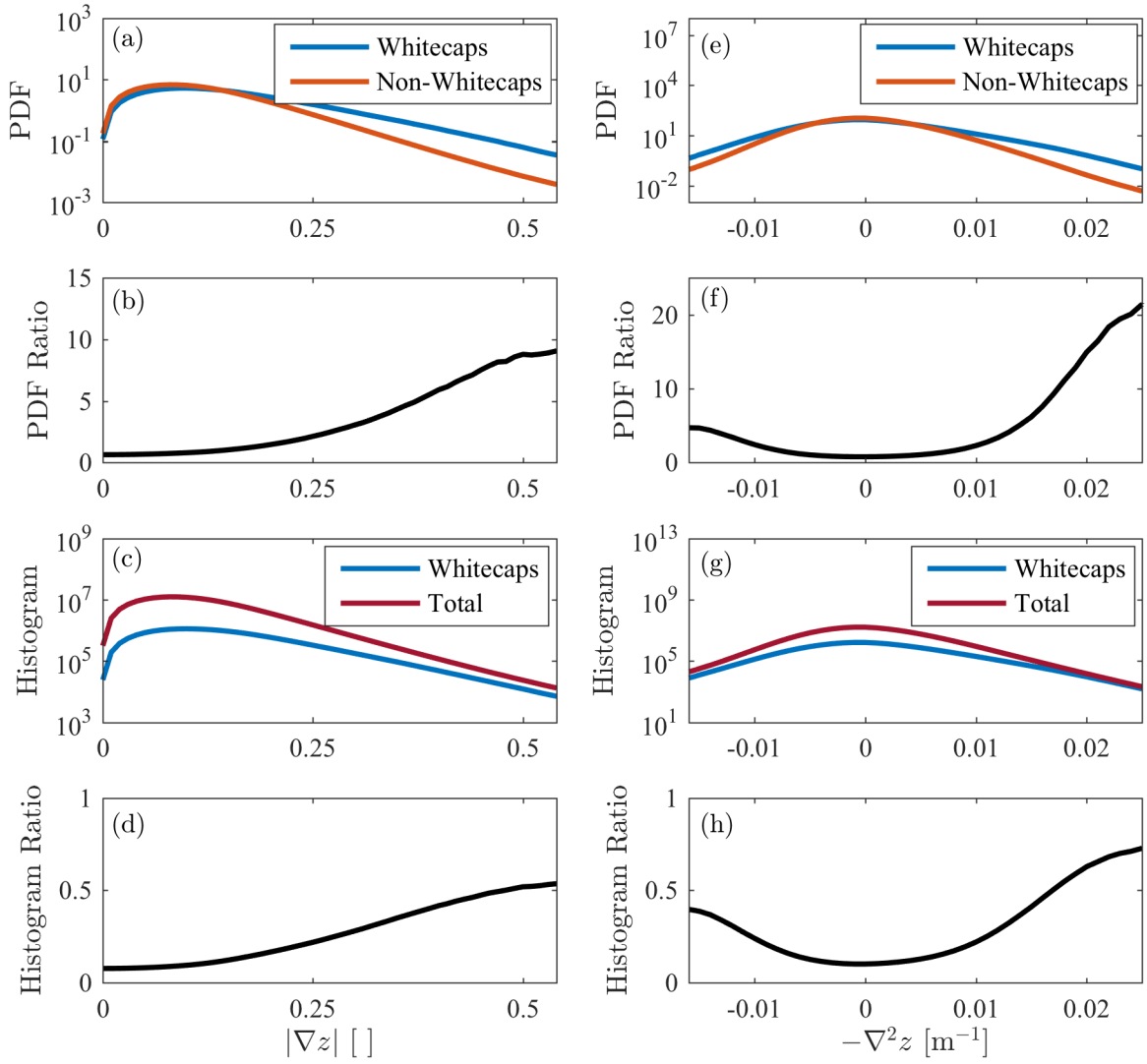

Figure 4.11: Statistics of (a-d) surface gradient magnitude, $|\nabla z|$, and (e-h) surface curvature, $-\nabla^2 z$. Panels (a,e) show the probability density function (PDF) from inside (blue) and outside (orange) of the whitecap boxes, and (b,f) shows their ratio. Panels (c,f) give the overall (red) and whitecap (blue) histograms, with their ratio shown in (d,h).

50% of surface slopes of $|\nabla z| = 0.5$, and 75% of curvatures of $-\nabla^2 z = 0.025$ are associated with whitecaps. Because there is no value which occurs only within the boxes, a threshold on $|\nabla z|$ or $-\nabla^2 z$ cannot be used to predict whitecapping with 100% accuracy. This may be because of noise or missed whitecaps, but it is difficult to know due to the large quantity of data. In the next section, a subset of the breaking cases is more closely examined for further insights into the whitecap geometry.

4.4.3 Breaking Wave Profiles

To further investigate the shape of the whitecaps, the clearest wave-breaking events are selected from the boxed whitecaps as follows. Over the lifetime of each whitecap event, the grouped pixels are approximated by an ellipse with major axis L_{major}, minor axis L_{minor}, centroid x_c and y_c, and orientation θ. The ratio of L_{major} to L_{minor} is found at each time, and the time when this ratio is maximum is recorded as $t_1 = 0$. The best cases are identified as those where the maximum L_{major}/L_{minor} is greater than 4, when θ is within 45° of the wind direction, and the (x_c, y_c) is within 10 meters of the center of the field-of-view. These conditions eliminate cases of noise and advected foam, ensure that the breaking wave is sufficiently long-crested, and avoid breakers occurring near the edge of the field-of-view. Finally, the 137 resulting whitecaps are checked manually to be sure they show unambiguous active breaking, after which 103 examples remain.

Next, a local coordinate system is defined around the breaking crest at $t_1 = 0$, with x_1 and y_1 coordinates orthogonal and parallel to the major axis of the whitecap, respectively. The spatial origin $(x_1, y_1) = (0,0)$ is found as the point of maximum $-\nabla^2 z$, within ± 2.5 meters of the whitecap centroid, (x_c, y_c). Profiles of z are interpolated onto x_1 for $-30 \leq t_1 \leq 30$ seconds.

A Hilbert transform is applied to the wave profiles to calculate the evolution of the whitecap frequency, wavenumber, and amplitude. The Hilbert transform produces an analytic function that defines a local amplitude and phase for the wave signal, $z(x_1, t_1) = \Re\{A(x_1, t_1) \exp[i\phi(x_1, t_1)]\}$. The transform can be performed in space or in time, such

that there are actually two amplitude and two phase functions: $A_x(x_1, t_1)$, $\phi_x(x_1, t_1)$, and $A_t(x_1, t_1)$, $\phi_t(x_1, t_1)$ (see Stansell and MacFarlane, 2002). Differentiating ϕ_x in x_1 gives a local and instantaneous wavenumber, $k(x_1, t_1)$, while differentiating ϕ_t in t_1 gives a local and instantaneous frequency, $\omega(x_1, t_1)$.

Figure 4.12 shows the ensemble-average of the whitecap profiles and Hilbert transform results. All values are normalized, using an average wavenumber, $\overline{k}$, frequency, $\overline{\omega}$, and amplitude, $\overline{A_x}$ or $\overline{A_t}$, from the Hilbert analysis. Since ω, k, A_x, and A_t each vary over the domain, their mean value is somewhat sensitive to the choice of x_1 and t_1 limits. Here, the mean is found between $-10 \leq x_1 \leq 10$ meters and $-3 \leq t_1 \leq 3$ seconds, which encompasses the bulk of the breaking wave but avoids noise near the edge of the domain. These averages were found to agree well with the wave amplitudes and periods from a zero-crossing analysis (not shown). The scaling of the wave elevation is performed after first subtracting the mean surface elevation of the profile, over the same limits.

Analysis of the ensemble-averaged breaking wave profiles is similar to the processing of laboratory wave data. Figure 4.12a shows the wave moving in the positive x_1 direction as time progresses (colors changing from red to blue). The breaker appears very smooth, which is the product of averaging over the 103 individual waves. There is a clear steepening and sharpening of the wave crest, which quickly relaxes after breaking. The maximum in slope occurs very near the breaking crest, but is not symmetric. Initially the maximum slope is on the front face, but after breaking it is on the back side. The wave is also vertically asymmetric. At the break point, the breaker lies almost fully above the mean water line. After breaking, the wave begins to shift to a lower mean elevation. Alternatively, the same information can be presented as a timestack, as in 4.12b. Unfortunately, the limited spatial field-of-view means that the wave is less well-sampled as $x_1\overline{k}$ approaches π and $-\pi$.

Whereas the Hilbert transform of a monochromatic sinusoidal waveform yields a constant amplitude, wavenumber, and frequency, this is not the case for these breaking waves. Instead, there is a localized increase in the wave amplitude, wavenumber, and frequency near the wave crest. Thus, the Hilbert transform results show a rapid increase in local wave steepness as

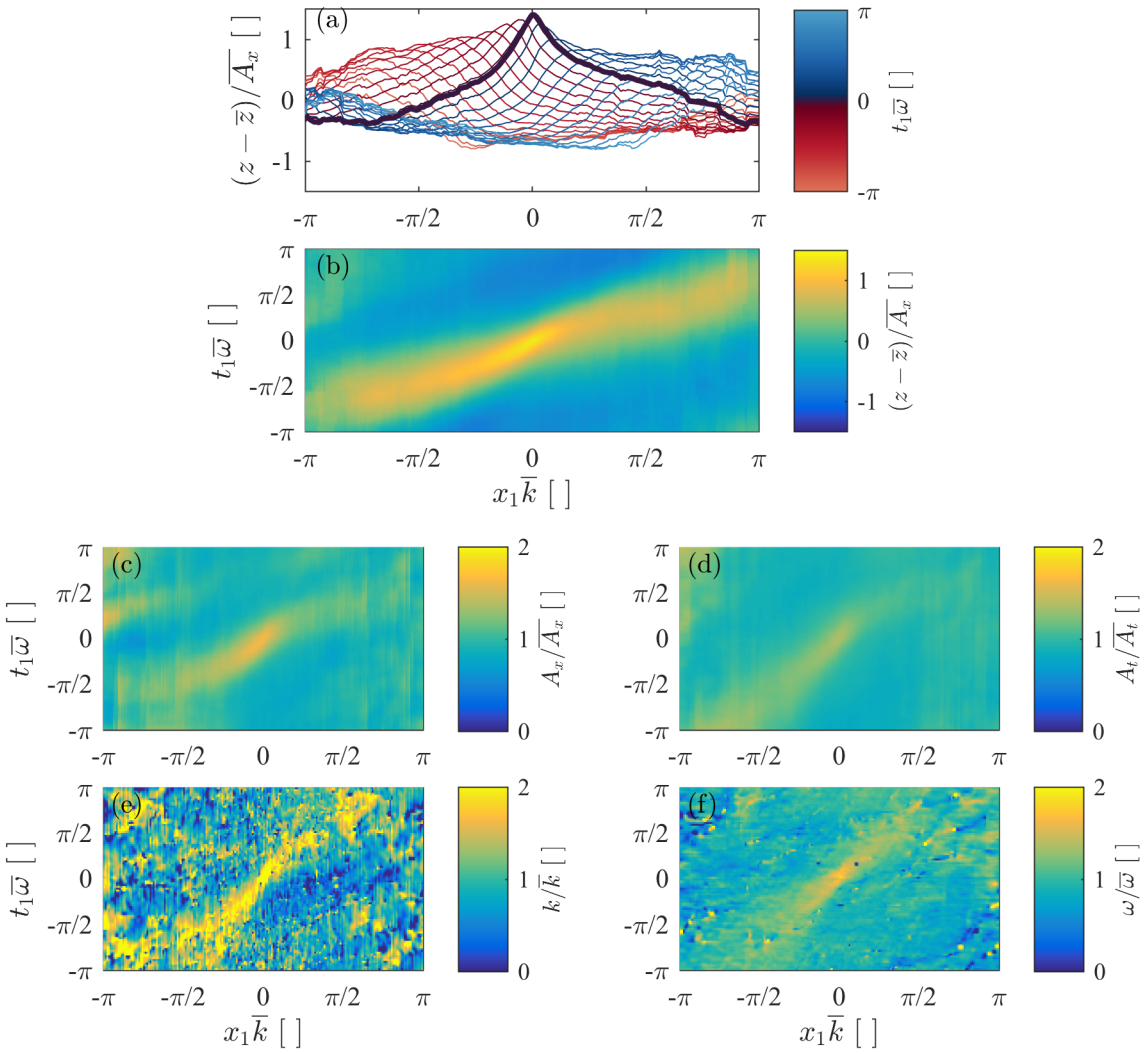

Figure 4.12: Ensemble averages of the 103 whitecap profiles and Hilbert transform results, normalized by the individual mean values over $-10 \leq x_1 \leq 10$ meters and $-3 \leq t_1 \leq 3$ seconds. (a,b) Two views of the elevation profiles, $(z-\overline{z})/\overline{A_x}$, (c) the local spatial amplitude, $A_x/\overline{A_x}$, (d) temporal amplitude, $A_t/\overline{A_t}$, (e) wavenumber $k/\overline{k}$, and (f) frequency, $\omega/\overline{\omega}$. The thick line in (a) corresponds to $t_1 = 0$.

the whitecap occurs. This is shown in Figure 4.13a, where the instantaneous steepness is plotted as $A_x k$. At the break point, $(x_1, t_1) = (0, 0)$, the local steepness is 0.424, very near

the Stokes wave steepness of 0.443.

This local steepening near the breaking crest is shown explicitly in Figure 4.13b. The normalized profiles are shown at $t_1 = 0$, along with the ensemble-average profile, and compared with the Stokes limiting wave, using the one-term approximation from Rainey and Longuet-Higgins (2006). The individual profiles show much scatter, as might be expected in broadband waves, such that the average profile does not quite collapse to the Stokes wave overall. However, near the peak the profiles closely resemble the angular crest of the Stokes wave.

Finally, the propagation speeds of these breaking crests are examined. Banner et al. (2014a) showed that the steepest crests of nonlinear wave groups propagate significantly slower than the predicted linear or weakly nonlinear phase speeds. This behavior is also seen in the whitecap profiles, as shown in Figure 4.14. The true wave phase speeds (c) are calculated as the ratio of the average frequency and wavenumber, which are independently measured from the Hilbert transform. These are compared with the phase speeds calculated from the average frequency using the linear dispersion relation, c_0. Although there is significant scatter, the true phase speeds are almost uniformly less than the linear phase speed. A fit to this data gives $c = 0.61c_0$, consistent with the field measurements of Banner et al. (2014a) showing $c \approx 0.75c_0$. This suggests that these whitecaps formed near the center of nonlinear wave groups.

4.5 Discussion

4.5.1 Comparison with Previous Measurements

Previously, studies such as Holthuijsen and Herbers (1986) have shown oceanic breaking waves to be of similar steepness to their non-breaking counterparts, and much less steep than the Stokes limit. Here, by contrast, Figures 4.9, 4.11, and 4.13 suggest that breaking is associated with high steepness and curvature, and breaking waves do resemble the corner crest of a Stokes limiting wave. The apparent contradiction with previous measurements is in

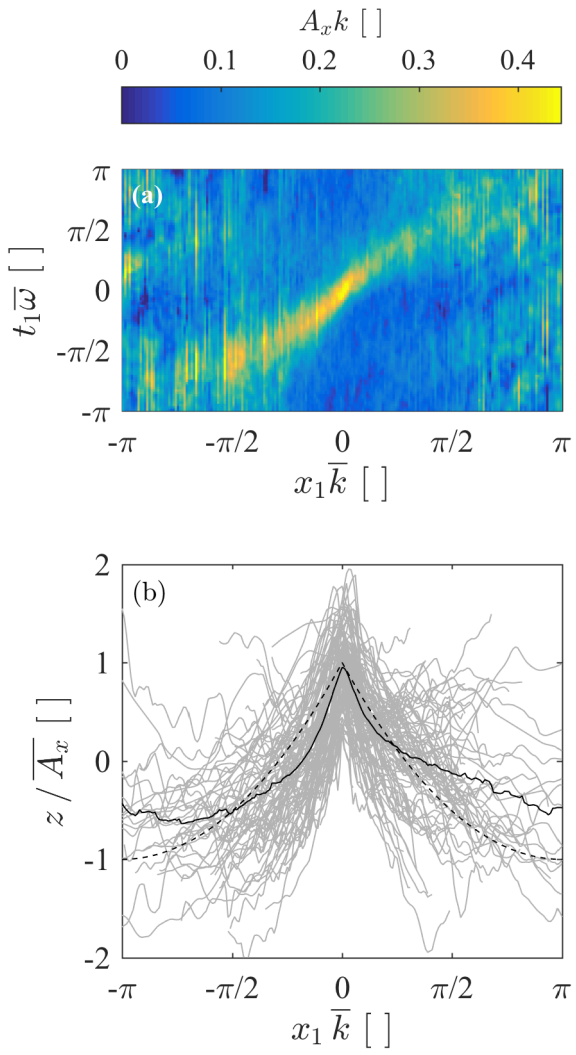

Figure 4.13: (a) Ensemble-averaged local wave steepness, $A_x k$, from the Hilbert transform. (b) Breaking wave profiles, scaled by the average spatial amplitude $\overline{A_x}$, and wavenumber $\overline{k}$ from the Hilbert analysis. The solid line shows the ensemble-averaged profile, dashed line shows the one-term Stokes limiting wave approximation from Rainey and Longuet-Higgins (2006).

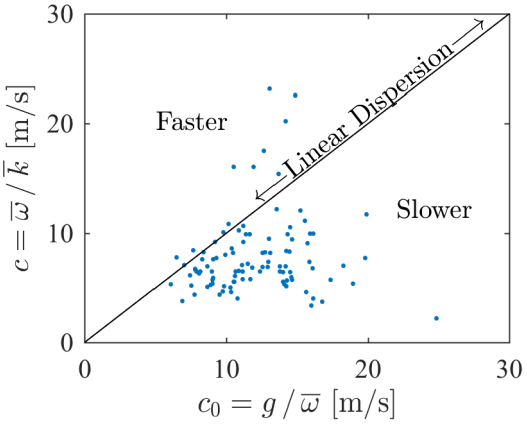

Figure 4.14: Comparison of measured phase speed (c) with linear phase speed (c_0) from the Hilbert transform analysis. The solid line is the 1:1 line, indicating perfect linear dispersion.

part because these steep crests are highly localized, such that they are not often accompanied by the full limiting wave profile. Thus, the whitecaps do not appear particularly steep when examined using bulk measurements of steepness. This is shown explicitly in Figure 4.15, which compares the probability density of wave steepness from the whitecap profiles with the overall steepness distribution, using a weighted average of the curves in Figure 4.7 based on the number of whitecaps from each video burst. This zero-crossing method is taken directly from Holthuijsen and Herbers (1986), and the results are very similar to theirs. Indeed, in a bulk sense, the whitecaps are not considerably steeper than the non-breaking waves.

Furthermore, the steepness measurements from the zero-crossing method of Holthuijsen and Herbers (1986) rely on assuming a wave phase speed from linear dispersion, which Figure 4.14 definitively shows is not applicable. Since the phase speed is actually lower than suggested by linear dispersion, the true bulk steepnesses are higher than the estimates from a time series measured at a point. Specifically, if the phase speed is actually 25% less than the linear expectation, as in Banner et al. (2014a), the true wave steepness is 33% larger

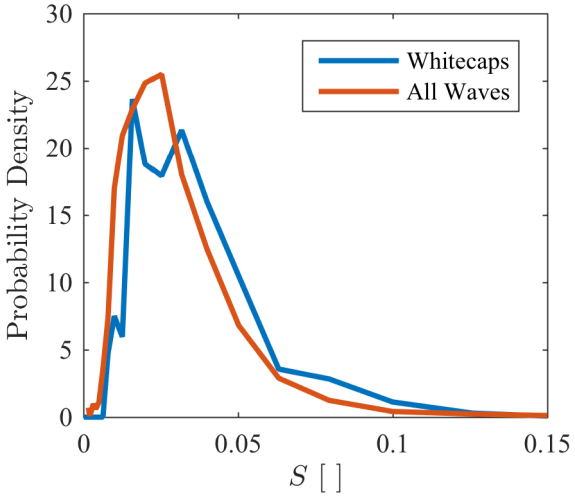

Figure 4.15: Probability density function (PDF) of wave steepness for the breaking wave profiles from a zero-crossing analysis, compared with the overall steepness PDF from a weighted average of the curves in Figure 4.7.

than what is estimated from the time series.

Babanin et al. (2010) suggests that the reason field measurements often show whitecapping at relatively low steepness is that the maximum steepness occurs prior to the detection of whitecap foam. The data do not show evidence of this time delay effect (see Figures 4.9 and 4.12). Still, the point holds — determining the actual onset of breaking in field data is a challenge. The presence of new whitecap foam does indicate active breaking, but the distinction between new foam and residual foam is often unclear. In making two-dimensional profiles of whitecaps, it was found that the surest way to identify active breaking was to use the aspect ratio of the foam patch. Still, manual inspection of these best cases removed roughly 25% of the tagged profiles, which were either ambiguous or mislabeled breaking events. Furthermore, foam from small breaking events often does not show up as brightly as from large events, or even at all in the case of microbreaking waves. The identification of breaking from whitecap foam is therefore one of the largest sources of uncertainty in these observations.

4.5.2 The Role of Nonlinearity

What physical mechanism is responsible for the localized increase in wave steepness in the breaking waves? Babanin (2011) divides potential steepening mechanisms into two categories: instability mechanisms and superposition mechanisms. The Benjamin-Fier instability, more generally called modulational instability, is a nonlinear effect which leads monochromatic wave trains to dissolve into modulating wave groups and can eventually lead to breaking (see the review of Yuen and Lake, 1980). Conversely, superposition mechanisms are primarily linear effects, which produce high steepnesses by focusing two or more wave crests of different directions (directional focusing) or phase speeds (dispersive focusing).

Our measurements indicate that nonlinear group dynamics are critical in producing the necessary steepnesses for breaking to occur. Figures 4.9 and 4.11 show that breaking occurs near points of locally extreme surface slope and curvature. Meanwhile, Figure 4.7 shows that the probability of these extreme surface slopes (at the tail of the distribution) is highly variable, which Liu et al. (1997) attributes to nonlinear effects. Furthermore, the breaking wave profiles display many of the characteristics associated with nonlinear wave groups. For example, the asymmetry of the profiles, in which the wave tilts forward prior to breaking and backwards after, was predicted by the theoretical work of Tayfun (1986). Similarly, the reduced phase speed of the breaking crests, shown in Figure 4.14, is likely due to the nonlinear group dynamics described in Banner et al. (2014a).

By contrast, there is not much evidence for breaking due to superposition. In particular, the wave profiles and their Hilbert transforms do not show steepening from long waves overtaking short waves, as in dispersive focusing. Instead, they show steep nonlinear waves propagating as a phase-locked signal. This matches the hypothesis of Babanin (2011), which argues on probabilistic grounds that dispersive focusing alone cannot produce the amount of breaking measured in natural wavefields.

However, the breaking wave profiles along a principal axis cannot address the question of directional superposition. Figure 4.16 shows again an ensemble-average of the 103 breaking

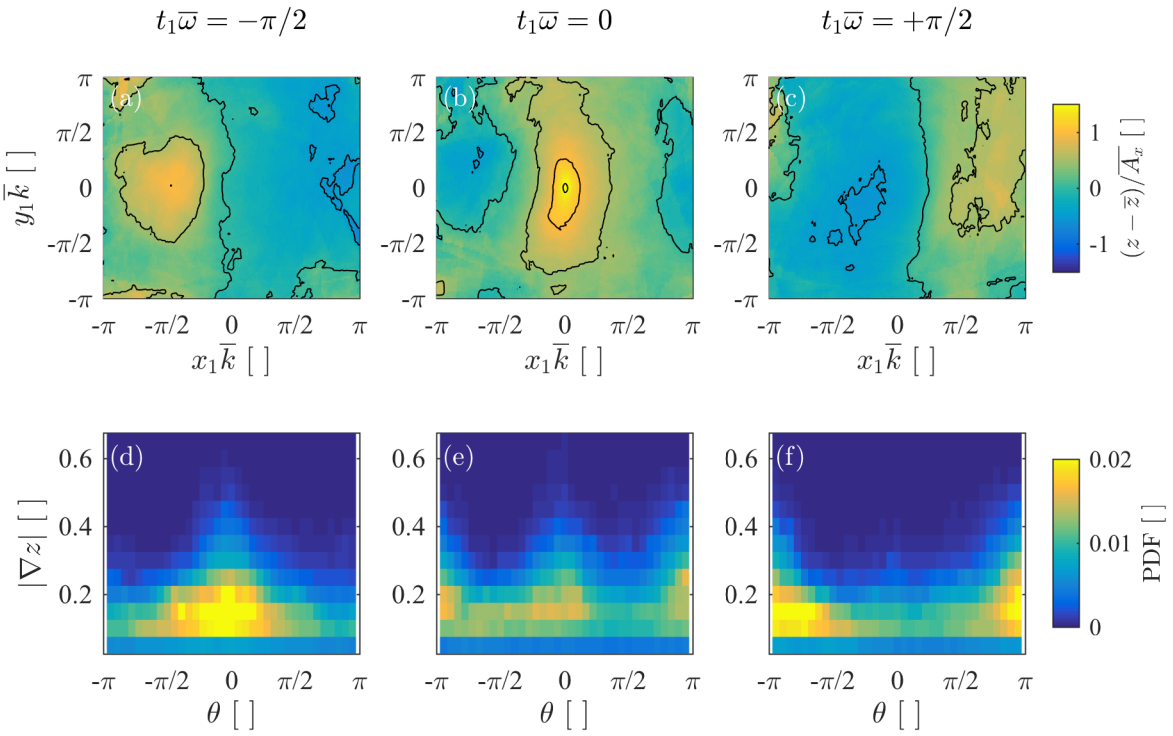

Figure 4.16: Ensemble average of the 103 whitecaps in two dimensions at times (a) $t_1\overline{\omega} = -\pi/2$, (b) $t_1\overline{\omega} = 0$, and (c) $t_1\overline{\omega} = \pi$. As before, all the waves were first normalized by the average wavenumber $\overline{k}$ and amplitude $\overline{A_x}$ from the previous section. (d-f) show the joint probability density function (PDF) of surface gradient magnitude, $|\nabla z|$, and direction, θ, for the whitecaps over the same times. Here, $\theta = 0$ ($\pm\pi$) corresponds to downward slopes in the $+x_1$ ($-x_1$) direction

waves, this time retaining both x_1 and y_1 spatial dimensions. Both x_1 and y_1 are scaled by the average wavenumber, $\overline{k}$, from the previous analysis. Snapshots of the two-dimensional waveform are shown at $t_1\overline{\omega} = -\pi/2$, 0, and π (i.e. at the break point, and a quarter period before and after). In addition, the joint PDF of surface gradient magnitude, $|\nabla z|$, and direction, θ are shown for the same times. Here, $\theta = 0$ corresponds to downward slopes in the $+x_1$ direction, and $\theta = \pm\pi$ indicates downward slopes in the $-x_1$ direction. Due to the limited spatial domain, they are not symmetric before and after breaking, when the wave is entering and leaving the field-of-view.

These plots show no indication of breaking from directional focusing, at least it is not common enough to not be visible in the ensemble averages. Both the wave motion and the direction of the largest surface slopes are primarily in the x_1 direction, which validates the use of the principal axis wave profiles in the previous section. Still, the two-dimensional shape of the average whitecap is interesting, for example, the progression shows the wave spreading somewhat in the y_1 direction during breaking. Moreover, these plots provide further evidence of the highly localized and transient nature of the steep whitecap crests. This three-dimensionality of the breaking crests may be a topic for further research.

4.6 Conclusion

In this chapter, a ship-based stereo video system was used to investigate the steepness of open ocean whitecaps. This work is in many ways complimentary to that of Benetazzo et al. (2016), however our focus on wave breaking is distinct. Additional methodological differences include the use of an IMU-GNSS system to measure the camera positions and orientations, and a checkerboard calibration procedure. Additionally, the stereo processing is primarily performed in Matlab using functions from the Computer Vision Toolbox. As in Benetazzo et al. (2016), the surface elevations are quasi-Gaussian, but whereas Benetazzo et al. (2016) only have model data to compare against their stereo-derived frequency and wavenumber spectra, here good agreement is shown against measured spectra from buoys.

The stereo data provide a unique spatiotemporal measurement of the breaking wave geometries. The measurements reveal that breaking often occurs at steep, highly localized, wave crests. These crests have slope and curvature resembling Stokes (1880) 120° corner, however, the waves themselves have much lower bulk steepness than $H/L = 1/7$. Evidence of local Stokes crests is seen in the time series of frame-wise maximum surface slope and curvature around peaks in new whitecap foam, in the distributions of slope and curvature near detected whitecaps, and in examination of 103 whitecap profiles.

These steep crests were not seen in previous field studies, such as Holthuijsen and Herbers (1986), for two reasons. First, the use of zero-crossing analysis gives only the bulk wave

steepness, rather than a local slope. Second, using a temporal wave trace underestimates the true wave steepness, because of a lower phase speed than predicted by linear dispersion. Thus, a spatial measurement which resolves the local surface steepness is needed to detect the relevant wave steepness. In such measurements, the Hilbert transform is a powerful tool for describing the local and instantaneous wave amplitude, frequency, wavenumber, steepness, and phase speed.

The wave steepening seen in the breaking waves is shown to be primarily due to nonlinear wave group dynamics (as opposed to dispersive or directional superposition). In particular, the phase speed of the breaking crests is consistently slower than predicted by linear dispersion, as discussed in Banner et al. (2014a). Unfortunately, the limited spatial domain prevents direct observation of the group evolution.

Because of its importance for air-sea interaction, a better understanding of wave-breaking is critical for a wide variety of applications. This work shows that stereo video is a powerful tool for studying the surface geometry of breaking waves. As in the numerical simulations of Chalikov and Babanin (2012), our measurements show that whitecaps often form at crests of extreme surface slope and curvature, which are primarily formed by the nonlinear instability mechanisms of modulating wave groups. More work is needed to determine how traditional methods of measuring and describing surface waves (wave buoys, the frequency spectrum, etc.) apply to the breaking waves. In addition, the steep crests are less a predictor of future breaking than an indicator of imminent or active whitecapping. It is possible that a dynamic breaking criteria, as advocated by Song and Banner (2002) and Banner and Pierson (2007), may provide a better framework for predictive models than a geometric criteria alone. Finally, it remains to be seen how whitecap geometry relates to the strength of the breaking (i.e. the whitecap dissipation), but it is likely that stereo video will be a useful tool in this problem as well. Future measurements could test, for example, the dissipation scalings of Duncan (1981) and Drazen et al. (2008).

Chapter 5

CONCLUSIONS

5.1 Summary and Recommendations

In this thesis, ship-based video cameras were used to detect and quantify breaking waves in the open ocean. The overall goal was to relate visible wave-breaking to the general wave conditions, and to investigate the question of why and how waves break in deep water. In Chapter 2 (Schwendeman and Thomson, 2015a), a stabilization method based on the detection of the horizon was found to be useful in removing ship motion from the wave imagery. In Chapter 3 (Schwendeman and Thomson, 2015b), the whitecap coverage was compared with measurements of the wind, waves and turbulent dissipation. Although the wind speed was the best predictor of the whitecap coverage, a normalized mean square slope metric which isolated the steepness of the short-to-intermediate wind waves also performed well. In Chapter 4, stereo video was used to directly measure the geometry of the breaking waves. The whitecaps were characterized by extreme local steepness near the breaking crests, which were geometrically similar to Stokes' 120° limiting corner flow. Several implications of this work are further examined below.

One difficulty in making quantitative use of single camera imagery in the open ocean is ship motion. The horizon stabilization and georectification method of Chapter 2 showed that measurements can be made without additional instrumentation, such as active stabilization or inertial motion packages. The horizon method is both robust and accurate. In determining the camera pitch and roll, this algorithm may be useful for other applications as well. For example, in Chapter 4 the horizon-derived roll was used to synchronize the stereo imagery with the IMU data stream. In making ship-based video measurements, one should always consider keeping the horizon in the camera field-of-view as a check on the motion correction.

Unfortunately, the horizon method cannot correct for ship heave and heading.

The analysis of whitecap coverage in Chapter 3 challenged several ideas of open ocean whitecapping. Although most steepness metrics are indeed correlated with W, the quality of these fits is highly variable, and many are not nearly as good as a simple function of wind speed. The best agreement is with mean square slope variables calculated in the tail of the wave spectrum. These parameters avoid the influence of swell energy on the steepness, which appears to have little effect on the whitecap coverage. Moreover, the improvement in correlation after normalizing by directional spread indicates that wave directionality needs to be taken into account. Measurements from stereo video may be able to further improve the comparison of whitecap coverage and wave slope. Since whitecaps occur near extremes in the surface slope, the probability of these extreme slopes may be a better predictor of the whitecap coverage than spectral steepness metrics taken from a buoy. The probability density function of the surface gradient shown in Chapter 4 indicate that extremes in the surface slope are related to both the average wave steepness as well as the wave nonlinearity.

Comparing W among only studies using similar methodology (especially digital imagery and pixelwise thresholding), and limiting the comparison to the intermediate wind speeds in which the measurements were made, the supposed scatter in the fits to U_{10} is much reduced. Wind speed is an imperfect parameter to physically explain the whitecap coverage, but it has good predictive power because it is a more precise measurement than most wave variables. Modelers should be skeptical about replacing wind speed parameterizations of whitecapping with more complicated ones based on wave quantities unless there is strong evidence of improved performance. Using bulk parameters, especially those defined at the spectral peak, is particularly unadvisable. Most recent measurements do, however, show clear evidence of a wind speed threshold in W, which is not captured in the power law fits such as Monahan and O'Muircheartaigh (1980). After more than 30 years, it may be time to replace Monahan and O'Muircheartaigh (1980) with a more up-to-date version as the *de facto* standard. The Callaghan et al. (2008a) relation would be a good choice, based on their large amount of data and range of observed wind conditions. However, whereas they provide a piecewise fit using

two cubic functions, a single "threshold power law" function, as described in Schwendeman and Thomson (2015b), would likely also fit the full dataset well and be simpler to implement.

Although $\Lambda(c)$ is a more complex measurement than W, it is not clear that it provides much more meaningful information. All of the uncertainties in determining W are also included in $\Lambda(c)$, with the additionally difficulty of determining the breaker speed, c. Not only is the measurement of c challenging, but the theoretical definition is ambiguous as well (see Banner et al., 2014b). The relatively poor comparison of W with turbulent dissipation rate is related to the difficulty in determining a common breaking strength, b. Microbreaking may explain some of the scatter, or it may come mostly from uncertainty in the measurements, but it is difficult to know because S_{ds} is so poorly constrained. Validation of the Duncan (1981) or Drazen et al. (2008) scalings from phase-resolved measurements of breaking in the open ocean are likely needed for $\Lambda(c)$ to gain further acceptance within the scientific community.

In Chapter 4, ship-based stereo video wave measurements were shown to be of similar quality to buoy measurements, while providing much more information. With the implementation of robust stereo algorithms in Matlab, as well as ever improving open source libraries and toolboxes, stereo video is quickly becoming a more widely available tool for wave scientists. Apart from wave breaking, there are many problems which may benefit from stereo video measurements, such as wave-ice and wave-current interactions. It may also have application in wave monitoring or extreme wave detection.

Stereo video processing leads to phase-resolved, three-dimensional, measurements of whitecaps, which were used to track the temporal and spatial evolution of the breaking wave steepness. This capability is unique from older field studies, such as Holthuijsen and Herbers (1986), which were only able to measure wave-breaking at one point. From a point measurement, one is forced to define the wave steepness over a full wavelength, which is problematic in a spectral wave environment where it is difficult to define a single wave. Moreover, the point measurements are not able to differentiate between different stages of breaking, so they may not measure the maximum wave steepness before breaking onset. Even in the

stereo data, defining the breaking onset can be a challenge. Unlike Holthuijsen and Herbers (1986), the stereo data indicate that, with steepness defined as the maximum of local surface slope, the whitecaps are significantly steeper than the non-breaking waves. Furthermore, the highest surface slopes are approximately consistent with the angle of the Stokes limiting wave, and mostly occur near to the whitecaps.

5.2 Remaining Questions

Generally, this work has attempted to give insight into three overarching questions regarding breaking waves, namely

1. What causes a wave to break?

2. Given a wave spectrum, which waves (and how many) will break?

3. How much energy is dissipated due to breaking, both individually and collectively?

These questions are quite broad and may not be fully settled for many years. In the meantime, there are many more specific questions to investigate. Below are listed some of the questions raised over the course of this work:

- The majority of whitecap observations have been made in intermediate wind speeds. How does wave breaking change in higher winds, for example, during a hurricane?

- What can be done about the issue of microbreaking? Infrared measurements remain expensive and difficult to interpret, is there another way to detect them or quantify their effects? Do microbreakers follow the same dynamics as visible whitecaps, or must they be treated differently?

- The stereo measurements show little lead time between the maximum wave steepness and the onset of breaking. Is there a way to forecast breaking several seconds, or even

several wave periods, in advance? Alternatively, is it possible that there is no simple, universal, breaking criteria?

- Does the breaking onset and resulting dissipation depend on whether breaking was caused by modulational instability vs. linear superposition? More generally, what effect do nonlinear group dynamics have on the breaking?

- Do either the Duncan (1981) or Drazen et al. (2008) scaling of dissipation rate apply to oceanic whitecaps? Can the whitecap area-time integral be used to determine the loss of wave energy, as suggested in personal communication with Adrian Callaghan?

- Even if the total loss of energy from a whitecap is known, the wave models need the spectral distribution of dissipation. Does $\Lambda(c)$ correctly partition this dissipation?

- How much of the energy lost during breaking goes into turbulence, as opposed to other dissipative mechanisms like bubble production? Conversely, can turbulence interact with non-breaking waves to dissipate wave energy?

5.3 Next Steps

Clearly, there is much left to learn. Stereo video shows great promise for studying whitecaps, and is likely to soon become a more widely used tool. The stereo video data of Chapter 4 may yet provide more insight into the breaking wave dynamics. For example, there is much interest in statistical analysis and predictions of extreme wave events (i.e. "rogue waves") from stereo video (see Benetazzo et al., 2015). To benefit other scientists interested in such "space-time" wave data, the current dataset will be archived and made available for public download. Additionally, the same stereo system has since been deployed in the marginal ice zone to study the influence of sea ice on waves, and may be useful in other unique environments.

However, it is clear that to investigate wave-breaking further, especially breaking dissipation and wave group dynamics, a larger field-of-view would be valuable. Unfortunately, it is difficult to expand the spatial domain while maintaining the accuracy of the stereo measurement. Some gains might be seen from using higher resolution cameras or simply more cameras. Alternatively, one might attempt to change the frame of reference by driving a ship at roughly the wave group velocity, thereby observing each wave group for a longer period of time. It might be possible to use unmanned aircraft to get a more ideal viewpoint. Another option is to use LIDAR to measure the surface elevation. Because of the high resolution of modern scanning LIDAR, it is possible to accurately measure the waves from manned aircraft, as in Romero and Melville (2010). Finally, it may be useful for some questions to start from a simpler measurement site, with a much narrower wave spectrum in both frequency and direction. This may clarify the basic dynamics, without the added complications of multiple wave scales.

The statistics of visible whitecaps remain valuable for relating wave-breaking to air-sea interaction and mixing, yet there are still relatively few comprehensive datasets. With the current price of video cameras and computer storage, and the horizon rectification method, it is now minimally expensive to measure whitecap coverage from cruises of opportunity. With a good system and some help, there is little reason why whitecap coverage cannot be measured, for example, on every UNOLS cruise, which would likely cover most wave conditions (perhaps not hurricanes and other extreme events). This would aid in the effort of researchers currently using satellite data products to estimate the global whitecap coverage (see Anguelova and Webster, 2006). It would also show once and for all whether water properties effect the whitecap coverage, as discussed in Callaghan et al. (2008b).

Still, many of the questions in the previous section cannot be answered without new and innovative methodologies. For example, in the age of "big data," the time is ripe for a new framework for quantifying wave breaking from video. This framework should be designed with microbreaking in mind, meaning IR cameras are probably necessary. Ideally, it should avoid the uncertainty from identifying discrete breaking events, as in whitecap coverage or

the Fourier method of Thomson and Jessup (2009). The most simple variant would be an infrared "whitecap coverage," though even this would introduce a number of new challenges. For example, the IR signal is highly dependent on the properties of the surface "cool-skin" layer (see Jessup et al., 1997). On the other hand, given the rapid progress in machine learning algorithms, it may be that more information can be obtained from these images with less direction from the user.

BIBLIOGRAPHY

Y. C. Agrawal, E. A. Terray, and M.A. Donelan. Enhanced dissipation of kinetic energy beneath surface waves. *Nature*, 359:219–220, 1992.

M. D. Anguelova and F. Webster. Whitecap coverage from satellite measurements: A first step toward modeling the variability of oceanic whitecaps. *J. Geophys. Res.*, 111(C03017), 2006. doi: 10.1029/2005JC003158.

F. Ardhuin, E. Rogers, A. V. Babanin, J. Filipot, R. Magne, A. Roland, A. van der Westhuysen, P. Queffeulou, J. Lefevre, L. Aouf, and F. Collard. Semiempirical dissipation source functions for ocean waves. part i: Definition, calibration, and validation. *J. Phys. Oceanogr.*, 40(9):1917–1941, 2010.

A. Babanin, D. Chalikov, I. Young, and I. Savelyev. Predicting the breaking onset of surface water waves. *Geophys. Res. Let.*, 34:L07605, 2007. doi: 10.1029/2006GL029135.

A. V. Babanin. *Breaking and Dissipation of Ocean Surface Waves*. Cambridge Univ. Press, New York, 2011.

A. V. Babanin, D. Chalikov, I. R. Young, and I. Savelyev. Numerical and laboratory investigation of breaking of steep two-dimensional waves in deep water. *J. Fluid Mech.*, 644: 433–463, 2010.

M. Banner and X. Tian. On the determination of the onset of breaking for modulating surface gravity water waves. *J. Fluid Mech.*, 367:107–137, 1998. doi: 10.1017/S0022112098001517.

M. L. Banner. Equilibrium spectra of wind waves. *J. Phys. Oceanogr.*, 20:966–984, 1990.

M. L. Banner and O. M. Phillips. On the incipient breaking of small scale waves. *J. Fluid Mech.*, 64:647–656, 1974.

M. L. Banner and W. L. Pierson. Wave breaking onset and strength for two-dimensional deep water wave groups. *J. Fluid Mech.*, 585:93–115, 2007.

M. L. Banner, A. V. Babanin, and I.R. Young. Breaking probability for dominant waves on the sea surface. *J. Phys. Oceanogr.*, 30:3145–3160, 2000. doi: 10.1175/1520-0485(2000)030<3145:BPFDWO>2.0.CO;2.

M. L. Banner, J. R. Gemmrich, and D.M. Farmer. Multiscale measurements of ocean wave breaking probability. *J. Phys. Oceanogr.*, 32:3364–3375, 2002. doi: 10.1175/1520-0485(2002)032<3364:MMOOWB>2.0.CO;2.

M. L. Banner, X. Barthelemy, F. Fedele, M. Allis, A. Benetazzo, F. Dias, and W. L. Pierson. Linking reduced breaking crest speeds to unsteady nonlinear water wave group behavior. *Physical Review Letters*, 112(114502), 2014a.

M. L. Banner, C. J. Zappa, and J. R. Gemmrich. A note on the phillips spectral framework for ocean whitecaps. *J. Phys. Ocean.*, 44:1727–1734, 2014b. doi: 10.1175/JPO-D-13-0126.1.

G. Bao, S. Xiong, and Z. Zhou. Instrumentation and measurement, ieee transactions on. *Vision-based horizon extraction for micro air vehicle flight control*, 54(3):1067–1072, 2005.

A. Benetazzo. Measurements of short water waves using stereo matched image sequences. *Coastal Engineering*, 53:1013–1032, 2006.

A. Benetazzo, F. Fedele, G. Gallego, P.-C. Shih, and A. Yezzi. Offshore stereo measurements of gravity waves. *Coastal Engineering*, 64:127–138, 2012.

A. Benetazzo, F. Barbariol, F. Bergamasco, A. Torsello, S. Carniel, and M. Sclavo. Observation of extreme sea waves in a space-time ensemble. *J. Phys. Ocean.*, 45:2261–2275, 2015. doi: 10.1175/JPO-D-15-0017.1.

A. Benetazzo, F. Barbariol, F. Bergamasco, A. Torsello, S. Carniel, and M. Sclavo. Stereo wave imaging from moving vessels: Practical use and applications. *Coastal Engineering*, 109:114–127, 2016. doi: 10.1016/j.coastaleng.2015.12.008.

C. F. Bohren and A. B. Fraser. At what altitude does the horizon cease to be visible? *American Journal of Physics*, 54:222–227, 1986.

M. G. Brown and A. Jensen. Experiments on focusing unidirectional water waves. *J. Geophys. Res.*, 106(C8):16917–16928, 2001. doi: 10.1029/2000JC000584.

A. Callaghan, G. de Leeuw, L. Cohen, and C. D. O'Dowd. Relationship of oceanic whitecap coverage to wind speed and wind history. *Geophysical Research Letters*, 35(L23609), 2008a. doi: 10.1029/2008GL036165.

A. H. Callaghan. An improved whitecap timescale for sea spray aerosol production flux modeling using the discrete whitecap method. *J. Geophys. Res.*, 118:9997–10010, 2013. doi: 10.1002/jgrd.50768.

A. H. Callaghan and M. White. Automated processing of sea surface images for the determination of whitecap coverage. *J. Atmos. Ocean. Tech.*, 26:383–394, 2009. doi: 10.1175/2008JTECHO634.1.

A. H. Callaghan, G. B. Deane, and M. D. Stokes. Observed physical and environmental causes of scatter in whitecap coverage values in a fetch-limited coastal zone. *J. Geophys. Res.*, 113(C05022), 2008b. doi: 10.1029/2007JC004453.

A. H. Callaghan, G. B. Deane, and M. D. Stokes. Two regimes of laboratory whitecap foam decay: bubble-plume controlled and surfactant stabilized. *J. Phys. Ocean.*, 43:1114–1126, 2013. doi: 10.1175/JPO-D-12-0148.1.

J. Canny. A computational approach to edge detection. *IEEE Transactions on Pattern Analysis and Machine Intelligence*, PAMI-8(6):679–698, 1986.

H. Cao and J. Zhang. Video stabilizing and tracking by horizontal line for maritime cruise ship. In *Control and Automation, 2007. ICCA 2007. IEEE International Conference on*, pages 1202–1206, May 2007.

V. J. Cardone. Specification of the wind distribution in the marine boundary layer for wave forecasting. Technical report, New York University, 1970.

L. Cavaleri, J.-H.G.M. Alves, F. Ardhuin, A. Babanin, M. Banner, K. Belibassakis, M. Benoit, M. Donelan, J. Groeneweg, T.H.C. Herbers, P. Hwang, P.A.E.M. Janssen, T. Janssen, I.V. Lavrenov, R. Magne, J. Monbaliu, M. Onorato, V. Polnikov, D. Resio, W.E. Rogers, A. Sheremet, J. McKee Smith, H.L. Tolman, G. van Vledder, J. Wolf, and I. Young. Wave modelling – the state of the art. *Progress in Oceanography*, 75(4):603 – 674, 2007. doi: 10.1016/j.pocean.2007.05.005.

L. Cavaleri, B. Fox-Kemper, and M. Hemer. Wind waves in the coupled climate system. *Bull. Amer. Meteor. Soc.*, 93:1651–1661, 2012. doi: 10.1175/BAMS-D-11-00170.1.

D. Chalikov. Statistical properties of nonlinear one-dimensional wave fields. *Nonlinear Processes in Geophysics*, 12(5):671–689, 2005. doi: 10.5194/npg-12-671-2005.

D. Chalikov and A. V. Babanin. Simulation of wave breaking in one-dimensional spectral environment. *J. Phys. Ocean.*, 42:1745–1761, 2012. doi: http://dx.doi.org/10.1175/JPO-D-11-0128.1.

C. C. Chickadel, R. A. Holman, and M. H. Freilich. An optical technique for the measurement of longshore currents. *Journal of Geophysical Research*, 108(C11):1–17, 2003.

C. Cox and W. Munk. Measurement of the roughness of the sea surface from photographs of the sun's glitter. *J. Opt. Soc. Am.*, 44:838–850, 1954. doi: 10.1364/JOSA.44.000838.

P. D. Craig and M. L. Banner. Modeling wave-enhanced turbulence in the ocean surface layer. *J. Phys. Ocean.*, 24:2546–2559, 1994. doi: 10.1175/1520-0485(1994)024<2546:MWETIT>2.0.CO;2.

G. de Leeuw, E. L. Andreas, M. D. Anguelova, C. W. Fairall, E. R. Lewis, C. O'Dowd, M. Schulz, and S. E. Schwartz. Production flux of sea spray aerosol. *Rev. Geophys.*, 49 (RG2001), 2011. doi: 10.1029/2010RG000349.

J. J. de Vries. *Datawell waverider reference manual, DWR-MkIII, DWR-G*. Datawell BV oceanographic instruments, 2014.

S. de Vries, D. F. Hill, M. A. de Schipper, and M. J. F. Stive. Remote sensing of surf zone waves using stereo imaging. *Coastal Engineering*, 58:239–250, 2011.

T. Dickey, M. Lewis, and G. Chang. Optical oceanography: Recent advances and future directions using global remote sensing and in situ observations. *Reviews of Geophysics*, 44 (RG1001), 2006.

D.A. Drazen, W. K. Melville, and L. Lenain. Inertial scaling of dissipation in unsteady breaking waves. *J. Fluid Mech.*, 611:307–332, 2008. doi: 10.1017/S0022112008002826.

R. O. Duda and P. E. Hart. Use of the hough transformation to detect lines and curves in pictures. *Commun. ACM*, 15(1):11–15, 1972.

J. H. Duncan. An experimental investigation of breaking waves produced by a towed hydrofoil. *Proc. R. Soc. London Ser. A*, 377:331–348, 1981. doi: 10.1098/rspa.1981.0127.

J.B. Edson, C.W. Fairall, P.G. Mestayer, and S.E. Larsen. A study of the inertial-dissipation method for computing air-sea fluxes. *J. Geophys. Res.*, 96(C6):10689–10711, 1991. doi: 10.1029/91JC00886.

F. Fedele, A. Benetazzo, G. Gallego, P-C Shih, A. Yezzi, F. Barbariol, and F. Ardhuin. Space-time measurements of oceanic sea states. *Ocean Modelling*, 70:103–115, 2013. doi: 10.1016/j.ocemod.2013.01.001.

S. Fefilatyev, D. Goldgof, M. Shreve, and C. Lembke. Detection and tracking of ships in

open sea with rapidly moving buoy-mounted camera system. *Ocean Engineering*, 54:1–12, 2012.

G. Z. Forristall. Wave crest distributions: Observations and second-order theory. *J. Phys. Ocean.*, 30:1931–1943, 2000. doi: 10.1175/1520-0485(2000)030<1931:WCDOAS>2.0.CO;2.

A. P. French. How far away is the horizon? *American Journal of Physics*, 50:795–799, 1982.

G. Gallego, A. Yezzi, F. Fedele, and A. Benetazzo. A variational stereo method for the three-dimensional reconstruction of ocean waves. *IEEE Trans. on Geoscience and Remote Sensing*, 49(11):4445–4457, 2011.

J. R. Garratt. Review of drag coefficients over oceans and continents. *Mon. Wea. Rev.*, 105: 919–929, 1977. doi: 10.1175/1520-0493(1977)105<0915:RODCOO>2.0.CO;2.

J. Gemmrich. Strong turbulence in the wave crest region. *J. Phys. Oceanogr.*, 40:583–595, 2010. doi: 10.1175/2009JPO4179.1.

J. Gemmrich, C. J. Zappa, M. L. Banner, and R. P. Morison. Wave breaking in developing and mature seas. *J. Geophys. Res.*, 118:4542–4552, 2013. doi: 10.1002/jgrc.20334.

J. R. Gemmrich and D. Farmer. Observations of the scale and occurrence of breaking surface waves. *J. Phys. Oceanogr.*, 29:2595–2606, 1999.

J. R. Gemmrich and D. Farmer. Near-surface turbulence in the presence of breaking waves. *J. Phys. Ocean.*, 34:1067–1086, 2004.

J. R. Gemmrich, M. L. Banner, and C. Garrett. Spectrally resolved energy dissipation rate and momentum flux of breaking waves. *J. Phys. Oceanogr.*, 38:1296–1312, 2008. doi: 10.1175/2007JPO3762.1.

L. Goddijn-Murphy, D. K. Woolf, and A. H. Callaghan. Parameterizations and algorithms for oceanic whitecap coverage. *J. Phys. Ocean.*, 41:742–756, 2011. doi: 10.1175/2010JPO4533.1.

J. L. Hanson and O. M. Phillips. Wind sea growth and dissipation in the open ocean. *J. Phys. Ocean.*, 29:1633–1648, 1999. doi: 10.1175/1520-0485(1999)029<1633:WSGADI>2.0.CO;2.

K. Hasselmann. On the spectral dissipation of ocean waves due to white capping. *Boundary-Layer Meteorology*, 6:107–127, 1974. doi: 10.1007/BF00232479.

J. Heikkila and O. Silven. A four-step camera calibration procedure with implicit image correction. *IEEE Computer Society Conference on Computer Vision and Pattern Recognition*, 1997.

H. Hirschmuller. Stereo processing by semiglobal matching and mutual information. *IEEE Transactions on Pattern Analysis and Machine Intelligence*, 30(2):328–341, 2008. doi: 10.1109/TPAMI.2007.1166.

K. Todd Holland, Robert A. Holman, Thomas C. Lippmann, John Stanley, and Nathaniel Plant. Practical use of video imagery in nearshore oceanographic field studies. *IEEE Journal of Oceanic Engineering*, 22:81–92, 1997.

R. Holman and M. C. Haller. Remote sensing of the nearshore. *Annual Review of Marine Science*, 5:95–113, 2013.

L. H. Holthuijsen. Stereophotography of ocean waves. *Applied Ocean Research*, 5(4):204–209, 1983. doi: 10.1016/0141-1187(83)90034-2.

L. H. Holthuijsen and T. H. C. Herbers. Statistics of breaking waves observed as whitecaps in the open sea. *Journal of Physical Oceanography*, 16(2):290–297, 2016/01/27 1986. doi: 10.1175/1520-0485(1986)016¡0290:SOBWOA¿2.0.CO;2. URL http://dx.doi.org/10.1175/1520-0485(1986)016<0290:SOBWOA>2.0.CO;2.

P. A. Hwang and M. A. Sletten. Energy dissipation of wind-generated waves and whitecap coverage. *J. Geophys. Res.*, 113(C02012), 2008. doi: 10.1029/2007JC004277.

P. A. Hwang, J. V. Toporkov, M. A. Sletten, and S. P. Menk. Mapping surface currents and waves with interferometric synthetic aperture radar in coastal waters: observations of wave breaking in swell-dominant conditions. *J. Phys. Ocean.*, 43:563–582, 2013. doi: 10.1175/JPO-D-12-0128.1.

J. Illingworth and J. Kittler. A survey of the hough transform. *Computer Vision, Graphics, and Image Processing*, 44:87–116, 1988.

IOCCG. Remote sensing of ocean colour in coastal, and other optically-complex, waters. In S. Sathyendranath, editor, *Reports of the International Ocean-Colour Coordinating Group*, number 3, Dartmouth, Canada, 2000. IOCCG.

B. Jähne, J. Klinke, and S. Waas. Imaging of short ocean wind waves: a critical theoretical review. *J. Opt. Soc. Am. A*, 11(8):2197–2209, 1994. doi: 10.1364/JOSAA.11.002197.

A. Jessup and K. Phadnis. Measurement of the geometric and kinematic properties of microscale breaking waves from infrared imagery using a PIV algorithm. *Measur. Sci. Tech.*, 16:1961–1969, 2005.

A. Jessup, C. Zappa, and M. Loewen. Infrared remote sensing of breaking waves. *Nature*, 385:52–55, 1997.

K. K. Kahma and C. J. Calkoen. Reconciling discrepancies in the observed growth of wind-generated waves. *J. Phys. Ocean.*, 22:1389–1405, 1992. doi: 10.1175/1520-0485(1992)022<1389:RDITOG>2.0.CO;2.

J. M. Kleiss and W. K. Melville. Observations of wave breaking kinematics in fetch-limited seas. *J. Phys. Ocean.*, 40:2575–2604, 2010. doi: 10.1175/2010JPO4383.1.

J. M. Kleiss and W. K. Melville. The analysis of sea surface imagery for whitecap kinematics. *J. Atmos. Ocean. Tech.*, 28:219–243, 2011. doi: 10.1175/2010JTECHO744.1.

C. Kraan, W. A. Oost, and P. A. E. M. Janssen. Wave energy dissipation by whitecaps. *J. Atmos. Ocean. Tech.*, 13:262–267, 1996. doi: 10.1175/1520-0426(1996)013<0262:WEDBW>2.0.CO;2.

C. Lafon, J. Piazzola, P. Forget, and S. Despiau. Whitecap coverage in coastal environment for steady and unsteady wave field conditions. *Journal of Marine Systems*, 66:38–46, 2007. doi: http://dx.doi.org/10.1175/1520-0426(1996)013<0262:WEDBW>2.0.CO;2.

E. Lamarre and W. K. Melville. Air entrainment and dissipation in breaking waves. *Nature*, 351:469–472, 1991. doi: 10.1038/351469a0.

F. Leckler, F. Ardhuin, C. Peureux, A. Benetazzo, F. Bergamasco, and V. Dulov. Analysis and interpretation of frequency-wavenumber spectra of young wind waves. *J. Phys. Ocean.*, 45:2484–2496, 2015. doi: 10.1175/JPO-D-14-0237.1.

Y. Liu, X.-H. Yan, W. T. Liu, and P. A. Hwang. The probability density function of ocean surface slopes and its effects on radar backscatter. *J. Phys. Ocean.*, 27:782–797, 1997. doi: 10.1175/1520-0485(1997)027<0782:TPDFOO>2.0.CO;2.

M. S. Longuet-Higgins. The effect of non-linearities on statistical distributions in the theory of sea waves. *J. Fluid Mech.*, 17(3):459–480, 1963. doi: 10.1017/S0022112063001452.

W. K. Melville. Energy dissipation by breaking waves. *J. Phys. Oceanogr.*, 24:2041–2049, 1994.

W. K. Melville. The role of surface-wave breaking in air-sea interaction. *Annu. Rev. Fluid Mech.*, 28:279–321, 1996. doi: 10.1146/annurev.fl.28.010196.001431.

W. K. Melville and P. Matusov. Distribution of breaking waves at the ocean surface. *Nature*, 417:58–63, 2002.

E. C. Monahan. Fresh water whitecaps. *J. Atmos. Sciences*, 26:1026–1029, 1969. doi: 10.1175/1520-0469(1969)026<1026:FWW>2.0.CO;2.

E. C. Monahan and I. O'Muircheartaigh. Optimal power-law description of oceanic whitecap coverage dependence on wind speed. *J. Phys. Ocean.*, 10:2094–2099, 1980. doi: 10.1175/1520-0485(1980)010<2094:OPLDOO>2.0.CO;2.

R. Moore, S. Thurrowgood, D. Bland, D. Soccol, and M.V. Srinivasan. A fast and adaptive method for estimating uav attitude from the visual horizon. In *Intelligent Robots and Systems (IROS), 2011 IEEE/RSJ International Conference on*, 2011a.

R. J. D. Moore, S. Thurrowgood, D. Soccol, D. Bland, and M. V. Srinivasan. A method for the visual estimation and control of 3-dof attitude for uavs. In *Proceedings of Australasian Conference on Robotics and Automation*, 2011b.

D. D. Morris, B. R. Colonna, and F. D. Snyder. Image-based motion stabilization for maritime surveillance. In Edward R. Dougherty Jaakko T. Astola, Karen O. Egiazarian, editor, *Proceedings of SPIE, Image Processing: Algorithms and Systems V*, volume 6497, February 2007.

M. Perlin, W. Choi, and Z. Tian. Breaking waves in deep and intermediate waters. *Annual Review of Fluid Mechanics*, 45(1):115–145, 2013. doi: 10.1146/annurev-fluid-011212-140721.

O. M. Phillips. On the generation of waves by turbulent wind. *J. Fluid Mech.*, 2:417–445, 1957.

O. M. Phillips. Spectral and statistical properties of the equilibrium range in wind-generated gravity waves. *J. Fluid Mech.*, 156:495–531, 1985. doi: 10.1017/S0022112085002221.

O. M. Phillips, F. Posner, and J. Hansen. High range resolution radar measurements of the speed distribution of breaking events in wind-generated ocean waves: Surface impulse and wave energy dissipation rates. *J. Phys. Ocean.*, 31:450–460, 2001.

W. J. Pierson and L. Moskowitz. A proposed spectral form for fully developed wind seas based on the similarity theory of s. a. kitaigorodskii. *Journal of Geophysical Research*, 69 (245):5181–5190, 1964. doi: 10.1029/JZ069i024p05181.

R. C. T. Rainey and M. S. Longuet-Higgins. A close one-term approximation to the highest stokes wave on deep water. *Ocean Engineering*, 33:2012–2024, 2006. doi: 10.1016/j.oceaneng.2005.09.014.

R. J. Rapp and W. K. Melville. Laboratory measurements of deep-water breaking waves. *Phil. Trans R. Soc. Lond. A*, 331:735–800, 1990.

L. Romero and W. K. Melville. Airborne observations of fetch-limited waves in the gulf of tehuantepec. *J. Phys. Ocean.*, 40:441–465, 2010. doi: 10.1175/2009JPO4127.1.

L. Romero, W. K. Melville, and J. M. Kleiss. Spectral energy dissipation due to surface-wave breaking. *J. Phys. Oceanogr.*, 42:1421–1444, 2012. doi: 10.1175/JPO-D-11-072.1.

D. J. Salisbury, M. D. Anguelova, and I. M. Brooks. On the variability of whitecap fraction using satellite-based observations. *J. Geophys. Res.*, 118:6201–6222, 2013. doi: 10.1002/2013JC008797.

B. Scanlon and B. Ward. Oceanic wave breaking coverage separation techniques for active and maturing whitecaps. *Methods in Oceanography*, 8:1–12, 2013. doi: 10.1016/j.mio.2014.03.001.

M. Schwendeman. Wave breaking dissipation in a fetch-limited sea. Master's thesis, University of Washington, 2012.

M. Schwendeman and J. Thomson. A horizon-tracking method for shipboard video stabilization and rectification. *J. Atmos. Ocean. Tech.*, 32:164–176, 2015a. doi: 10.1175/JTECH-D-14-00047.1.

M. Schwendeman and J. Thomson. Observations of whitecap coverage and the relation to wind stress, wave slope, and turbulent dissipation. *J. Geophys. Res. Oceans*, 120, 2015b. doi: 10.1002/2015JC011196.

M. Schwendeman, J. Thomson, and J. R. Gemmrich. Wave breaking dissipation in a young wind sea. *J. Phys. Ocean.*, 44(1):104–127, 2014. doi: 10.1175/JPO-D-12-0237.1.

J. Song and M. L. Banner. On determining the onset and strength of breaking for deep water waves. part i: Unforced irrotational wave groups. *J. Phys. Ocean.*, 32:2541–2558, 2002.

P. Stansell and C. MacFarlane. Experimental investigation of wave breaking criteria based on wave phase speeds. *J. Phys. Oceanogr.*, 32:1269–1283, 2002.

H. F. Stockdon and R. A. Holman. Estimation of wave phase speed and nearshore bathymetry from video imagery. *J. Geophys. Res.*, 105(C9):22,015–22,033, 2000.

G. G. Stokes. On the theory of oscillatory waves. In *Mathematical and Physical Papers*, volume 1. Cambridge Univ. Press, 1880. doi: 10.1017/CBO9780511702242.013.

M. Stramska and T. Petelski. Observations of oceanic whitecaps in the north polar waters of the atlantic. *Journal of Geophysical Research: Oceans*, 108(C3), 2003. doi: 10.1029/2002JC001321.

Y. Sugihara, H. Tsumori, T. Ohga, H. Yoshioka, and S. Serizawa. Variation of whitecap coverage with wave-field conditions. *Journal of Marine Systems*, 66(1–4):47 – 60, 2007. doi: 10.1016/j.jmarsys.2006.01.014.

P. Sutherland and W. K. Melville. Field measurements and scaling of ocean surface wave-breaking statistics. *Geophys. Res. Let.*, 40:3074–3079, 2013. doi: 10.1002/grl.50584.

P. Sutherland and W. K. Melville. Field measurements of surface and near-surface turbulence in the presence of breaking waves. *Journal of Physical Oceanography*, 45(4):943–965, 2015. doi: 10.1175/JPO-D-14-0133.1.

R. Szeliski. *Computer Vision: Algorithms and Applications*. Springer, New York, 2010.

M. A. Tayfun. On narrow-band representation of ocean waves: 1. theory. *J. Geophys. Res. Oceans*, 91(C6):7743–7752, 1986. doi: 10.1029/JC091iC06p07743.

E.A. Terray, M.A. Donelan, Y.C. Agrawal, W.M. Drennan, K.K. Kahma, A.J. Williams, P.A. Hwang, and S.A. Kitaigorodskii. Estimates of kinetic energy dissipation under breaking waves. *J. Phys. Oceanogr.*, 26:792–807, 1996. doi: 10.1175/1520-0485(1996)026<0792:EOKEDU>2.0.CO;2.

J. Thomson. Wave breaking dissipation observed with 'swift' drifters. *J. Atmos. Ocean. Tech.*, 29(12):1866–1882, 2012. doi: 10.1175/JTECH-D-12-00018.1.

J. Thomson and A. Jessup. A fourier-based method for the distribution of breaking crests from video observations. *J. Atmos. Ocean. Tech.*, 26:1663–1671, 2009.

J. Thomson, A. Jessup, and J. Gemmrich. Energy dissipation and the spectral distribution of whitecaps. *Geophys. Res. Let.*, 36(L11601), 2009. doi: 10.1029/2009GL038201.

J. Thomson, E. A. D'Asaro, M. F. Cronin, W. E. Rogers, R. R. Harcourt, and A. Shcherbina. Waves and the equilibrium range at ocean weather station p. *Journal of Geophysical Research: Oceans*, 118(11):5951–5962, 2013. doi: 10.1002/2013JC008837.

J. Thomson, M. S. Schwendeman, S. F. Zippel, S. Moghimi, J. Gemmrich, and W. E. Rogers. Wave breaking turbulence in the ocean surface layer. *J. Phys. Oceanogr.*, 2016. doi: http://dx.doi.org/10.1175/JPO-D-15-0130.1.

S. Thurrowgood, D. Soccol, R. Moore, D. Bland, and M.V. Srinivasan. A vision based system for attitude estimation of uavs. In *Intelligent Robots and Systems, 2009. IROS 2009. IEEE/RSJ International Conference on*, pages 5725–5730, Oct 2009.

S. Thurrowgood, R. J. D. Moore, D. Soccol, M. Knight, and M. V. Srinivasan. A biologically

inspired, vision-based guidance system for automatic landing of a fixed-wing aircraft. *J. Field Robotics*, 31:699–727, 2014.

Z. Tian, M. Perlin, and W. Choi. Energy dissipation in two-dimensional unsteady plunging breakers and an eddy viscosity model. *J. Fluid Mech.*, 655:217–257, 2010. doi: 10.1017/S0022112010000832.

Z. Tian, M. Perlin, and W. Choi. An eddy viscosity model for two-dimensional breaking waves and its validation with laboratory experiments. *Phys. Fluids*, 24(036601), 2012. doi: 10.1063/1.3687508.

J. M. Wanek and C. H. Wu. Automated trinocular stereo imaging system for three-dimensional surface wave measurements. *Ocean Engineering*, 33:723–747, 2006.

M. A. Weisman, S. S. Atakturk, and K. B. Katsaros. Detection of breaking events in a wind-generated wave field. *J. Phys. Oceanogr.*, 14:1608–1619, 1984.

B. Weissling, S. Ackley, P. Wagner, and H. Xie. Eiscam - digital image acquisition and processing for sea ice parameters from ships. *Cold Regions Sci. and Tech.*, 57:49–60, 2009.

P.J. Wiles, T. P. Rippeth, J.H. Simpson, and P.J. Hendricks. A novel technique for measuring the rate of turbulent dissipation in the marine environment. *Geophys. Res. Let.*, 33:L21608, 2006. doi: 10.1029/2006GL027050.

J. M. Williams. Limiting gravity waves in water of finite depth. *Phil. Trans R. Soc. Lond. A*, 302(1466):139–188, 1981. doi: 10.1098/rsta.1981.0159.

D. K. Woolf. Parameterization of gas transfer velocities and sea-state-dependent wave breaking. *Tellus B*, 57(2):87–94, 2005. doi: 10.1111/j.1600-0889.2005.00139.x.

M.J. Yelland, P.K. Taylor, I.E. Consterdine, and M.H. Smith. The use of the inertial dissipation technique for shipboard wind stress determination. *J. Atmos. Ocean. Tech.*, 11: 1093–1108, 1994. doi: 10.1175/1520-0426(1994)011<1093:TUOTID>2.0.CO;2.

I.R. Young. *Wind Generated Ocean Waves*. Elsevier Ocean Engineering Book Series. Elsevier, New York, 1999.

H. C. Yuen and B. M. Lake. Instabilities of waves on deep water. *Ann. Rev. Fluid Mech.*, 12:303–334, 1980. doi: 10.1146/annurev.fl.12.010180.001511.

C. J. Zappa, M. L. Banner, H. Schultz, J. R. Gemmrich, R. P. Morison, D. A. LeBel, and T. Dickey. An overview of sea state conditions and air-sea fluxes during radyo. *J. Geophys. Res.*, 117(C00H19), 2012.

H. Zhang, P. Yin, X. Zhang, and X. Shen. A robust adaptive horizon recognizing algorithm based on projection. *Transactions of the Institute of Measurement and Control*, 33(6): 734–751, 2011.

Z. Zhang. A flexible new technique for camera calibration. *IEEE Transactions on Pattern Analysis and Machine Intelligence*, 22(11):1330–1334, 2000.